A. ÇETİN METU 2008

ASSESSMENT AND MODELLING OF PARTICLE CLUSTERING IN CAST ALUMINUM MATRIX COMPOSITES

ARDA ÇETİN

APRIL 2008

ASSESSMENT AND MODELLING OF PARTICLE CLUSTERING IN CAST ALUMINUM MATRIX COMPOSITES

A THESIS SUBMITTED TO
THE GRADUATE SCHOOL OF NATURAL AND APPLIED SCIENCES
OF
MIDDLE EAST TECHNICAL UNIVERSITY

BY

ARDA ÇETİN

IN PARTIAL FULFILLMENT OF THE REQUIREMENTS
FOR
THE DEGREE OF DOCTOR OF PHILOSOPHY
IN
METALLURGICAL AND MATERIALS ENGINEERING

APRIL 2008

Approval of the thesis:

ASSESSMENT AND MODELLING OF PARTICLE CLUSTERING IN CAST ALUMINUM MATRIX COMPOSITES

submitted by **ARDA ÇETİN** in partial fulfillment of the requirements for the degree of **Doctor of Philosophy in Metallurgical and Materials Engineering, Middle East Technical University** by

Prof.Dr. Canan Özgen
Dean, Graduate School of **Natural and Applied Sciences** _____

Prof.Dr. Tayfur Öztürk
Head of Department, **Metallurgical and Materials Engineering** _____

Prof.Dr. Ali Kalkanlı
Supervisor, **Metallurgical and Materials Engineering Dept., METU** _____

Examining Committee Members:

Prof.Dr. Bilgin Kaftanoğlu
Mechanical Engineering Dept., METU _____

Prof.Dr. Ali Kalkanlı
Metallurgical and Materials Engineering Dept., METU _____

Prof.Dr. Şakir Bor
Metallurgical and Materials Engineering Dept.,METU _____

Prof.Dr. Ekrem Selçuk
Metallurgical and Materials Engineering Dept.,METU _____

Prof.Dr. Tamer Özdemir
Metallurgy Dept., Gazi University _____

Date: 14.04.2008

I hereby declare that all information in this document has been obtained and presented in accordance with academic rules and ethical conduct. I also declare that, as required by these rules and conduct, I have fully cited and referenced all material and results that are not original to this work.

Name, Last Name : ARDA ÇETİN

Signature :

ABSTRACT

ASSESSMENT AND MODELLING OF PARTICLE CLUSTERING IN CAST ALUMINUM MATRIX COMPOSITES

Çetin, Arda
Ph.D., Department of Metallurgical and Materials Engineering
Supervisor: Prof. Dr. Ali Kalkanlı

April 2008, 114 pages

The damage and deformation behaviour of particle reinforced aluminum matrix composites can be highly sensitive to local variations in spatial distribution of reinforcement particles, which markedly depend on melt processing and solidification stages during production. The present study is aimed at understanding the mechanisms responsible for clustering of SiC particles in an Al-Si-Mg (A356) alloy composite during solidification process and establishing a model to predict the risk of cluster formation as a function of local solidification rate in a cast component. Special emphasis has been given to spatial characterization methods in terms of their suitability to characterize composite microstructures. Result indicate that methods that present a summary statistics on the global level of heterogeneity have limited application in quantitative analysis of discontinuously reinforced composites since the mechanical response of such materials are highly sensitive to dimensions, locations and spatial connectivities of clusters. The local density statistics, on the other hand, was observed to provide a satisfactory description of the microstructure, in terms of localization and quantification of clusters. A macrotransport - solidification kinetics model has been employed to simulate solidification microstructures for estimation of cluster formation tendency. Results show

that the distribution of SiC particles is determined by the scale of secondary dendrite arms (SDAS). In order to attain the lowest amount of particle clustering, the arm spacings should be kept within the limit of $2d_{SiC}$ >SDAS >d_{SiC}, where d_{SiC} is the average particle diameter.

Keywords: Discontinuously reinforced composites, clustering, thermal analysis, solidification modelling, quantitative metallography.

ÖZ

DÖKÜM YOLUYLA ÜRETİLMİŞ ALÜMİNYUM TABANLI KOMPOZİTLERDE PARÇACIK TOPAKLANMASININ DEĞERLENDİRİLMESİ VE MODELLEMESİ

Çetin, Arda
Doktora, Metalurji ve Malzeme Mühendisliği Bölümü
Tez Yöneticisi: Prof. Dr. Ali Kalkanlı

Nisan 2008, 114 sayfa

Parçacık takviyeli alüminyum tabanlı kompozitlerin hasar ve deformasyon tepkileri üretimin sıvı faz ve katılaşma aşamalarında şekillenen parçacık dağılımına yüksek duyarlılık göstermektedir. Bu çalışma SiC parçacıklarıyla desteklenmiş Al-Si-Mg (A356) kompozitlerin katılaşma sürecinde parçacık topaklanmasına yok açan mekanizmaları anlamayı ve döküm parçalarda yerel katılaşma hızına bağlı topak oluşma riskini değerlendirebilecek bir model oluşturmayı amaçlamaktadır. Çalışma kapsamında birçok uzamsal analiz yöntemine yer verilmiş ve kompozit mikroyapısı analizine uygunlukları değerlendirilmiştir. Sonuçlar, kompozitlerin mekanik tepkilerinin topakların boyutları, pozisyonları ve uzamsal bağlantılarıyla yakından ilişkili olması nedeniyle genel heterojenlik seviyesini özetleyen istatistiklerin bu malzemelerin karakterizasyonunda sınırlı kullanımı olduğunu göstermektedir. Yerel yoğunluk istatistiğinin sonuçları ise topakların niceliksel değerlendirmesi ve pozisyonlarının tespiti açılarından tatmin edici bulunmuştur. Topak oluşma eğilimini tahmin edebilmek amacıyla katılaşma mikroyapılarının benzetimi için makro transfer - katılaşma kinetiği yaklaşımı kullanılmıştır. Elde edilen benzetimsel mikroyapı değerlendirmelerin deneysel sonuçlarla oldukça uyumlu oldukları görülmüştür. Sonuçlar, SiC parçacık dağılımının ikincil dendrit

kol aralıkları (İDKA) tarafından belirlendiğini göstermektedir. En düşük topaklanma seviyesine ulaşabilmek için ikincil dendrit kol aralıklarının $2d_{SiC}$ >İDKA >d_{SiC}, (d_{SiC} ortalama parçacık boyutunu göstermektedir) aralığında tutulması gerekmektedir.

Anahtar kelimeler: Parçacık takviyeli kompozitler, topaklanma, termal analiz, katılaşma modellemesi, niceliksel metalografi.

ACKNOWLEDGEMENTS

Looking back from the end of this long journey, it is interesting to see how many wonderful people have contributed to this work in a huge variety of ways. This thesis is the account of approximately five years of devoted work, which would not have been possible without the help of many.

First of all, I would like to thank my supervisor, Prof.Dr. Ali Kalkanlı, who gave me this great opportunity to work in such a diverse and comfortable environment. I truly appreciate your belief in me and constant encouragement, without which this work could hardly be completed. I also wish to thank Prof.Dr. Ekrem Selçuk for generously sharing his wisdom and experience, both as a scientist and a human being. I would like to extent my thanks to Haluk Güldür, General Manager of Heraues Electro-Nite, Turkey. Thank you for your belief in our work and your true support that arrives right on time, when necessary. I also would like to acknowledge Prof.Dr. Tamer Özdemir, Prof.Dr. İshak Karakaya, Prof.Dr. Şakir Bor and Prof.Dr. Bilgin Kaftanoğlu for their invaluable suggestions, comments and encouragements.

I am deeply indebted to my friends Güliz and Süha Tirkeş, Seha Tirkeş, Ozan Bilge, Fırat Tiryaki (aka Mr. Bass Cool), Alper Ünver (aka the doktorant assistant), Emilie and Cem Selçuk (long live Ziggy Zinc!), Hansu Birol, Defne Bayraktar, Züleyha Brewer, Deniz Karakuş, Murat Oruç, Özgür Nurdoğan, Özden Sicim, Hamdi Kural, Akın Özyurda & Kağan Menekşe (aka the Master Caster), Fatih Güner, Özgür Duygulu, Özlem Güngör and Koray Yurtışık; for sharing the miserable moments of my Ph.D. life and all the good times we had.

I would like to thank my colleagues and friends at METE, particularly to Ali Erdem Eken, Alper Kınacı, Aydın Ruşen, Barış Akgün, Barış Okatan, Can Ayas, Caner Şimşir, Cem Taşan, Çağla Özgit, Emre Ergül, Elvan Tan, Ergin Büyükakıncı, Evren Tan, Fatih Şen, Güher Kotan, Gülhan Çakmak, Gül İpek Nakaş, Hasan Akyıldız, Metehan Erdoğan, Oğul Can Turgay, Öncü Akyıldız, Pelin Maradit, Selen Gürbüz, Serdar Karakaş, Serdar Tan, Tarık Aydoğmuş, Taylan Örs, Turgut Kırma, Volkan Kalem, Volkan Kayasu and Ziya Esen (please note the alphabetical order) for being around and being themselves. Big thanks for transforming this big and dull building into a warm and lovely working place.

I also would like to express my sincere gratitude to Salih Türe and Özdemir Dinç for their essential and generous support on technical issues. I am also thankful to Cengiz Tan for his commitment to make things with great care and passion to share his knowledge with such a sweet attitude.

My utmost and sincere thanks go to my family, Süreyya, Abdullah and İdil Çetin, without whom this thesis “literally” would not have been possible at all. Thank you very much for your understanding and support.

Finally, I would like to express my very special thanks to Deniz Keçik, who has converted the final period of dissertation preparation, which could have been a depressing and isolated experience, into a tolerable and straightforward process by bringing the utmost peace and joy to my life. It was your understanding, patience and encouragements that have upheld me most of time. Thank you.

TABLE OF CONTENTS

ABSTRACT ……. iv

ÖZ …… vi

ACKNOWLEDGEMENTS ……. viii

TABLE OF CONTENTS ……. x

NOMENCLATURE …… xiii

CHAPTERS

1 INTRODUCTION …….. 1

2 QUANTITATIVE ANALYSIS OF PARTICLE DISTRIBUTION …….. 4

2.1 Brief Review of Literature ……..... 4

2.2 Spatial Analysis Methods ……. 6

2.2.1 Refined nearest neighbour analysis ……. 6

2.2.2 *K*-Function …….. 8

2.2.3 Inference of local clustering …… 9

2.2.4 Visualization of clusters …….. 11

2.2.5 Voronoi tessellation …… 12

3 THERMAL ANALYSIS OF MMC SOLIDIFICATION…… 13

3.1 Newtonian and Fourier Thermal Analysis Methods ……. 13

3.1.1 Calculation of latent heat of solidification ……... 18

3.1.2 Calculation of instantaneous solid fraction ……..... 19

3.2 Thermal Analysis of Composite Solidification ……. 19

3.3 Dendrite Coherency Point ……. 21

4 MODELLING OF MMC SOLIDIFICATION …….. 23

4.1 Theoretical Formulation of Macroscopic Heat Transfer ……... 24

4.2 Microscopic Modelling ……. 26

4.2.1 Pseudo-binary alloy assumption: Calculation of equivalent solute … 26

4.2.2 Nucleation of α-Al dendrites ……... 27

4.2.3 Dendritic growth ……. 28

4.2.4 Eutectic nucleation …….. 30

4.2.5 Eutectic grain growth and impingement ……. 31

4.2.6 Coarsening of secondary dendrite arms …….. 32

5 EXPERIMENTAL & COMPUTATIONAL DETAILS …… 38

5.1 Materials …… 38

5.1.1 Matrix alloy ……. 38

5.1.2 The reinforcement phase ……. 39

5.2 Stir Casting of Aluminum Matrix Composites ……. 41

5.3 Thermal Analysis of MMC Solidification …… 44

5.4 Image Analysis …….. 45

5.5 Computational Details ……... 47

5.5.1 Quantitative analysis of particle distribution …….. 47

5.5.1.1 Computer generated point data …… 47

5.5.1.2 Spatial analysis programs ……. 48

5.5.2 Macrotransport - solidification kinetics modelling ……. 48

6 RESULTS & DISCUSSION …….. 51

6.1 Thermal Analysis of Composite Solidification ……. 52

6.1.1 Evolution of solid fraction …….. 54

6.1.2 Comparison of dendrite coherency point estimations ……. 56

6.2 Quantitative Analysis of Particle Distribution …….. 58

6.2.1 Simulated point data …… 58

6.2.2 Quantitative analysis of composite microstructures ……... 66

6.2.2.1 Refined nearest neighbour analysis …….. 66

6.2.2.2 Voronoi tessellation ……. 69

6.2.2.3 *K*-function …… 71

6.2.2.4 Local density statistics ……. 73
6.2.2.5 Effect of metallographic field size on cluster dimensions ……... 79
6.2.2.6 Comparison of methods ……... 82
6.3 Effect of Solidification Rate on Clustering of SiC Particles …….. 83
6.3.1 Effect of solidification rate on dendritic structure …….. 83
6.3.2 Effect of solidification rate on particle distribution …… 84
6.4 Modelling of MMC Solidification …… 90
6.4.1 Prediction of local solidification rate …….. 90
6.4.2 Prediction of secondary dendrite arm spacings …….. 96

7 CONCLUSIONS …… 99

REFERENCES …… 102

APPENDICES

A. Phase diagram and solidification path of A356 alloy …… 107
B. Mold dimensions and thermocouple locations ……... 111

VITA ……..... 113

NOMENCLATURE

A	area	m^2
C	concentration	wt%
C_L*	liquid interface concentration	wt%
$\langle C_L \rangle$	average liquid concentration	wt%
CSR	complete spatial randomness	
CV	coefficient of variation	
D	diffusion coefficient	m^2 sec^{-1}
DCP	dendrite coherency point	
E	expected value	
FTA	Fourier thermal analysis	
G	free energy	J
J	flux	atoms m^{-2} sec^{-1}
M	mass content	
N	number of events / particles	
N_s	volumetric nucleation site density	m^{-3}
NS	Neyman-Scott cluster process	
NTA	Newtonian thermal analysis	
P	thermocouple location	m
Q	heat loss	J
R	grain radius	m
S	source term	
SR	solidification rate	°C sec^{-1}
T	temperature	°C
T_m	melting point of pure Al	°C
T_{bulk}	average temperature in the volume element	°C
TC	thermocouple	

V	volume	m^3
V_s	solidification velocity	$m\ sec^{-1}$
X	alloying element	
Z_F	Fourier zero curve	$°C\ sec^{-1}$
a	primary nucleation parameter	m^{-3}
b	primary nucleation parameter	$s^2\ m^{-3}\ °C^2$
c_p	specific heat	$J\ kg^{-1}\ °C^{-1}$
c_v	volumetric heat capacity	$J\ m^{-3}\ °C^{-1}$
d	distance	m
d_{SiC}	SiC particle diameter	m
f	volume fraction	
h	kernel bandwidth	
h_i	heat transfer coefficient	$W\ m^{-2}\ °C^{-1}$
k	thermal conductivity	$W\ m^{-1}\ °C^{-1}$
m	liquidus slope	$°C\ wt\%^{-1}$
n	number	
r	radius	m
t	time	sec
u	Euclidean distance	m
t_f	local solidification time	sec
w	nearest neighbour distance	μm
ΔH_f	latent heat of solidification	$J\ kg^{-1}$
ΔT	undercooling	°C
Φ	average dendrite arm diameter	μm
α	thermal diffusivity	$m^2\ sec^{-1}$
ϕ	phase quantity	
γ	intensity	$events\ area^{-1}$
κ	partition coefficient	
λ_2	secondary dendrite arm spacing	μm
μ	mean	
μ_0	coarsening constant	$m^3\ sec^{-1}$
μ_{eut}	eutectic growth constant	$m\ sec^{-1}\ °C^2$
μ_N	nucleation parameter	$m^{-2}\ °C^{-2}$

ρ	density	kg m^{-3}
σ	standard deviation	
ξ	significance parameter	
ψ	impingement correction factor	
Γ	Gibbs-Thomson coefficient	m °C

SUPERSCRIPTS & SUBSCRIPTS USED

A	area
L	liquid
P	particle
S	solid
comp	composite
eq	equivalent
eut	eutectic
g	growing
m	mold
	matrix
obs	observed
pois	Poisson
s	shrinking
∞	surroundings

CHAPTER 1

INTRODUCTION

Metal matrix composites (MMC) have proven to offer distinctive advantages over a number of conventional materials being used in aerospace, ground transportation (auto and rail), defense, thermal management and infrastructure industries. These advantages include improved strength, stiffness, fatigue and wear resistances with good thermal properties, while maintaining low weight. Another advantage is that the extent of such improvements can be tailored by altering the type, size and morphology of the reinforcement phase. There are two basic groups of reinforcements, which are referred as *continuous* and *discontinuous*. Continuous reinforcements are typically fibers or monofilament wires, offering attractive improvements in longitudinal properties by sacrificing transverse properties. Isotropic improvements can be obtained by employing discontinuous reinforcements, such as whiskers, particles and short fibers. Among these alternatives, the most attractive options for commercial practice are silicon carbide and alumina in the form of "particles" with aluminum alloy matrices due to their distinct advantage in terms of affordability. Hence, in today's industry, discontinuously reinforced aluminum composites (DRA) account for majority of MMC annual production.

Due to extensive research on production and characterization of such materials, today DRA are an established technology. However, there are still certain problems, one and most important, being the clustering or *agglomeration* of reinforcement particles. The extent of property degradation associated with particle clustering have numerously been underlined by many researchers throughout the period covering from early 80's, where DRA technology was first emerged, onwards to very recent investigations. Although certain solutions were derived by altering the processing method (such as infiltrating the liquid metal to a packed preform of reinforcements) or controlling processing variables

(such as the particle size ratio in powder metallurgy routes), no neat solutions could be proposed for casting processes, where bulk of MMC production are carried out. There are only certain *beliefs* about solidification routes that finer dendritic arm spacings would produce uniform distribution of reinforcements (which is proved to be wrong in this study), however no quantitative data were reported in the literature.

In order to understand the origin of clustering problem and to be able to quantify the amount of reinforcement clustering, one should have a very clear idea of what a *cluster* is. The literature on this aspect of MMC technology sadly lacks a thorough understanding of spatial characterization methods. There are only a few studies that came into prominence in this aspect, which are briefly reviewed in the following pages. In general, there is an ambiguity concerning the type of information that an engineer needs regarding the microstructure of a MMC. The problem is that, the terms *inhomogeneity* and *clustering* are commonly used as synonyms and the microstructures of MMCs are considered in terms of global trends in the distribution. However, as far as the fracture mechanics of MMCs is concerned, one also needs to gather information on the amount, locations and spatial connectivities of reinforcement clusters, since failure mechanisms of such materials include crack nucleation and propagation with a high sensitivity to cluster locations. Therefore attempting to characterize MMC microstructures by simple scalar descriptions, although holds a practical value, lacks a great deal of information to successfully associate the mechanical response of the composite to its microstructure.

The present study is structured in three parts. The first part attempts to answer the questions; what is a cluster and how can it be detected? The effort to answer these questions actually forms the backbone of the study, since the clusters can neither experimentally be detected nor computationally predicted without a clear understanding of what we are looking for. The second part is an experimental study on relation of clustering with local microstructure, which will help to understand cluster formation tendencies as a function of location within castings with complex geometries. The third and final part is a computational study aimed at simulating solidification microstructures as a function of local solidification time and therefore to predict the tendency of reinforcement clustering. Putting these parts together results in a thorough picture in which certain locations in a casting, where there exists a tendency towards clustered particle arrangements can be predicted before production. Such an ability will obviously help engineers to come up

with solutions to produce these components with more uniform microstructures and hence, less prone to failure. These solutions may include interventions to production process such as refinement of microstructure or varying reinforcement size, or altering component designs to improve microstructural uniformity.

Due to combinatorial nature of the present work, the theoretical background is presented in three different chapters. Firstly, the spatial characterization methods are given in Chapter 2. Chapter 3 focuses on thermal analysis of metal matrix composites, which provides a clear description of MMC solidification. Chapter 4 introduces the numerical approach to MMC solidification. Chapter 5 presents the experimental and computational details, followed by the results and discussion in Chapter 6. Finally, concluding remarks are summarized in Chapter 7.

CHAPTER 2

QUANTIATIVE ANALYSIS OF PARTICLE DISTRIBUTION

2.1 Brief Review of Literature

It is well known that introduction of hard ceramic particles into soft metallic matrices leads to profound improvements in mechanical properties such as increased strength, stiffness and fatigue resistance while maintaining low weight[1,2]. The origin of these property enhancements is primarily attributed to two mechanisms. In the first one, the strengthening is ascribed to direct load transfer from the matrix to the reinforcement phase[3-6]. The second mechanism, on the other hand, attributes strengthening of the material to increasing dislocation density of matrix due to developed residual plastic strain, which results from thermal mismatch between the ceramic particles and the matrix material[5-9].

In structural composites, one of the most critical design criterions is fatigue resistance, which is particularly important in automotive and aerospace industries where resistance to high cycle fatigue resistance is strictly necessary[6]. The failure process of discontinuously reinforced composites is generally described over two stages; damage localization and damage globalization[10]. The first stage includes various mechanisms such as particle and matrix interface debonding, particle fracture, void formation in the ductile matrix, short crack initiation and crack coalescence. The second stage, on the other hand, consists of a long crack growth stage, which follows Paris' Law in the intermediate stress intensity factor range[10]. There are various factors that influence localization and globalization of the damage. One such parameter is the size of reinforcement particles. In

general, as the particle size increases, it is more likely that it contains a surface crack[11, 12]. This assumption was verified through various experimental studies that directly relate the particle cracking frequency with increasing particle size[2, 13]. Orientation and morphology of the reinforcing particles were also reported to contribute to damage behaviour of the composites[14, 15]. One other important factor that determines the mechanical response of the composite is the spatial distribution of second phase particles. Although the aforementioned factors other than spatial arrangement of particles can well be altered by varying the size or morphology of reinforcements, control of particle distribution requires a thorough understanding of the factors that determine their arrangement.

Composite microstructures often display clustered arrangements. Although such clusters were reported to have negligible effect on elastic properties,[16, 17] they have profound influence on damage evolution and failure mechanisms. One such influence is the stress localization in these regions[15], which increases the probability of particle failure to a significant extent[17, 18]. Presence of particle clusters was also reported to decrease the yield strength, strain hardening rate and failure strain of the composite over the monolithic material[16]. The origin of this property degradation is attributed to preferential nucleation of cracks[12, 14] in clustered regions and final fracture is produced by crack propagation through the matrix to other clusters[11, 19, 20]. Finally, Ayyar and Chawla's[14, 21] work have shown through finite element simulations that the crack growth resistance of the material is also lower in composites with clustered distributions compared to random arrangements.

The very first attempts in quantitative metallography of metal matrix composites were carried out by Wray *et al*[22] and Spitzig *et al*[23] by characterizing the composite microstructures by Dirichlet tessellation and nearest neighbour methods. Among the various studies that came into prominence in this field; Everett *et al*[24] have compared the Monte-Carlo based computer generated patterns with actual composite microstructures by utilizing Dirichlet tessellation, nearest neighbour statistics and radial distribution function. Various characterization functions of Voronoi cell based geometric parameters for characterization and response modeling of composites was introduced by Ghosh *et al*[25]. Li *et al*[26] computationally constructed 3D microstructure models by sequentially assembling digital section micrographs obtained by serial sectioning and presented a systematic approach to 2D and 3D microstructural characterization. A computational approach based

on Voronoi tessellation to determine the local reinforcement area fraction contour maps was adopted by Ganguly and Poole[27]. Finally, Scalon *et al*[28] investigated the distribution of second phase particles by various pattern descriptor functions and modeled their spatial distribution by a Strauss point process model.

Those studies have either concentrated on application of various quantitative characterization methods or attempted to correlate the spatial configuration of second phase particles to the mechanical response of composite systems. They have mainly described the observed spatial patterns by considering the global trends in the distribution of particles and used suitable descriptors to discriminate between random and clustered arrangements. However, such approaches may fail to predict the actual failure susceptibility of these materials since damage and deformation behaviour of composites can be highly sensitive to local variations in particle content and spatial correlations between these local variations. For example, previous research[18, 19] on fracture behaviour of discontinuously reinforced composites showed that in composites with clustered particle arrangements, damage preferentially initiates from clusters and final fracture is produced by crack propagation through the matrix to other clusters. Therefore, the spatial heterogeneity in these systems should be characterized by considering the locations, dimensions and spatial connectivity of the clusters rather than simple scalar descriptions of microstructures.

2.2 Spatial Analysis Methods

2.2.1 Refined Nearest Neighbour Analysis

The refined nearest-neighbour analysis[29] is based on comparison of the complete distribution functions of either w, the nearest-neighbour distance between events (G-function), or x, the distance from a sampling point (not event) to the nearest event (F-function) with that of expected distribution of events for complete spatial randomness (CSR). The theoretical cumulative distribution function of nearest-neighbour distances under the null hypothesis of CSR is given by

$$G(w) = 1 - \exp(-\gamma \pi w^2) \tag{2.1}$$

where γ is the intensity. An appropriate edge corrected estimate of the observed distribution function would be

$$\hat{G}(w) = \frac{\sum_i I(w_i \le w, r_i > w)}{\sum_i I(r_i > w)} \tag{2.2}$$

where I is the indicator function that denotes the count of events, and r_i and w_i are the distances from the ith event to its nearest boundary and to its nearest neighbour, respectively. The deviation of an observed pattern from randomness can be detected from the difference of estimates of observed and theoretical distribution functions[29]. The deviation of an observed pattern from CSR can also be brought out by utilizing the ratio of means, given by

$$Q = \frac{E_{obs}(\overline{w})}{E_{pois}(\overline{w})} \tag{2.3}$$

where $E_{obs}(\overline{w})$ is the observed mean of nearest neighbour distances and $E_{pois}(\overline{w})$ is the expected mean of nearest neighbour distances for a Poisson process. The expected mean of a Poisson distribution is given by the expression[30]

$$E_{pois}(\overline{w}) = 0.5\left(\frac{N}{A}\right)^{-0.5} \tag{2.4}$$

where N/A gives the area density of the events within the study region. Different types of spatial distributions can therefore be classified according to:

- ✓ $Q \approx 1$ denotes random event sets,
- ✓ $Q < 1$ implies clustered distribution,
- ✓ $Q > 1$ implies uniform distribution.

2.2.2 *K*-Function

One drawback of the refined nearest-neighbour distance methods is that they only consider the distances to the closest events, ignoring the larger scales of pattern. The *K*-function, on the other hand, provides a summary of spatial dependence over a wide range of scales including all event to event distances, not only the nearest-neighbour distances. The most commonly used edge-corrected estimator of the *K*-function is given by Ripley[31] as

$$\hat{K}(t) = \frac{1}{\gamma} \sum_{i} \sum_{j \neq i} \frac{I_t(u_{ij})}{w_{ij}} \tag{2.5}$$

where γ is the intensity, u_{ij} is the distance between the ith and jth events and I_t is the indicator function that denotes the count belonging to a value of t for the distance comparisons $u_{ij} \leq t$. The weight function w_{ij} provides the edge correction by considering the proportion of the circumference of the circle around event i. The *K*-function for a homogeneous Poisson distribution of events is given by $K(t) = \pi t^2$. *K*-function is commonly transformed to

$$\hat{L}(t) = \sqrt{\frac{\hat{K}(t)}{\pi}} - t \tag{2.6}$$

as Eqn. (2.6) yields a theoretical value of zero under the null hypothesis of CSR. Positive values above the confidence interval suggest the presence of clusters whereas negative values below the confidence interval suggest a uniform distribution of events.

2.2.3 Inference of Local Clustering

Although the *K*-function successfully measures the local density around each event over many distance scales, the presence of clustering can be inferred only when the local density around an event exceeds a certain threshold value. In order to determine this threshold value and to estimate the local amount of clustering around an event, we have adopted a cumulative radial distribution function, $\rho(P_i, r)$, which in the present study is defined as the number of reinforcement particles per unit area within the radius r from an original particle P_i, divided by the number of particles per unit area of the whole study region. Fig. 2.1 illustrates the evaluation of $\rho(P_i, r)$.

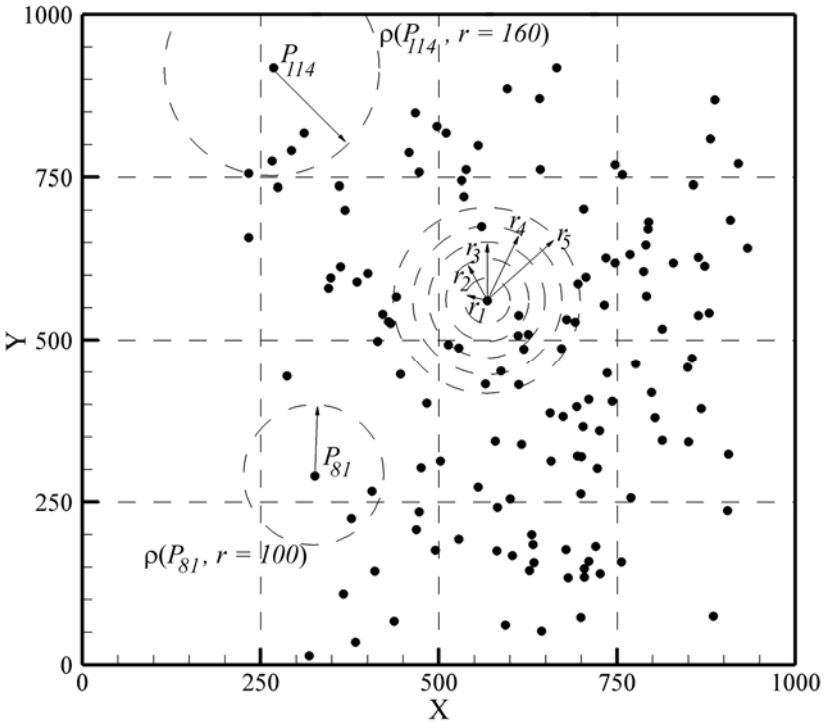

Figure 2.1 Evaluation procedure of $\rho(P_i, r)$ illustrated at five distance scales; r_1, r_2, r_3, r_4 and r_5. $\rho(P_i, r)$ is also illustrated for particles P_{81} and P_{114} at distance scales of 100 and 160 units, respectively.

A similar concept of density calculation was previously introduced by Prodanov *et al*[32] by defining a parameterized threshold function $T_{\xi}(r)$, which expresses the probability that the local density around a particle, as depicted by $\rho(P_i, r)$, exceeds a certain threshold value in an associated Poisson (random) point process. In the present study the threshold function $T_{\xi}(r)$ for each study region was estimated from 200 simulations of homogeneous Poisson process with the same intensity as the studied pattern. The significance parameter ξ was set to 0.95; meaning that only 5% of the points in an associated Poisson point process were expected to exceed the threshold $T_{0.95}(r)$. Therefore, a particle in the study region can be inferred as a part of a cluster if the local density around that particular particle exceeds the amount present in an associated Poisson process; $\rho(P_i, r) > T_{0.95}(r)$, at a particular radius, r. In order to consider the edge effects, a weighted edge correction scheme, which is based on weighing the proportion of the circumference of the disc that remains inside the study region to entire circumference, was applied[31].

An important aspect of this approach is that the local density around a particle may or may not exceed the corresponding threshold value depending on the scale of observation, r. Following the method of Prodanov *et al*[32] the above-threshold particles, which were accepted to be a part of a cluster were updated at each scale of observation and the information regarding the coordinates of these particles were collected in a set of above-threshold particles, $S(r)$. The percent ratio of above-threshold events averaged over all scales of observation is then calculated from

$$\%Threshold = \frac{\frac{1}{T}\int_0^T N(t)dt}{N_{events}} \tag{2.7}$$

where N_{events} is the total number of events in the study region and T denotes the overall scale of observation.

2.2.4 Visualization of Clusters

In order to reveal the spatial correlations between the detected clusters, one needs to visualize the locations, dimensions and relative intensities of the clusters. One common way to obtain a spatially smooth intensity estimate of points within a study region is the kernel estimation[33]. The intensity, $\gamma(\boldsymbol{x})$, at location $\boldsymbol{x}$ can be estimated by

$$\hat{\gamma}_h(\boldsymbol{x}) = \sum_{i=1}^{n} \frac{1}{h^2} k\left\{\frac{(\boldsymbol{x} - \boldsymbol{x}_i)}{h}\right\} \tag{2.8}$$

where h is the bandwidth parameter that regulates the degree of smoothness, $\boldsymbol{x}$ is the location for intensity estimation, $\boldsymbol{x_i}$ is the observed event location, n is the number of points and $k\{\}$ represents the kernel weighting function. Scalon *et al*[28] successfully utilized this method for intensity estimation of the second phase particles in an Al/SiC_p composite. A more refined approach to visualize the clusters would be to associate the set of above-threshold particles to the sum of kernels by only considering the above-threshold particles that belong to $S(r)$, at a particular scale of observation, r. With this approach, one can locate the clusters and compare their relative intensities instead of complicated contour plots that represent the intensity variation of the whole data set. Since different suitable alternatives of the kernel weighting functions have relatively small effect on the resulting intensity estimate,[34] we have implemented a simple quartic density function denoted by

$$k(\boldsymbol{u}) = \begin{cases} \frac{3}{\pi}(1 - \boldsymbol{u}^T\boldsymbol{u})^2 & \text{for } |\boldsymbol{u}| < 1 \\ 0 & \text{otherwise} \end{cases} \tag{2.9}$$

where $|\boldsymbol{u}|$ represents the Euclidean distance of the vector $\boldsymbol{x}$ (e.g. $\sqrt{\boldsymbol{u}^T\boldsymbol{u}} = \boldsymbol{x}$). The relative intensities of the above-threshold particles can therefore be estimated by

$$\hat{\gamma}_h(\boldsymbol{x}) = \sum_{i \in S(r)} \frac{3}{\pi h^2}\left[1 - \frac{d_i^2}{h^2}\right]^2 \tag{2.10}$$

where, d_i is the distance between the location of intensity estimation and the observed particle location, and the summation is only over values of d_i which do not exceed h.

2.2.5 Voronoi Tessellation

The Voronoi diagram[35] built on a set of events represents partition of the area into a set of adjacent regions that have the shape of convex polygons such that each polygon contains exactly one event. The relevant properties of a Voronoi polygon, such as its area, may be used to distinguish between different point processes. The dispersion of the probability density function, known as the coefficient of variation, can be defined for polygon area as

$$CV_A = \frac{\sigma_A}{\mu_A} \tag{2.11}$$

where σ is the standard deviation and μ is the mean of the probability density function, and the subscript A refer to polygon area. A lower CV_A value indicates uniform distribution whereas higher values imply clustering of events.

CHAPTER 3

THERMAL ANALYSIS OF MMC SOLIDIFICATION

3.1 Newtonian and Fourier Thermal Analysis Methods

Newtonian[36] and Fourier[37] thermal analysis methods are simplified but convenient techniques to monitor the average temperature variations and phase changes during the course of solidification. They are actually applicable at the limiting cases when solidification is fully controlled by the thermal resistance at the metal / mold interface or by low thermal diffusivity of the metal.

Both methods are based on interpretation of cooling curves obtained from one or more locations in the casting. The difference of these method is the way their baseline, or *zero curve*, is generated. The zero curve represents the hypothetical variation of the metal's cooling rate, if there would be no phase transformation within the covered temperature range. Newtonian analysis neglects the presence of thermal gradients and generates the zero curve from the thermal data obtained from a single thermocouple. In Fourier analysis, on the other hand, the zero curve is a function of temperature Laplacian and therefore requires minimum of two (in cylindrical geometry) or three (in Cartesian geometry) thermocouples.

As mentioned above, in Newtonian analysis only one thermocouple, placed at the geometrical center of the casting is used and the presence of thermal gradients is neglected. This assumption is valid only when the Biot number for a particular geometry and metal-mold system is less than 0.1. Biot number[38] is a dimensionless number that relates the resistance to heat transfer inside and at the surface of a sample (i.e. the metal-mold interface in the present case). Values smaller that 0.1 imply that the heat conduction

inside the solidifying sample is much faster than at the metal-mold interface, so that the temperature gradients within the sample may be neglected. In all samples analyzed in the present study, the Biot numbers were verified to be smaller than 0.1 for validity of the Newtonian thermal analysis procedure.

In Newtonian analysis, the zero curve is derived from a simple energy balance for a hypothetical case where the metal does not go under any phase transformation. The rate of heat loss to the surroundings is given by the expression

$$\frac{dQ}{dt} = -h_i A\left(T - T_\infty\right) \tag{3.1}$$

where dQ / dT is the rate of heat loss to the surroundings, t is time, h_i is the coefficient of heat loss to the surroundings, A is the effective surface area over which heat transfer occurs, T is instantaneous temperature and T_∞ is the temperature of the surroundings. The rate of heat evolved to the surroundings can be described by the equation

$$\frac{dQ}{dt} = V \rho c_p \frac{dT}{dt} \tag{3.2}$$

where V is the volume of solidifying metal, ρ is density and c_p is the specific heat capacity. If the metal does not go under any phase transformation within the covered temperature range, these two equations can be equated to yield

$$\frac{dT}{dt} = -\left(\frac{h_i A}{V \rho c_p}\right)\left(T - T_\infty\right) \tag{3.3}$$

Eqn. (3.3) represents the derivative of the cooling rate of a sample, which does not go under any phase transformation; i.e. the zero curve. However, there are certain difficulties associated with this equation. First one is the calculation of the heat transfer parameter, since it is affected from many parameters such as; variations in pouring temperature, sample geometry and reactions between the sample and the sand mold. The value of specific heat is the second potential difficulty, since it is a strong function of

composition and temperature, and therefore depends on the relative amounts of phases present at any temperature. These difficulties can be overcome by using the thermal data obtained from cooling curve to generate the zero curve. Rearranging and integrating Eqn. (3.3) yields

$$\int_{T_i}^{T} \frac{dT}{T - T_\infty} = -\int_{0}^{t} \frac{h_i A}{V \rho c_p} dt \tag{3.4}$$

$$ln\left(\frac{T - T_\infty}{T_i - T_\infty}\right) = -\left(\frac{h_i A}{V \rho c_p}\right) t \tag{3.5}$$

Rearranging to give the instantaneous temperature;

$$T = \left(T_i - T_\infty\right) exp\left(-\frac{h_i A}{V \rho c_p}\right) t + T_\infty \tag{3.6}$$

where T_i is the initial temperature at t = 0. Derivative of Eqn. (3.6) finally yields the expression for zero curve

$$\left(\frac{dT}{dt}\right)_{zc} = -\left(T_i - T_\infty\right)\left(\frac{h_i A}{V \rho c_p}\right) exp\left(-\frac{h_i A}{V \rho c_p} t\right) \tag{3.7}$$

Eqn. (3.7) can be rewritten as

$$\left(\frac{dT}{dt}\right)_{zc} = -C_1 C_2 exp\left(-C_2 t\right) \tag{3.8}$$

where the subscript *zc* denotes the zero curve and $C_1 = T_i - T_\infty$ and $C_2 = h_i A / V \rho c_p$ are constants to be determined experimentally.

Therefore, one can obtain the Newtonian zero curve experimentally by curve fitting of an exponential function from one no-phase transformation region (i.e. above liquidus) to the other (i.e. after solidification is completed). The obvious source of error in this approach is the chosen time steps for curve fitting, which can create significant differences in the resulting zero curve. There are various suggestions for curve fitting of the arbitrary function in the literature[39, 40] however; no common agreement or a procedure could be established to obtain this curve.

The derivation of the Fourier zero curve is much more straight forward. It starts with the Fourier equation, including a heat source;

$$\frac{\partial T}{\partial t} = \alpha \nabla^2 T + \frac{1}{c_v}\frac{\partial Q}{\partial t} \tag{3.9}$$

where α is the thermal diffusivity, ∇T is the temperature Laplacian and c_v is the volumetric specific heat and Q is the heat evolved during solidification. Rearranging

$$\frac{\partial Q}{\partial t} = c_v\left(\frac{\partial T}{\partial t} - Z_F\right) \tag{3.10}$$

where $Z_F = \alpha\nabla^2 T$ is the Fourier zero curve. In order to obtain the Fourier zero curve, therefore, one should be able to describe the temperature Laplacian within the solidifying casting. In a Cartesian geometry, a minimum of three thermocouples are necessary to describe the temperature field. However, the required number of thermocouples can be reduced to two in a symmetric temperature field[37]. The temperature Laplacian in a cylindrical casting, which is symmetrical with respect to the vertical axis, is given by

$$\nabla^2 T = \frac{\partial^2 T}{\partial r^2} + \frac{1}{r}\frac{\partial T}{\partial r} \tag{3.11}$$

When two thermocouples are placed in a cylindrical casting at two different locations, P_1 and P_2, from the center, the differentials in Eqn. (3.11) can be expressed as

$$\nabla^2 T = \frac{\frac{T_2 - T_1}{P_2 - P_1} - 0}{P_1 + \frac{P_2 - P_1}{2}} + \frac{1}{P_1 + \frac{P_2 - P_1}{2}} \left(\frac{T_2 - T_1}{P_2 - P_1} \right) \tag{3.12}$$

where T_1 and T_2 are temperature values read from thermocouple locations P_1 and P_2, respectively. Upon rearranging, Eqn. (3.12) reduces to

$$\nabla^2 T = \frac{4\left(T_2 - T_1\right)}{P_2 - P_1} \tag{3.13}$$

When there is no phase transformation (Q_s = 0) the thermal diffusivity of the system can be obtained from Eqn. (3.10) as

$$\alpha = \frac{\partial T}{\partial t} \frac{1}{\nabla^2 T} \tag{3.14}$$

Therefore, when the cooling rates and Laplacians are known before and after solidification, thermal diffusivities of the solid, α_s, and liquid, α_l, can be calculated. The instantaneous values of the thermophysical properties during solidification can be calculated by an iterative method. The iteration starts with a linear assumption of the variation in solid fraction

$$f_S = \frac{t - t_{end}}{t_{end} - t_{start}} \tag{3.15}$$

where, t is the instantaneous time and the subscripts *start* and *end* denote the start and end of solidification, respectively. At each time step, the instantaneous values of α and c_v of the solid liquid mixture are calculated as

$$\alpha = \alpha_L \left[1 - f_S\right] + \alpha_S f_S \tag{3.16}$$

$$c_v = c_{v,L} \left[1 - f_S\right] + c_{v,S} f_S \tag{3.17}$$

where, $c_{v,L}$ and $c_{v,S}$ are the volumetric heat capacities of the liquid and solid, respectively.

3.1.1 Calculation of Latent Heat of Solidification

As mentioned above, the zero curve represents the variation in the cooling rate of a hypothetical sample if it would go under no phase transformation. Consequently, it should be clear that, the difference between the cooling rate of a sample (i.e. the derivative of cooling curve) and its zero curve results from the released latent heat associated with the solidification of the sample. Therefore, one can calculate the amount of released latent heat by quantifying this difference.

Latent heat calculation in Newtonian analysis starts with including the heat generation term. When phase transformation occurs, Eqn. (3.3) can be expressed as

$$\frac{dQ}{dt} = V \rho c_p \frac{dT}{dt} + \frac{dQ_L}{dt} \tag{3.18}$$

where Q_L is the heat resulting from latent heat release during phase transformation. Combining Eqn.s (3.1) and (3.18) and rearranging

$$\left(\frac{dT}{dt}\right)_{cc} = \frac{1}{V \rho c_p}\left(h_i A\left(T - T_\infty\right) - \frac{dQ_L}{dt}\right) \tag{3.19}$$

The magnitude of latent heat released during solidification can be calculated by subtracting Eqn. (3.7) from Eqn. (3.19) and integrating within the interval of solidification

$$L = -c_p \left[\int_{t_s}^{t_e} \left(\frac{dT}{dt}\right)_{cc} dt - \int_{t_s}^{t_e} \left(\frac{dT}{dt}\right)_{zc} dt\right] \tag{3.20}$$

In Fourier analysis, latent heat is calculated by integrating Eqn. (3.10). This integrated form is actually very similar to Eqn. (3.20) since the zero curve term is already included in Eqn. (3.10). The governing equation is

$$L = \int_{t_s}^{t_e} \left(\frac{\partial Q}{\partial t} \right) dt \tag{3.21}$$

where t_s and t_e denote the start and end of solidification, respectively.

3.1.2 Calculation of Instantaneous Solid Fraction

The solid fraction evolution is calculated with the assumption that the latent heats associated with primary and eutectic solidifications are equal. The instantaneous fraction of the solid phase at time t can therefore be calculated as

$$f_s(t) = \frac{1}{L} \int_{t_s}^{t} \left(\frac{\partial Q}{\partial t} \right) dt \tag{3.22}$$

3.2 Thermal Analysis of Composite Solidification

Newtonian and Fourier methods need some corrections to be applied to composite solidification. Firstly, the reinforcement particles do not go under any phase transformation during solidification of the matrix alloy. Therefore the mass content of particles should be considered since the latent heat values are calculated per unit mass. The latent heat associated with the solidification of the composite therefore can be expressed as

$$L_{comp} = L\left(1 - M_p\right) \tag{3.23}$$

where M_p is the mass content of particles and the subscript *comp* denotes composite. The second point to be corrected is the effect of particles on the thermophysical properties of the composite materials. The governing equations are presented in Table 3.1.

Table 3.1. Equations for thermophysical properties

Temp Interval	Derived Equations	
$T > T_L$	$c_p^{comp} = \dfrac{V_{SiC} \cdot \rho_{SiC} \cdot c_p^{SiC} + (1 - V_{SiC}) \cdot c_p^{L} \cdot \rho_L}{\rho_{comp}}$	(3.24)
	$\rho_{comp} = V_{SiC} \cdot \rho_{SiC} + (1 - V_{SiC}) \cdot \rho_L$	(3.25)
$T_L > T > T_{end}$	$c_p^{comp} = \dfrac{V_{SiC} \cdot \rho_{SiC} \cdot c_p^{SiC} + (1 - V_{SiC}) \cdot c_p^{m} \cdot \rho_m}{\rho_{comp}}$	(3.26)
	$\rho_{comp} = V_{SiC} \cdot \rho_{SiC} + (1 - V_{SiC}) \cdot \rho_m$	(3.27)
	$c_p^{m} = c_p^{L} \cdot (1 - f_S) + c_p^{S} f_S$	(3.28)
	$\rho_m = \rho_L \cdot (1 - f_S) + \rho_S \cdot f_S$	(3.29)
$T_{end} > T$	$c_p^{comp} = \dfrac{V_{SiC} \cdot \rho_{SiC} \cdot c_p^{SiC} + (1 - V_{SiC}) \cdot c_p^{S} \cdot \rho_S}{\rho_{comp}}$	(3.30)
	$\rho_{comp} = V_{SiC} \cdot \rho_{SiC} + (1 - V_{SiC}) \cdot \rho_S$	(3.31)

where V_{SiC} is the volume content of SiC particles, and the sub- and superscripts *l*, *s*, *m* and *SiC* denote liquid, solid, matrix and SiC particles, respectively.

3.3 Dendrite Coherency Point

Dendrite coherency point (DCP) is defined as the solid fraction at which the freely growing equiaxed dendrites impinge upon each other and a rigid, solid network of dendrites is established throughout the casting. It also defines a transition from mass feeding to interdendritic feeding[41]. Casting defects such as interdendritic porosity, macrosegregation and hot tears start to develop after DCP[42].

SiC particles are not suitable substrates for nucleation of α-Al. The dendrites therefore nucleate on available substrates other than SiC particles and push the reinforcement particles into the interdendritic regions, resulting in a segregated pattern of particles. Within the framework of the present study, we have also analyzed whether DCP can be regarded as an index to the distribution of second phase particles, since the distance scales that the particles are being pushed by the growing dendrites are related to the point where impingement occurs.

DCP can be determined by either mechanical methods[43, 44] or thermal analysis[45, 46]. The mechanical methods are based on rheological measurements during solidification. The abrupt increase in viscosity of the melt at some stage during solidification is attributed to impingement of primary dendrites. Thermal analysis method, on the other hand, monitors the variation in thermal gradient during the course of solidification. One thermocouple is placed at the geometrical center of the casting and another next to the mold wall and the temperature difference, ΔT, read from these thermocouples are recorded. When the freely growing dendrites touch each other and a solid network is established all throughout the casting, the rate of heat transfer increases due to higher thermal conductivity of the solid phase. This results in a decrease in the magnitude of the thermal gradient in the casting, which can be monitored from the ΔT curve in Fig. 3.1. The first minimum in this curve is the dendrite coherency since the magnitude of thermal gradient starts to decrease after this point.

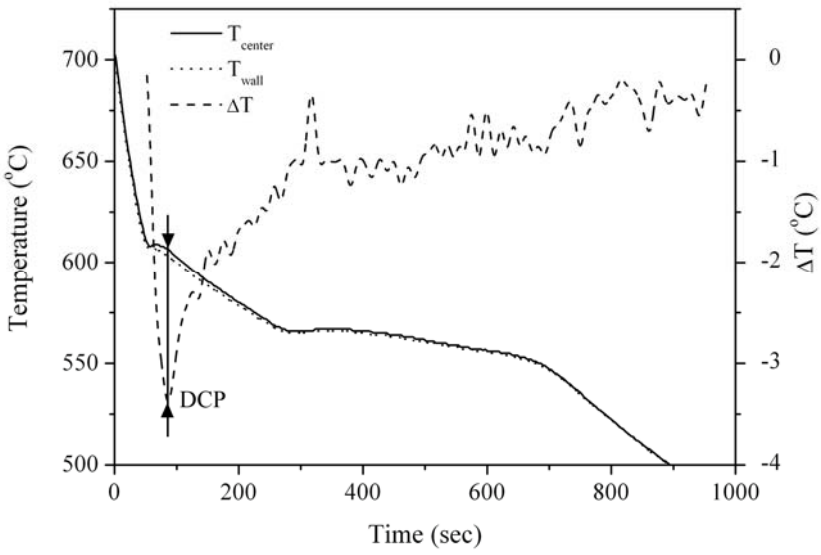

Figure 3.1 Cooling curves obtained from the center (T_{center}) and wall (T_{wall}) thermocouples and the *ΔT* curve for an A356 alloy reinforced with 20% SiC_p. The first minimum in the *ΔT* curve is taken as the dendrite coherency point (DCP).

CHAPTER 4

MODELLING OF MMC SOLIDIFICATION

The present study is aimed at building a comprehensive approach to MMC solidification to assess the as-cast microstructure and reinforcement distribution. Predicting the cluster formation tendency in a part before casting would provide a distinct advantage due the significant savings in prototyping and production costs. Such an ability would also help engineers to come up with new designs to produce these parts with a more uniform microstructure and therefore less prone to failure.

The distribution of second phase particles during solidification is determined by the primary dendrites. Subsequent reactions after dendritic solidification, such as the eutectic reaction or solidification of various intermetallic phases do not yield any influence on the final arrangement of particles, since the particles are already stabilized within the solid network of dendrite arms during the period of these transformations. Therefore, an attempt to assess the as-cast particle distribution through numerical simulations should concentrate on predicting the local solidification rate, since the dendritic spacings (both primary and secondary) are functions of the local cooling rate[47].

The main focus of the present work regarding the solidification process is, therefore, correct prediction of cooling curves at various locations within the casting as a function of casting geometry. The coupling of macrotransport equations with solidification kinetics was achieved through the latent heat method. The ripening of secondary dendrite arms was described by a dynamic coarsening model.

4.1 Theoretical Formulation of Macroscopic Heat Transfer

The main issue in continuum modelling of solidification process is to simultaneously solve the mass, energy and momentum transport equations. The standard transport equation for advection-diffusion is[48]

$$\frac{\partial}{\partial t}(\rho\phi) + \nabla(\rho\mathbf{V}\phi) = \nabla(\rho\gamma\nabla\phi) + S \tag{4.1}$$

where t is time, ρ is density, ϕ is the phase quantity, $\mathbf{V}$ is the velocity vector, γ is the general diffusion coefficient and S is source term. However, as far as the casting solidification is concerned, the entire process is primarily controlled by diffusion of heat and, to a small extent, convection in the liquid[49]. Therefore, neglecting the diffusion of species (i.e. constant density) and momentum transfer ($\mathbf{V} = 0$) the transport equation can be written in terms of temperature rather than enthalpy as

$$\frac{\partial T}{\partial t} = \alpha\nabla^2 T + \frac{\dot{Q}}{\rho c_p} \tag{4.2}$$

where T is temperature, α is the thermal diffusivity, c_p is the specific heat and $\dot{Q}$ is the heat source term. This source term represents the latent heat released during solidification and is given by

$$\dot{Q} = \Delta H_f \frac{\partial f_S}{\partial t} \tag{4.3}$$

where ΔH_f is the latent heat of fusion and f_S is the solid fraction. During the experimental studies, the composites were cast into cylindrical molds with insulation in the axial surfaces to ensure the heat transfer to occur in radial coordinates. In order to simulate the experimental conditions, composites were assumed to solidify in sand molds with cylindrical cavities and with zero heat flux in θ and z directions. The definition of cylindrical coordinates is presented in Fig 4.1. The equation for transient heat conduction is given by

$$\rho c_p \frac{\partial T(r,t)}{\partial t} = k \frac{1}{r} \frac{\partial}{\partial r}\left(r \frac{\partial T(r,t)}{\partial r} \right) + \Delta H_f \frac{\partial f_s(r,t)}{\partial t} \tag{4.4}$$

where, r is the radial coordinate and k is the thermal conductivity. In order to solve this equation, the evolution of solid, $f_S(r, t)$ must be described as a function of time and location inside the casting. This can be achieved through various schemes for coupling of the macroscopic heat flow with the microscopic solidification kinetics[50, 51]. In the present study, the latent heat method (LHM)[52] was used to incorporate the latent heat release during phase transformation to the macroscopic heat transfer. Heat transfer was assumed to be controlled by the resistance at the metal/mold interface and a prescribed flux boundary condition was used to account for the transfer at the interface[48].

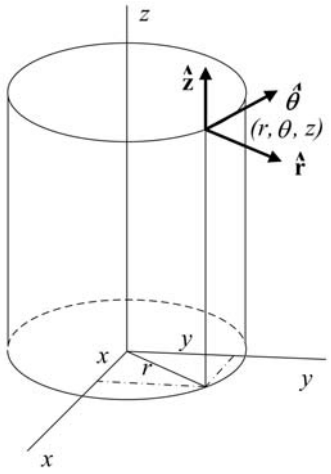

Figure 4.1 Definition of $\hat{r}$, $\hat{\theta}$ and $\hat{z}$ directions in cylindrical coordinates.

4.2 Microscopic Modelling

4.2.1 Pseudo-Binary Alloy Assumption: Calculation of Equivalent Solute

Formation of intermetallic phases at the later stages of eutectic solidification does not have any influence on the as-solidified particle distribution. Therefore, for the ease of calculations, it was assumed that solidification of the A356 matrix alloy results in two distinct microstructural regimes; the equiaxed α-Al dendrites and the eutectic phase. The silicon equivalency (Si_{eq}) method[53] was used to treat the A356 alloy as a pseudo-binary Al-Si_{eq} alloy. The Si_{eq} value expresses the amount of alloying elements other than Si (only 0.35% Mg in this case) in terms of an equivalent amount of silicon by the following expression

$$Si_{eq} = Si + \sum Si_{eq}^{X_i} \tag{4.5}$$

where, X denotes the alloying elements other than Si. The $\sum Si_{eq}^{X}$ values for some major and minor alloying elements and the resulting depression in the liquidus temperature are presented in Table 4.1.

Table 4.1 $Si_{eq}^{X_i}$ (wt%) values and the resulting liquidus depression (ΔT_L) of some alloying elements for 3XX aluminum alloys[53].

	Alloying elements (1wt%)									
	Cu	**Fe**	**Mg**	**Mn**	**Zn**	**Ni**	**Pb**	**Sn**	**Bi**	**Sr**
Si_{eq}	0.323	0.650	0.017	0.787	0.123	0.536	0.889	0.752	0.898	0.770
ΔT_L (°C)	1.98	4.00	0.10	4.84	0.75	3.29	5.47	4.63	5.53	4.74

4.2.2 Nucleation of α-Al Dendrites

It was assumed that solidification of the A356 matrix alloy results in two distinct microstructural regimes; the equiaxed α-Al dendrites and the eutectic phase. It was previously reported[2] that the SiC particles are not suitable substrates for nucleation of α-Al dendrites. Therefore, we have assumed that the presence of SiC particles have no influence on nucleation kinetics of the α-Al dendrites.

The nucleation models used in the present study are mainly intended for equiaxed solidification. Bulk nucleation heterogeneously takes place within the melt on foreign particles already existing in the liquid. A simple empirical instantaneous nucleation model was used to account for the nucleation of equiaxed α-Al dendrites in order to avoid computational complications related to definition of the micro-volume element[48] as will be explained in the following section. The model assumes that all nuclei are generated at the nucleation temperature (Fig 4.2a) and the nucleation site density is determined by the cooling rate at the onset of solidification. The governing equation is given by

$$N_s = a + b\left(\frac{\partial T}{\partial t}\right)^2 \tag{4.6}$$

where, N_s is the volumetric nucleation site density and a and b are experimentally determined constants[54].

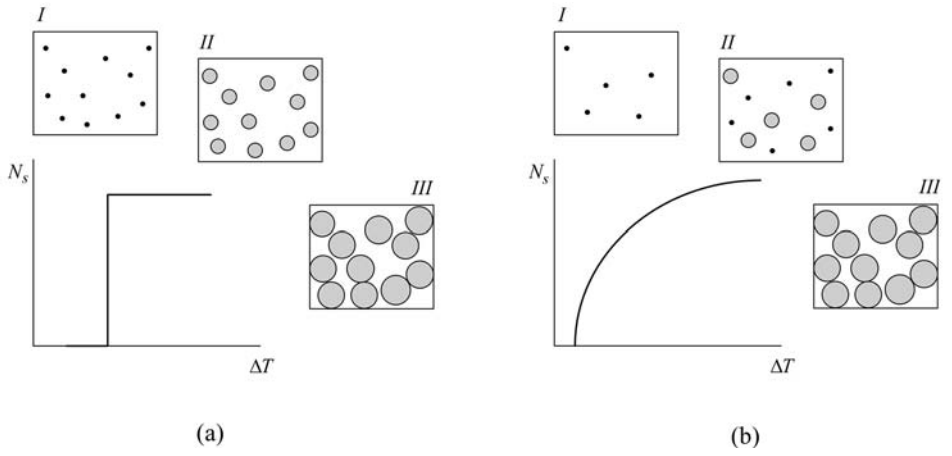

Figure 4.2 Schematic comparison of (a) instantaneous and (b) continuous nucleation models[48].

4.2.3 Dendritic Growth

There is still no complete theoretical solution that can describe the complexity of dendrite growth[48]. Although the diffuse interface approaches[55] (also known as the phase field method) can handle the morphological evolution of a dendrite quite successfully, they have limited applicability in terms of engineering usefulness. Furthermore, focusing on morphological evolution of each dendrite in a three dimensional space would require excessive computational capabilities, which does not seem possible at the current state of the art. Therefore, for the problem under consideration in this study, we have employed a simplified volume averaged dendrite model[48].

The schematic representation of the volume average model for an equiaxed condensed dendrite is given in Fig. 4.3. The dendrite envelope defines a pseudo-interface that separates the intradendritic and extradendritic liquid phases. It embraces the solid phase and the intradendritic liquid. The equivalent dendrite envelope (r_E), on the other hand, defines a spherical volume identical to the dendrite envelope. This volume also includes the solid and the intradendritic liquid. For further ease of calculations, this volume can be assumed as approximately equal to the volume of solid phase. Therefore, the growth rate of the condensed dendrite can be described over an averaged volume of sphere. The growth proceeds until all micro-volume element is filled, which has a radius of r_f.

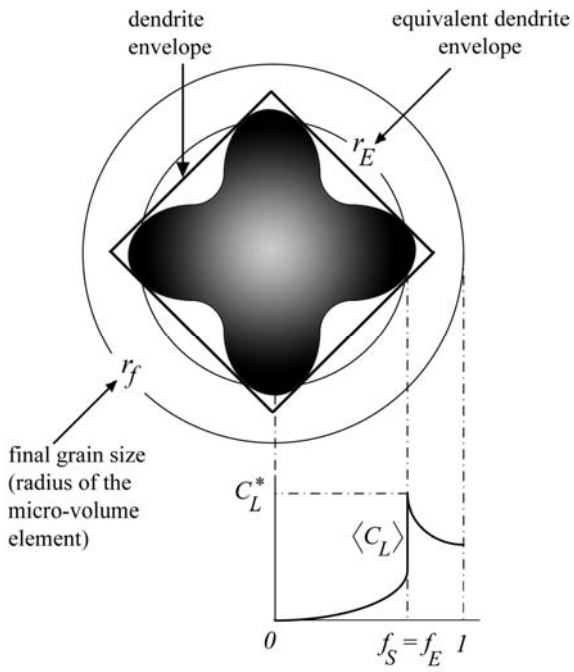

Figure 4.3 Schematic representation of assumed morphology and the associated concentration profile of globular equiaxed dendrites as given by Nastac and Stefanescu[56].

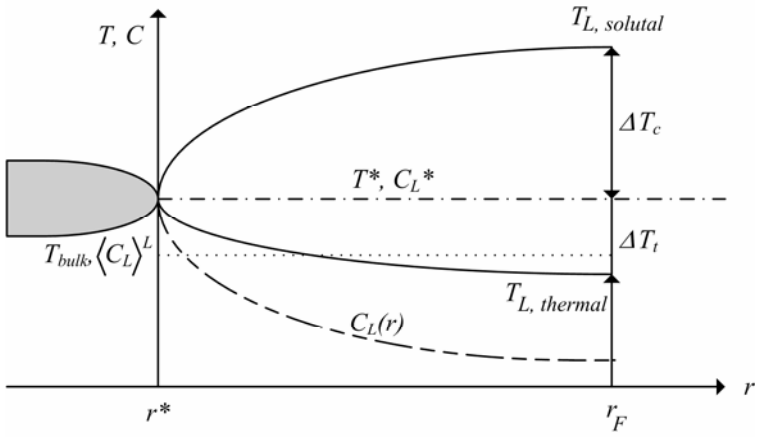

Figure 4.4 The concentration and temperature profiles ahead of the dendrite tip. ΔT_c and ΔT_t shows the solutal and thermal undercoolings, respectively. $\langle C_L \rangle^L$ is the intrinsic volume average concentration[56].

The growth rate of the equiaxed dendrites was calculated by the model developed by Nastac and Stefanescu[56] which relies on the melt undercooling at the dendrite tip (Fig. 4.4), which is given by

$$\Delta T = \Delta T_c + \Delta T_t \tag{4.7}$$

where ΔT_c and ΔT_t are the solutal and thermal undercoolings, respectively. The governing equation to describe the mean growth velocity of the dendrite tip is given by Eq. (4.8). The original derivation is given by Nastac and Stefanescu[56].

$$V_s = \left[2\pi^2 \Gamma \left(\frac{m(\kappa - 1)C_L^*}{D_L} + \frac{\Delta H_f}{c_p \alpha_L} \right) \right]^{-1} \cdot \Delta T^2 \tag{4.8}$$

where, m is the liquidus slope, κ is the partition coefficient, C_L* is the liquid interface concentration, D_L is the liquid diffusion coefficient, Γ is the Gibbs-Thomson coefficient, α_L is the liquid thermal diffusivity and ΔT is the undercooling. The melt undercooling is calculated by a linear liquidus assumption;

$$\Delta T = T_m + m\langle C_L \rangle - T_{bulk} \tag{4.9}$$

where, T_m is the melting point of pure aluminum, $\langle C_L \rangle$ is the volume average extradendritic liquid concentration and T_{bulk} is the average temperature in the volume element (see Fig. 4.4).

4.2.4 Eutectic Nucleation

The eutectic microconstituent may form by heterogeneous nucleation on the primary phase or as independently nucleated equiaxed grains on nucleant particles in the interdendritic liquid[57]. However, the literature reports contradictory results on whether the SiC particles could act as nucleants for heterogeneous nucleation of the eutectic phase.

Although SiC particles were previously reported[58, 59] as suitable substrates for heterogeneous nucleation of the eutectic phase, Nagarajan *et al*[59] did not detect any significant alteration in the eutectic undercooling due to presence of SiC particles. For the ease of calculations, following the method of Gonzalez-Rivera *et al*[54], we have assumed that the eutectic phase forms only as independently nucleated equiaxed grains. This assumption leads to prediction of higher eutectic growth rates than the actual case, which was compensated by a suitable impingement treatment, as will be explained in the following section.

A continuous nucleation model (Fig. 4.2b) was adopted to account for the nucleation of eutectic grains in order to obtain a more realistic impression of eutectic undercooling and recalescence periods on the simulated cooling curves. Oldfield's empirical model[60] was used to describe the nucleation site distribution. The governing equation is given by

$$\frac{\partial N_s}{\partial t} = -n\mu_N \left(\Delta T\right)^{n-1} \frac{\partial T}{\partial t}\left(1 - f_S\right) \tag{4.10}$$

where, μ_N is a nucleation parameter, $n = 2$ and the term $(1 - f_S)$ was included to account for the residual volume fraction of liquid.

4.2.5 Eutectic Grain Growth and Impingement

The growth of the equiaxed eutectic grains was calculated by using the Johnson-Mehl model[61]

$$V_s = \frac{\partial R}{\partial t} = \mu_{eut} \Delta T_{eut}^2 \tag{4.11}$$

where, R is the grain radius, μ_{eut} is the eutectic growth constant and ΔT_{eut} is the eutectic undercooling. Since the equiaxed grains have spherical morphology, the evolution of solid fraction can be described by[48]

$$\frac{\partial f_S}{\partial t} = 4\pi\left(\frac{\partial N_s}{\partial t}\frac{R^3}{3} + N_s r^2 \frac{\partial R}{\partial t}\right)(1-f_S)^{\Psi f_S} \tag{4.12}$$

The effect of grain impingement was considered by weighting the effective area between the solid grains and liquid by the term $(1-f_S)^{\Psi f_S}$ in Eq. (4.12) with $\Psi = 3$. This correction is analogous to previous approximations by Johnson-Mehl[61] and Avrami[62]. Ψ is a constant introduced to account for the delay in the eutectic growth rate[54] due to impingement of growing eutectic grains with each other, with the preexisting primary dendrites and also with the reinforcing SiC particles.

4.2.6 Coarsening of Secondary Dendrite Arms

The main aim of the numerical studies in this work is to estimate the secondary dendrite arm spacing distribution in a casting as a function of local cooling rate. Therefore, special emphasis will be given to this section and the applied model will be described in more detail.

The secondary arms are morphological instabilities or branches that grow perpendicular to the primary trunk. Although in early theories of dendritic solidification it was assumed that the secondary arms form in beginning of dendritic solidification and grow cooperatively with the primary trunk, it has later been recognized that the secondary arms coarsen with a mechanism analogous to Oswald ripening process in precipitate growth[63]. During coarsening of secondary dendrite arms, smaller branches shrink and melt and remaining larger branches continue their growth. The main reason behind this phenomenon is the effect of curvature on the liquidus temperature and the concentration profiles along the surfaces of these instabilities.

As the dendrite arm gets smaller, the contribution of the surface energy to the free energy of the solid phase increases due to increasing surface energy to volume ratio. This increment in free energy results in a depression in the equilibrium melting temperature of the solid phase (Fig. 4.5). Therefore, the smaller dendrite arms with higher curvature and therefore lower melting point dissolve to the melt and eventually disappear, whereas; the

larger arms continue their growth. This phenomenon is known as the dynamic coarsening of secondary dendrite arms[48].

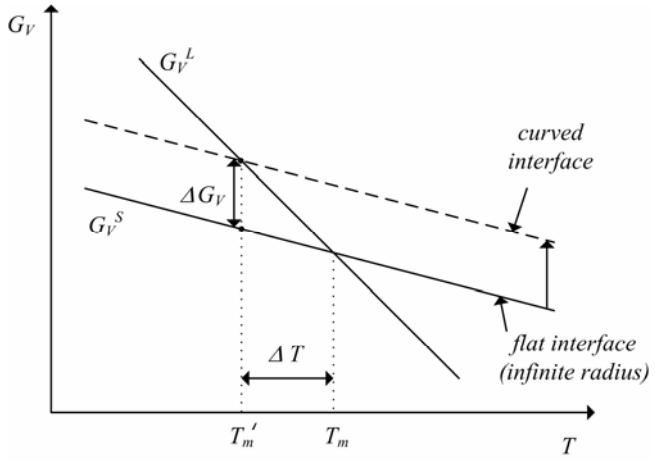

Figure 4.5 Variation of free energy of the solid and liquid phases as a function of temperature. Additional surface due to curved interface results in a depression in the equilibrium melting temperature of the solid phase by ΔT[66].

The coarsening of secondary arms is a diffusion controlled process. It is well established that the secondary dendrite arm spacing can be related to the solidification time by the empirical relationship

$$\lambda_2^3 = \mu_0 t_f \tag{4.13}$$

where, λ_2 is the secondary dendrite arm spacing, t_f is the solidification time and μ_0 is the coarsening constant. The correct prediction of as-solidified arm spacings depends on the derived expressions of μ_0. Various derivations of μ_0 were previously proposed in the literature[63-65]. In the present study, the dynamic coarsening model developed by Mortensen[65] was used. The governing derivation in the following pages is for array of coarsening cylinders, which represents the secondary dendrite arms, held at a constant holding temperature, T_{hold}, for a certain time, t.

As the dendrites grow, the secondary arms also get thicker. The average diameter of the dendrite arms, Φ, therefore can be represented as a function of fraction solid formed. The governing relationship is

$$\Phi = \lambda_2 \sqrt{f_s} \tag{4.14}$$

where f_s is the solid fraction. Since under isothermal conditions the solid fraction remains constant, the rate of thickening of the arms can be expressed by

$$\frac{d\Phi}{dt} = \sqrt{f_s}\frac{d\lambda_2}{dt} \tag{4.15}$$

While other approximations cited above generally focus on dissolution time of small dendrite arms into the melt, the Mortensen's model focuses on the fraction of dendrites that continue their growth. Some fraction of dendrites, F, is assumed to continue their growth, while others shrink. If the diameters of the growing and shrinking arms are denoted as Φ_g and Φ_s, respectively; then the average dendrite arm diameter can be given by the following relationship

$$\Phi = F\Phi_g + (1-F)\Phi_s \tag{4.16}$$

Assuming $F \approx 0.5$ and $\Phi_g \approx 2\Phi_s$ and combining Eqns. (4.14) and (4.16); we have

$$0.75\Phi_g = \lambda_2 \sqrt{f_s} \tag{4.17}$$

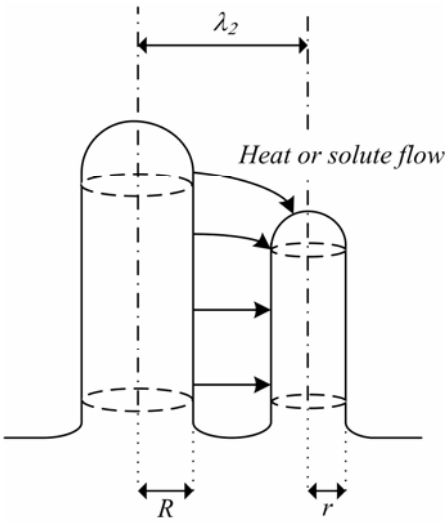

(a)

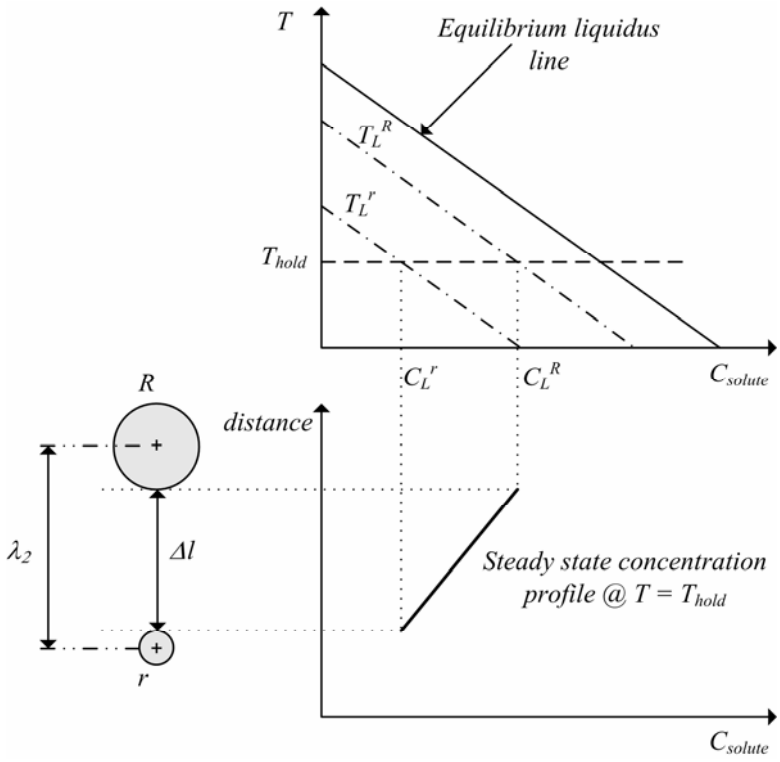

(b)

Figure 4.6 Schematic illustration of the situation between two solid cylinders of different radii, placed in a locally isothermal melt.

Fig. 4.6 illustrates the situation between two solid cylinders of different radii placed in a locally isothermal melt. Due to effect of curvature, (see Fig. 4.5) the two cylinders will have different liquidus temperatures and hence, the concentration along the surfaces of these cylinders will also be different. The surface of the cylinder with smaller radius will be at a lower solute concentration. Therefore, the solute will diffuse along the concentration gradient from the larger to smaller cylinder, while the solvent atoms will diffuse from the smaller to larger cylinder. As a consequence, the smaller cylinder will dissolve to the melt, while the larger cylinder will continue its growth. If it is assumed that the spacing between these cylinders are sufficiently small and the coarsening rate is sufficiently low so that local equilibrium is established between them, then the solute flux from the larger to smaller cylinder and solvent flux from the smaller to larger cylinder are given by

$$J_{solute} = -D_L \frac{\partial C}{\partial x} \tag{4.18}$$

$$J_{solvent} = -C_L^r (1-\kappa) \frac{1}{2} \frac{d\Phi_s}{dt} \tag{4.19}$$

where κ is the partition coefficient. Now, if we assume that the difference between surface concentrations is very small so that $C_L^r = C_L^R = \langle C_L \rangle$, where $\langle C_L \rangle$ is the average liquid concentration, by combining Eqns. (4.18) and (4.19) and writing the flux of the solvent for the growing arms, we obtain the expression for the thickening rate of the larger arms;

$$\frac{1}{2} \frac{d\Phi_g}{dt} = -\frac{D_L}{(1-\kappa)\langle C_L \rangle} \frac{\partial C}{\partial x} \tag{4.20}$$

The rate at which the larger sphere coarsens is therefore a function of the concentration gradient; that is the term $\partial C/\partial x$ in Eqn (4.20), which in turn depends on the amount of depression in liquidus temperatures (see Fig. 4.5). The liquidus temperatures at the surfaces of the cylinders are given by Kurz and Fisher[63] as

$$T_L^r = T_m + mC_L^r - \frac{2\Gamma}{\Phi_s} \tag{4.21}$$

$$T_L^R = T_m + mC_L^R - \frac{2\Gamma}{\Phi_g} \tag{4.22}$$

where T_m is the melting point of the solvent, m is the liquidus slope and Γ is the Gibbs-Thomson coefficient. Under isothermal conditions, combining Eqns. (4.21) and (4.22)

$$m\left(C_L^R - C_L^r\right) = \Gamma\left(\frac{2}{\Phi_s} - \frac{2}{\Phi_g}\right) \tag{4.23}$$

Therefore the concentration difference is

$$\Delta C = -\frac{2\Gamma}{m\Phi_g} \tag{4.24}$$

Combining Eqns. (4.17) and (4.24), the difference in concentration can be written as

$$\Delta C = -\frac{3\Gamma}{2m\sqrt{f_s}\lambda_2} \tag{4.25}$$

The average diffusion distance, Δl, in Fig. 4.6 is given by Mortensen[65] as

$$\Delta l = \left(1 - \sqrt{f_s}\right)\lambda_2 \tag{4.26}$$

Then, it can be estimated that

$$-\frac{\Delta C}{\Delta l} \approx -\frac{\partial C}{\partial x} = \frac{3\Gamma}{2m\lambda_2^2\left(1-\sqrt{f_s}\right)\sqrt{f_s}} \tag{4.27}$$

Combining Eqns. (4.17), (4.20) and (4.27) we obtain

$$\lambda_2^2 \frac{d\lambda}{dt} = \frac{9\Gamma D_L}{4m(1-\kappa)\langle C_L\rangle\left(1-\sqrt{f_s}\right)\sqrt{f_s}} \tag{4.28}$$

Integrating Eqn. (4.28) with in the interval of isothermal holding time, t_h,

$$\lambda_{2,f}^3 - \lambda_{2,0}^3 = \frac{27\Gamma D_L t_h}{4m(1-\kappa)\langle C_L \rangle \left(1-\sqrt{f_s}\right) f_s} = \mu_0 t_h \tag{4.29}$$

where $\lambda_{2,0}^3$ and $\lambda_{2,f}^3$ are the spacings between secondary arms at the beginning and end of the isothermal holding. Assuming that $\lambda_{2,0} << \lambda_{2,f} = \lambda_2$, the final secondary arm spacing is given by

$$\lambda_2^3 = \mu_0 t_f \quad \text{with} \quad \mu_0 = \frac{27\Gamma D_L}{4m(1-\kappa)\langle C_L \rangle \left(1-\sqrt{f_s}\right) f_s} \tag{4.30}$$

Eqn. (4.30) describes the coarsening of secondary arms under isothermal conditions. In order to integrate this equation to the actual process of solidification, one needs to know the functional dependence of the average liquid concentration and solid fraction with time[65]. The dependence of these variables to time was directly calculated from their corresponding alterations within the micro-volume element, which was presented in section 4.2.3, and implemented to Eqn. (4.30) to achieve the as solidified secondary dendrite arm spacing distribution within the casting.

CHAPTER 5

EXPERIMENTAL & COMPUTATIONAL DETAILS

5.1 Materials

5.1.1 Matrix Alloy

The matrix alloy chosen for the present study was A356 aluminum alloy due to its excellent castability and rather wide solidification range (see Appendix A). The composition limits of the A356 alloy are presented in Table 5.1. Typical applications are aircraft structures, machine parts, truck chassis parts and other structural applications requiring high strength.

Table 5.1 Composition limits of A356 aluminum alloy

Si	**Mg**	**Cu**	**Mn**	**Fe**
6.5% - 7.5%	0.25% - 0.45%	0.20% (max)	0.10% (max)	0.20% (max)
Zn	**Ti**	**Other (each)**	**Others (total)**	**Al**
0.10% (max)	0.20% (max)	0.05% (max)	0.15% (max)	Balance

5.1.2 The Reinforcement Phase

F320 type, green silicon carbide (SiC) particles with an average particle size of 29.2 ± 1.5 μm were used as the reinforcement phase. Table 5.2 presents the chemical and physical properties of the SiC particles. The surface chemical values of the particles are given in Table 5.3.

Table 5.2 Chemical and physical properties of the SiC particles

Crystal form:	α-SiC hexagonal
True density (kg m^{-3}):	3.20
Color:	Green
Decomposition point (°C):	2300
Hardness - Knoop (kg cm^{-2}):	2500 - 2900
Reaction with acids:	Very slight surface action with hydrofluoric acid
Oxidation-reduction:	Oxidation slowly starts at 800 °C. No reduction.

Table 5.3 Surface chemical values of F320 silicon carbide

Product	**%SiC**	**%Free C**	**% Si**	**%SiO_2**	**%Fe_2O_3**
F240 - F800	99.50	0.10	0.10	0.10	0.05

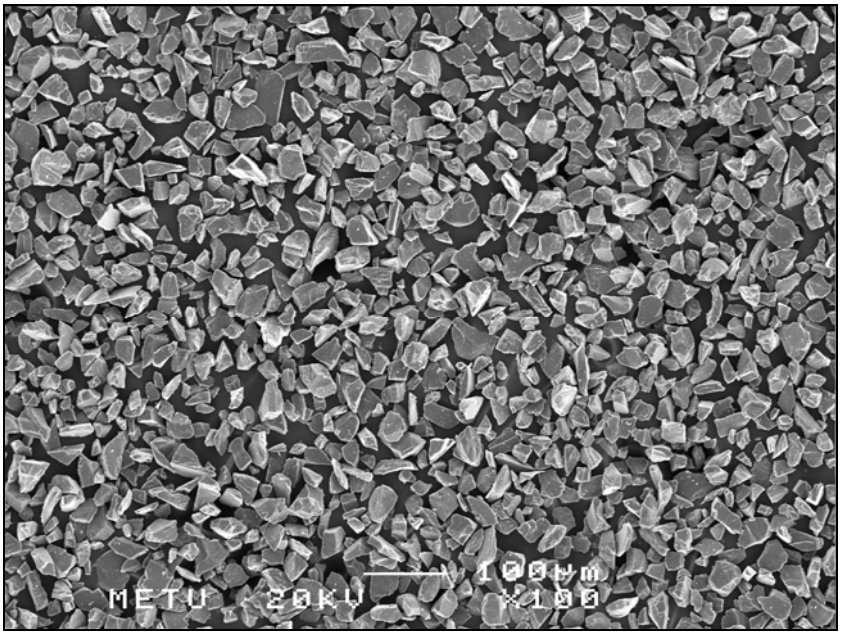

Figure 5.1 Morphology of SiC particles used in this work.

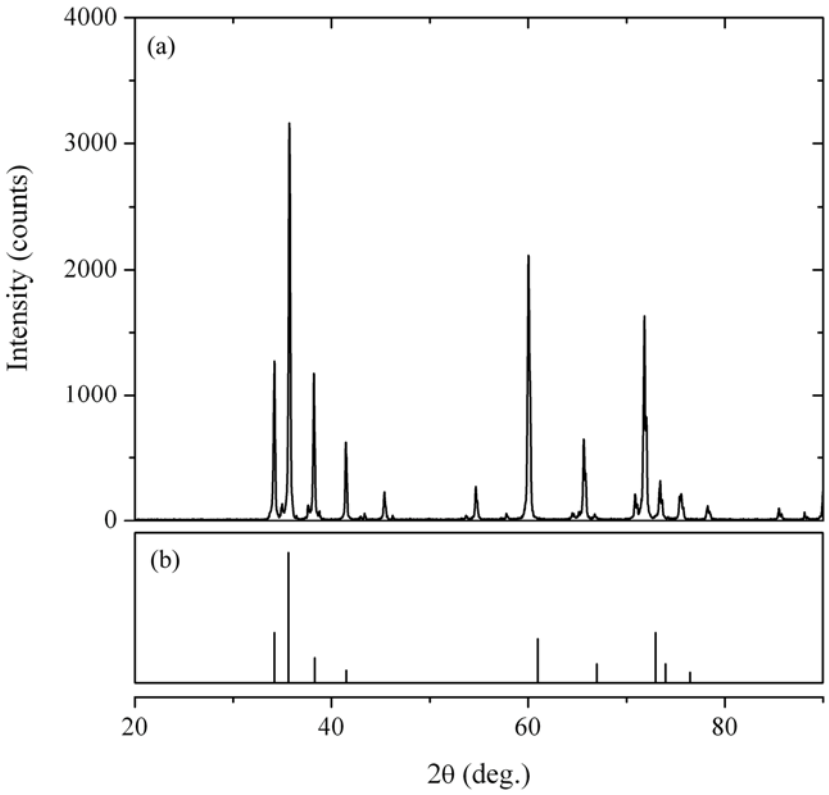

Figure 5.2 (a) X-ray diffraction pattern of the SiC particles and (b) standard powder pattern of 6H-SiC (JCPDS 29-1131).

Fig. 5.1 shows the morphology of the SiC particles used in this study. The X-ray diffraction pattern (Cu Kα) of reinforcement particles is shown in Fig. 5.2 with JCPDS (Joint Committee on Powder Diffraction Standards) data 29-1131 (6H-SiC).

5.2 Stir Casting of Aluminum Matrix Composites

The aluminum alloy matrix composites were synthesized by the double stir-casting method. A weighed quantity of high purity aluminum electrical wires were melted in a clay bonded graphite crucible and alloyed with required amount of silicon. After complete dissolution of silicon, the melt was degassed with high purity argon (99.998%) for 20 min with a flow rate of 5 liter per min. In order to improve the wettability of SiC particles[67], the melt was alloyed with 1% Mg and temperature was dropped below liquidus, to the semi-solid state. SiC particles, preheated at 300 °C for 2 hours were added to the slurry and manually stirred until the particles were completely wetted. The composite slurry was then reheated to T_L ± 5 °C, where T_L is the liquidus temperature, and stirred with a stainless steel four-blade impeller at 300 rpm for 15 minutes. The blades of the impeller were coated with a zirconia based suspension to avoid iron contamination of the melt. In order to compensate the oxidized magnesium during the stirring period, the melt was brought to fully liquid state and alloyed with required amount of magnesium to reach the nominal composition. Extreme care was taken for temperature control of the melt (720 ± 10 °C) during processing to avoid Al_4C_3 formation.

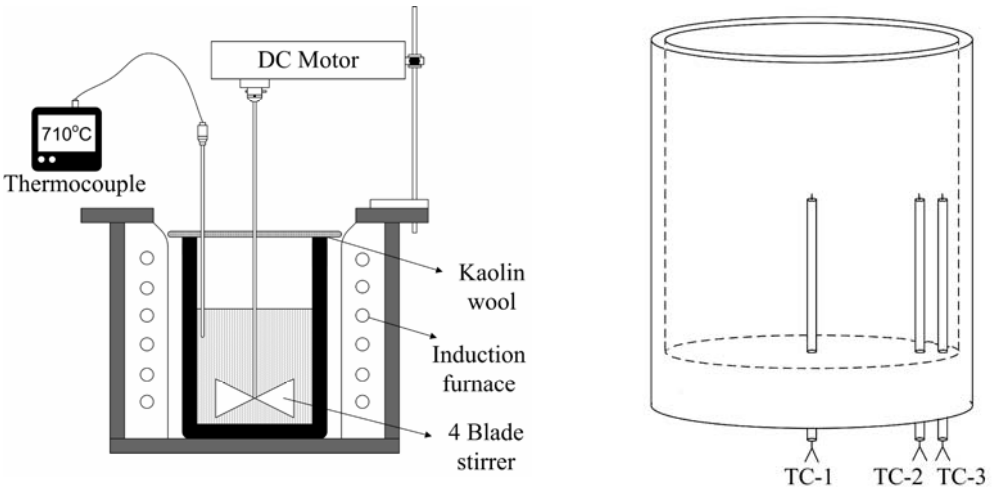

Figure 5.3 (a) Schematic diagram of the experimental setup for synthesis of aluminum matrix composites; (b) schematic of a typical cylindrical thermal analysis cup.

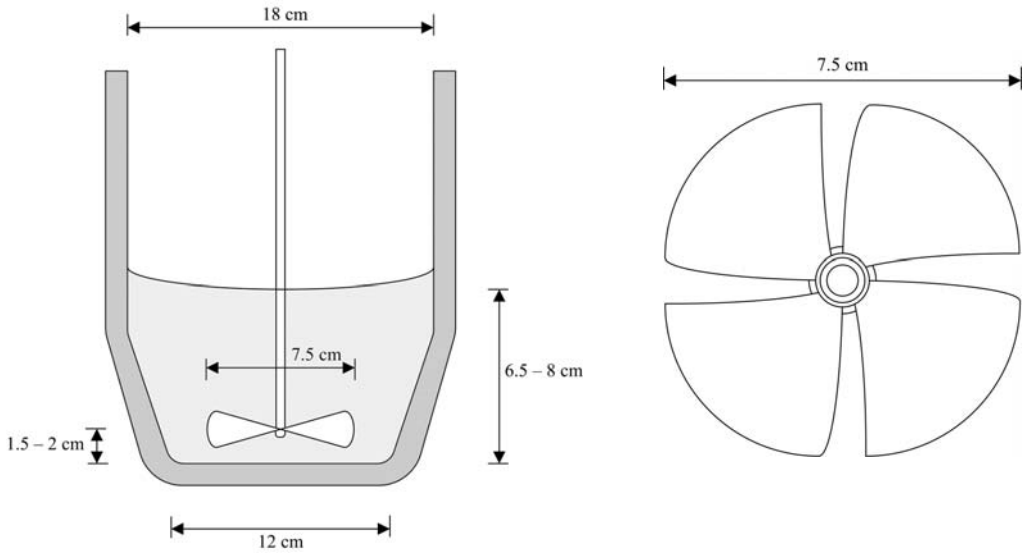

Figure 5.4 (a) Position of stirrer in the ladle; (b) schematic of the four-blade stirrer.

During production of samples, the amount of charge materials, stirring duration and position of stirrer in the crucible were almost kept constant to minimize the contribution of variables related to stirring on distribution of reinforcement particles. Fig 5.4 illustrates the position of the stirrer in the ladle and the schematic of the four-blade stirrer. In all experiments, the total amount of charge materials ranged between 1800 to 2400 gr, which resulted in a liquid metal height of 6.5 to 8 cm. Nagata[68] stated that, in order to avoid accumulation of particles at the bottom of the ladle, the position of the stirrer should not exceed 30% of the height of the liquid metal from the base. In all experiments, care was taken to position the stirrer 1.5 to 2 cm from the base to ensure uniform dispersion of particles within the liquid.

5.3 Thermal Analysis of MMC Solidification

The composites were poured into cylindrical resin-coated shell sand molds (see Fig. 5.3b) with varying dimensions (see Appendix B) to obtain different solidification rates and allowed to cool down to room temperature. The investigated range of solidification rates were between 0.164 and 2.417 °C sec^{-1}.

The temperature of the solidifying composites was monitored from three alumina sheathed K-type thermocouples placed inside each cylindrical mold. In each mold, one thermocouple was positioned at the geometrical center of the mold and the others at two different radial distances from the center and at the same vertical height as the center thermocouple (Fig. 5.3b). Apart from its suitability for both Fourier and Newtonian thermal analysis procedures, this set-up is also typical for estimation of dendrite coherency point (DCP) with two thermocouples, which is based on the temperature difference (ΔT) between the wall and center thermocouples[41].

The thermocouple tips were in direct contact with the liquid. The top and bottom surfaces of the cylindrical molds were isolated with layers of zirconia and kaolin wool placed on preheated ceramic plates to ensure the cooling of the samples only by heat transfer from the radial surfaces for estimation of dendrite coherency points and also to establish similar heat transfer conditions with the 2D computational algorithm presented in Chapter 4. The thermal data were obtained by recording the time and temperature values by using an Elimko multi-channel data acquisition system at a rate of 1 *Hz*. The recorded data were processed with a program developed in Mathcad environment (Mathsoft Eng. & Ed. Inc. v11), which allowed application of Newtonian (NTA) and Fourier thermal analysis (FTA) procedures, calculation of solid fraction (f_S) curves and estimation of dendrite coherency points (DCP). Solidification rate of the samples were calculated from the slopes of the cooling curves between liquidus and eutectic reactions, as received from the center thermocouples. The solidification rates were defined to be positive so that the calculated values indicate their magnitude.

The DTA measurements were carried out by the Setaram SETSYS DTA device already available in the Department of Metallurgical and Materials Engineering in METU. The investigated temperature range was from 660 to 480 °C, at a cooling rate of 10 °C min^{-1} under argon atmosphere.

5.4 Image Analysis

The solidified samples were sectioned and prepared for metallographic analysis. The Cartesian coordinates of the centroids of the SiC particles and the secondary dendrite arm spacing (SDAS) values were obtained by Clemex Image Analysis system. At least 20 random fields of each sample were analyzed to achieve the spatial and metallographic data and care was taken to avoid overlapping of the analyzed fields. The metallographic fields were 1376.3 × 1017.2 μm^2 in all cases (Fig. 5.5).

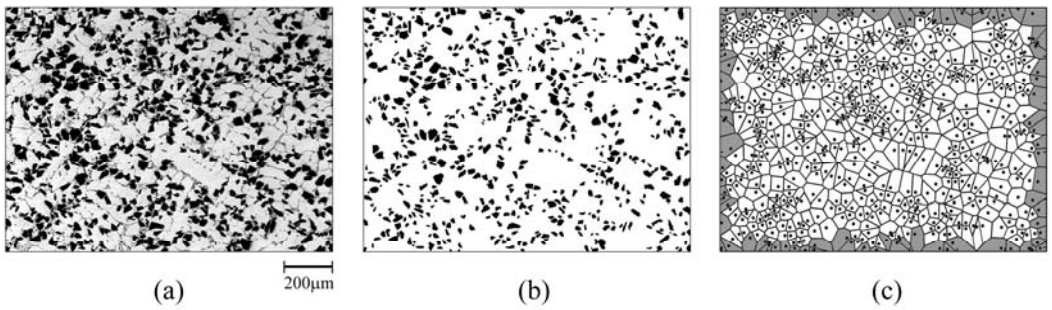

Figure 5.5 (a) An optical micrograph of sample no A2010; (b) selected SiC particles for quantitative analysis and; (c) centroids of SiC particles, presented with the Voronoi diagram.

In order to capture the long range spatial patterns and to analyze the effect of metallographic study area on the resulting statistics, the calculations were also performed on digital montages of contiguous microstructural fields. Fig. 5.6 shows such a montaged microstructure of an A356-20% SiC composite and a close-up image showing the high resolution of the image. The photographs of contiguous metallographic fields were collected and montaged with Adobe Photoshop CS2 image editor software. This procedure is necessary to capture relatively large microstructural fields that cannot be captured by an optical microscope with high resolution. The high resolution of the image is particularly important for the image analysis program to capture the microstructural details.

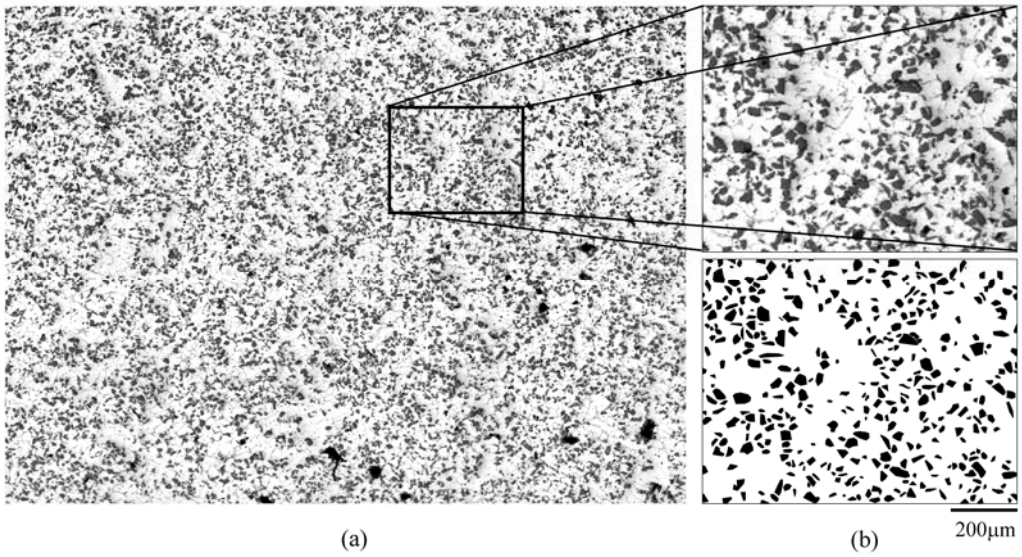

Figure 5.6 (a) A high resolution montage of contiguous fields from an A356 - 20% SiC composite microstructure; (b) a close-up image from the metallographic field, together with the binary image.

5.5 Computational Details

5.5.1 Quantitative Analysis of Particle Distribution

5.5.1.1 Computer generated point data

Computer simulated artificial distributions of events, where each event represents a reinforcement particle, were generated in order to test the response of applied statistical methods to various point patterns and levels of clustering. Three types of point processes; random (Poisson), regular and clustered were considered. Random event sets were generated by simulation of homogeneous Poisson process, in which the x and y coordinates were sampled from two independent uniform distributions within the boundaries of the study region, R. Inhibition model was used for regular event sets, which commences with generation of a Poisson distribution, followed by elimination of events that are found to be less than some specified distance, d, from their nearest-neighbour. The clustered event sets were generated by a three step Neyman-Scott cluster process. First, parent events were distributed according to a Poisson process with a pre-defined intensity. Then a number of events, obtained from a random distribution with mean μ were assigned to each parent. Finally, the assigned events were distributed around the parents according to a Gaussian probability distribution function centered on the parents and with standard deviation σ. In order to monitor the response of the applied functions to local variations in particle content, we have generated regular, random and clustered data sets with three different intensities. Each representative distribution was limited to a 1000 × 1000 square area and consisted of 150, 300 and 450 events. The clustered data sets were generated with varying μ and σ to test the robustness of the applied functions to alterations in clustering levels. Nine different clustered distributions were generated with the following properties:

- ✓ For 150 events: $\mu = 10$; $\sigma = 50, 100, 150$
- ✓ For 300 events: $\mu = 20$; $\sigma = 50, 100, 150$
- ✓ For 450 events: $\mu = 30$; $\sigma = 50, 100, 150$

5.5.1.2 Spatial analysis programs

Four different analysis methods were used in the present study; Voronoi tessellation, refined nearest neighbour analysis, K-function and the local density statistics. The Voronoi polygons for the set of coplanar points, which represent the centroids of SiC particles, were first determined with MATLAB (The Mathworks, Inc. v7). Area distribution of the resulting cells was evaluated by Clemex image analysis software. The polygon areas could also be determined by the inbuilt function 'polyarea' in MATLAB. However, since the 'polyarea' function also takes the marginal polygons into consideration and makes no edge correction; the analysis ends up with incorrect results. In order to overcome this problem, the marginal polygons were eliminated and the area distributions were evaluated via the image analysis software. A set of programs developed in-house by the author were used for the refined nearest neighbour analysis, *K*-function and the local density statistics. All programs were developed in Mathcad environment (Mathsoft Eng. & Ed. Inc. v11).

5.5.2 Macrotransport – Solidification Kinetics Modelling

A program developed by the author was used for numerical assessment of composite solidification. The program calculates the evolution of fraction of solid during the course of solidification and couples the calculated evolution with the governing macrotransport equations. The coupling was achieved through the latent heat method (LHM)[52]. The flowchart of the coupling procedure is given in Fig. 5.7. The numerical parameters used in simulations and thermal analysis are presented in Table 5.3.

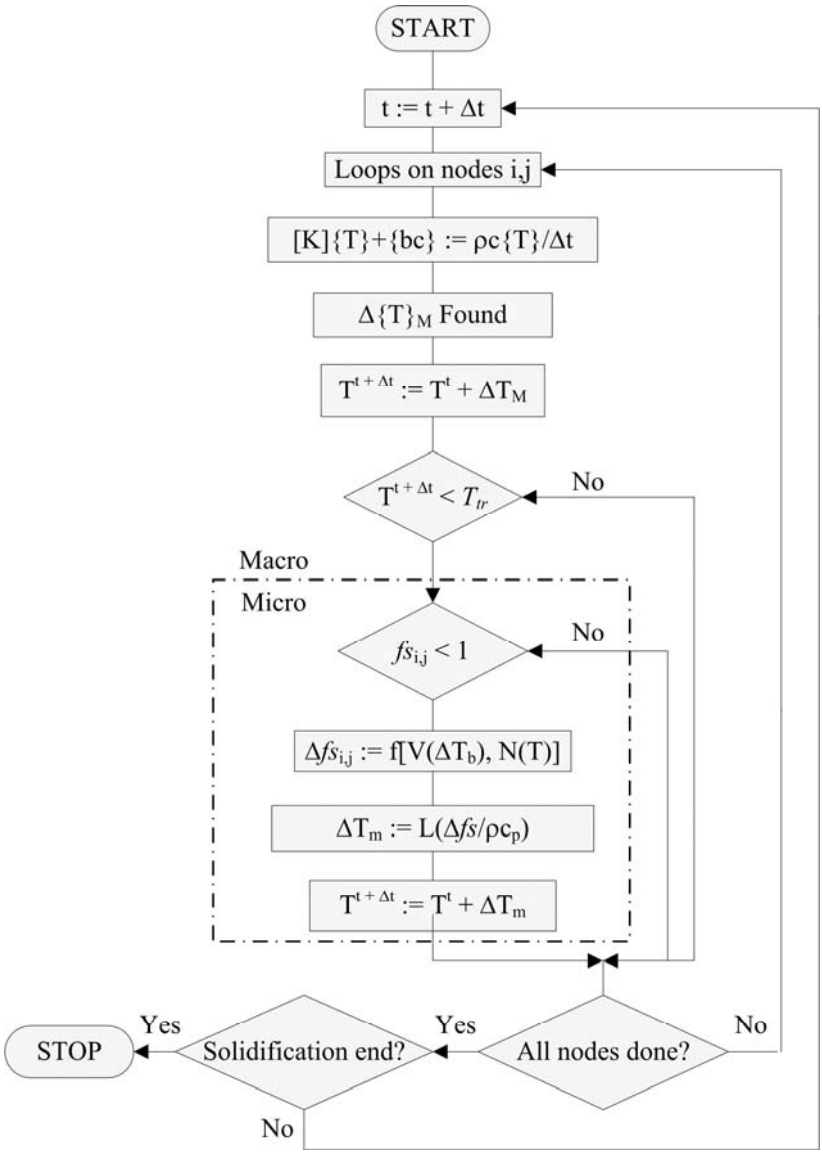

Figure 5.7 Basic flowchart of macrotransport – solidification kinetics coupling algorithm by latent heat method (LHM)[52].

Table 5.3 Selected data used in simulations and in thermal analysis of composites.

Quantity	Value	Unit
Mold (shell sand)		
Density	$\rho_m = 1600$	kg m^{-3}
Thermal conductivity	$k_m = 0.52$	W m^{-1} °C^{-1}
Specific heat	$c_{p,m} = 1170$	J kg^{-1} °C^{-1}
Matrix(A356) - Reinforcement (SiC)		
Solid density	$\rho_S = 2700$	kg m^{-3}
Liquid density	$\rho_L = 2400$	kg m^{-3}
Particle density	$\rho_P = 3200$	kg m^{-3}
Solid specific heat	$c_{p,S} = 1084$	J kg^{-1} °C^{-1}
Liquid specific heat	$c_{p,L} = 963$	J kg^{-1} °C^{-1}
Particle specific heat	$c_{p,P} = 1300$	J kg^{-1} °C^{-1}
Solid thermal conductivity	$k_S = 159$	W m^{-1} K^{-1}
Liquid thermal conductivity	$k_L = 121$	W m^{-1} K^{-1}
Particle thermal conductivity	$k_P = 250$	W m^{-1} K^{-1}
Latent heat (Pure Al)	$\Delta H_f^{\alpha} = 3.91\times 10^5$	J kg^{-1}
Latent heat (Eutectic)	$\Delta H_f^{eut} = 5.63\times 10^5$	J kg^{-1}
Partition coefficient	$\kappa = 0.132$	
Liquidus slope	$m = -6.656$	°C $wt\%^{-1}$
Liquid diffusion coefficient	$D_L = 3\times10^{-9}$	m^2 s^{-1}
Gibbs-Thomson coefficient	$\Gamma = 0.9\times10^{-7}$	m °C
Nucleation and Growth		
Primary nucleation parameter	$a = 3.57\times10^9$	m^{-3}
Primary nucleation parameter	$b = 2.3\times10^7$	s^2 m^{-3} °C^2
Eutectic nucleation parameter	$\mu_N = 1\times10^6$	m^{-2} °C^{-2}
Eutectic growth constant	$\mu_{eut} = 5\times10^{-6}$	m s^{-1} °C^2

CHAPTER 6

RESULTS & DISCUSSION

The present work aims to study the clustering of reinforcement particles in metal matrix composites through experimental studies and numerical simulations. The scope of the study consists of (i) understanding the effect of solidification rate on clustering of reinforcement particles; (ii) studying suitable statistical descriptions of composite microstructures that can successively quantify the amount of particle clustering and (iii) establishing a model that predicts the cluster formation tendency in complex geometry cast parts.

Prediction of clustering is an important issue for two reasons. Firstly, being able to predict the cluster formation tendency in complex geometry cast parts before production would help the engineers to come up with new designs to produce these parts with a more uniform microstructure and therefore less prone to failure. The second benefit would be for the modelling studies aimed at predicting the mechanical response of complex composite parts with varying section thicknesses produced by solidification processing. Until now, such studies could only introduce the effect of particle clustering by some scalar descriptions. However, being able to predict and describe the particle distribution as a function of solidification rate would offer the possibility to consider the effect of local microstructural features as well.

The first section to be presented in this chapter concerns the thermal analysis results. The aim of the thermal analysis studies is to describe the evolution of solid fraction during the course of solidification and estimate the dendrite coherency points. The former also holds significance in verifying the numerical model, which describes the solidification of composites. The results regarding the quantitative analysis of particle

distribution will be presented in the following section, which will be followed by the effect of solidification rate on as-solidified particle distribution and the results of the numerical analysis study. As described previously, the aim of the numerical analysis study is to establish a model that can predict the solidification microstructures, which determines the as-cast particle distribution.

6.1 Thermal Analysis of Composite Solidification

Distribution of SiC particles was evaluated in terms of two parameters related to primary solidification of composites; secondary dendrite arm spacing (SDAS) and volume fraction of solid phase at the dendrite coherency (f_S^{DCP}). Secondary dendrite arm spacing is a function of local cooling rate and is known to decrease as the cooling rate increases[47]. The volume fraction of the solid phase at the dendrite coherency, on the other hand, depends on the evolution of microstructure during the course of solidification. Refinement of the dendritic structure postpones the coherency whereas; increased growth rate results in an earlier formation of the dendritic skeleton[44, 69-72]. From a macro-scale point of view, one could expect earlier occurrence of coherency with an increase in the magnitude of cooling rate as a result of increased volumetric transformation rate. However, an increase in the magnitude of cooling rate also results in refinement of the dendritic structure due to increased undercooling. Therefore, the solid fraction at which coherency occurs is actually determined by the competition between these two processes with counteracting effects[44, 72].

In order to obtain the variation of solid fraction during the course of solidification, the thermal data obtained from various locations within the cylindrical molds were processed according to Newtonian (NTA) and Fourier (FTA) thermal analysis methods. Fig. 6.1 presents sample cooling curves, their derivatives, the zero curves and the solid fraction curves on the same time scale. The range of solidification rates investigated in the present study is tabulated in Table 6.1.

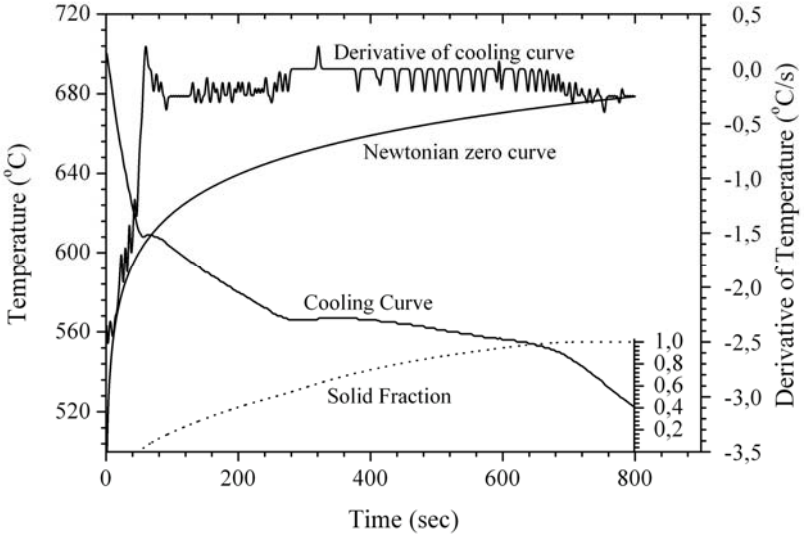

(a)

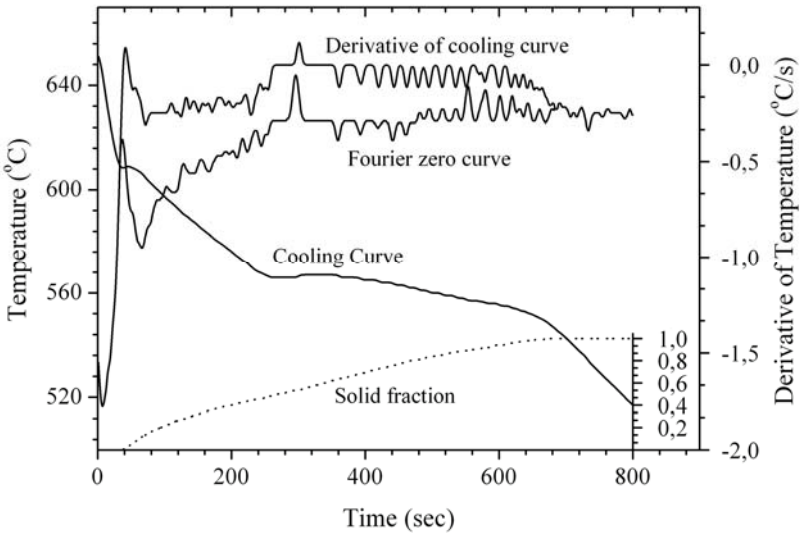

(b)

Figure 6.1 Sample cooling curves, derivative curves, zero curves and solid fraction curves obtained by (a) Newtonian and (b) Fourier thermal analysis methods for A356 alloy composites reinforced with 20% SiC particles.

Table 6.1 Range of investigated solidification rates.

SiC Content	Sample	SR (°C sec^{-1})	SiC Content	Sample	SR (°C sec^{-1})
10%	*A1001*	0.164	*20%*	*A2001*	0.213
	A1002	0.242		*A2002*	0.309
	A1003	0.280		*A2003*	0.353
	A1004	0.345		*A2004*	0.429
	A1005	0.411		*A2005*	0.566
	A1006	0.429		*A2006*	0.652
	A1007	0.596		*A2007*	0.698
	A1008	0.682		*A2008*	0.775
	A1009	0.725		*A2009*	0.806
	A1010	0.795		*A2010*	1.107
	A1011	0.981		*A2011*	1.211
	A1012	1.121		*A2012*	1.421
	A1013	1.329		*A2013*	1.861
	A1014	1.928		*A2014*	2.417
	A1015	2.319			

6.1.1 Evolution of Solid Fraction

The difference between the FTA and NTA lies in the way they generate the baselines, also known as the zero curves. Instead of NTA, which arbitrarily calculates the zero curve by some extrapolation or curve fitting techniques, in FTA the zero curve is obtained from the temperature Laplacian, $\nabla^2 T$. The extent of this difference can be seen on the generated zero curves in Fig. 6.1. The zero curve generated by the NTA exhibits a smooth trend during the course of solidification, since it is obtained by fitting of an exponential function. The zero curve generated by FTA, on the other hand, is a function of the cooling rate and temperature Laplacian and therefore exhibits similar trends with the derivative curve.

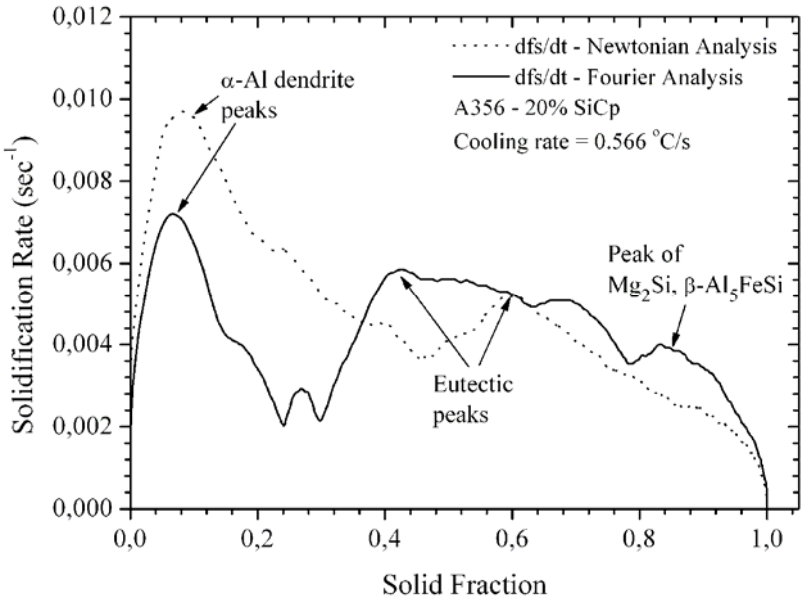

Figure 6.2 Comparison of solidification rates obtained from NTA and FTA methods.

The differences between the solid fraction (f_S) estimations of NTA and FTA can better be understood by close examination of solidification rates in Fig. 6.2. NTA calculates a higher solidification rate at the onset of solidification compared to FTA. Due to this difference within the interval of primary solidification of α-Al dendrites, the solid fraction values at the dendrite coherency point obtained from NTA and FTA also differs. The second peaks in Fig. 6.2 account for the eutectic solidification. FTA demonstrates another third peak corresponding to the solidification of intermetallic phases such as Mg_2Si and β-Al_5FeSi. The solidification of these phases cannot be monitored from the curve obtained from NTA. Formation of these phases was verified by DTA (Fig. 6.3) and also from the literature[73, 74].

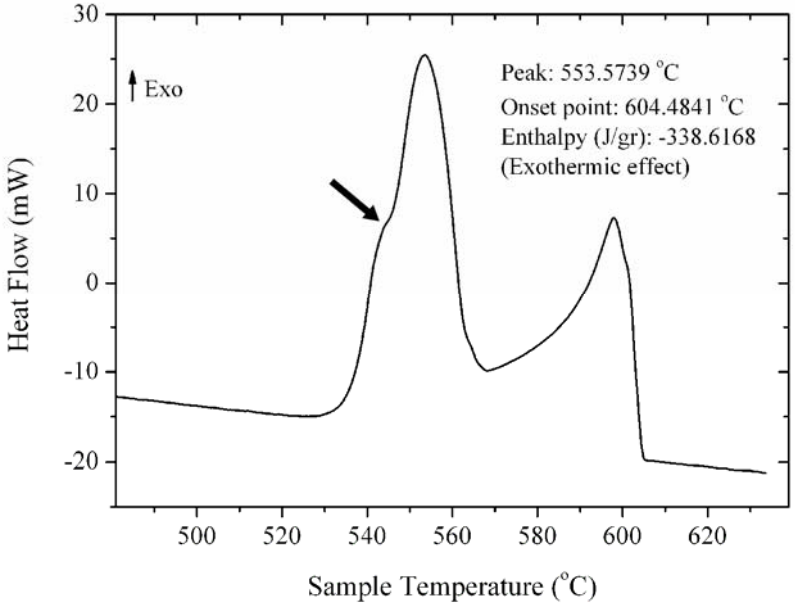

Figure 6.3 DTA curve of the A356 alloy. Cooling rate was 10 °C min^{-1}. The inflection indicated by the black arrow corresponds to solidification of intermetallic phases such as Mg_2Si and β-Al_5FeSi.

6.1.2 Comparison of Dendrite Coherency Point Estimations

As far as the as-cast particle distribution is concerned, formation of these intermetallics holds no importance. The main difference that needs to be underlined is the calculated solid fraction evolutions during dendritic solidification, since the distribution of reinforcement particles is determined during this interval. Therefore, it should again be noted that, NTA calculates a higher solidification rate at the onset of solidification compared to FTA. Consequently, the solid fraction values at the dendrite coherency point obtained from NTA generally, though not necessarily, corresponds to a higher solid fraction compared to FTA.

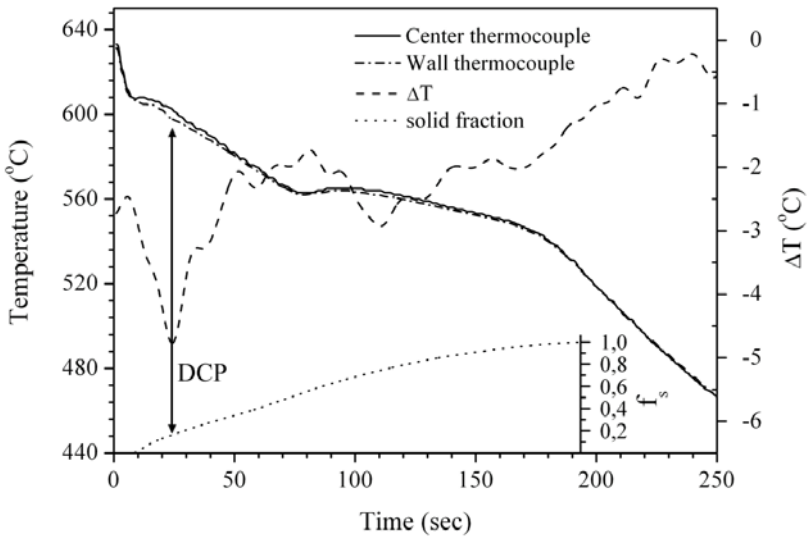

Figure 6.4 A typical output data: cooling curves obtained from center and wall thermocouples, the ΔT curve and the solid fraction curve for an A356 – 20% SiC_p composite, presented on the same time scale.

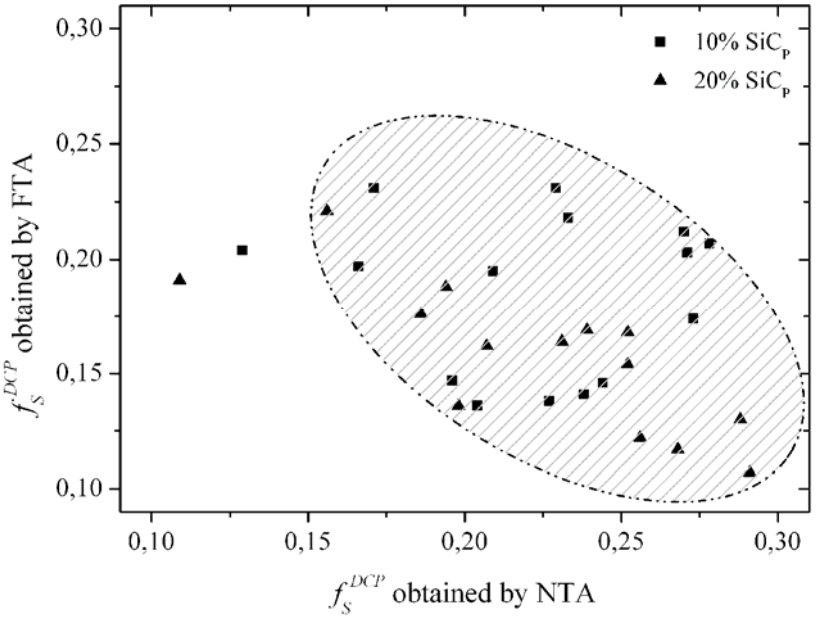

Figure 6.5 Calculated solid fractions at the dendrite coherency point by NTA and FTA.

Fig. 6.4 illustrates a typical f_S^{DCP} estimation procedure with two thermocouples. The solid fraction that corresponds to the first negative peak on the ΔT curve is accepted as the dendrite coherency point. Fig. 6.5 shows the comparison of f_S^{DCP} values by NTA and FTA. Although no clear relationships could be observed, the solid fractions calculated by NTA were found to correspond to higher values compared to FTA. This difference was also reported by Barlow and Stefanescu[40]. The shaded region in Fig. 6.5 is added to emphasize this tendency.

6.2 Quantitative Analysis of Particle Distribution

The spatial data obtained from composite microstructures were analyzed with various methods in spatial statistics to quantify the amount of particle clustering. The discussed methods are the refined nearest neighbour statistics, Voronoi tessellation, *K*-function and the local density statistics method. Series of point processes with known properties were simulated in order to explore the reaction of the aforementioned methods to various levels of clustering. The applicability of these methods to quantify composite microstructures was discussed.

6.2.1 Simulated Point Data

Computer simulated artificial distributions of events, where each event represents a reinforcement particle, were generated in order to test the response of applied statistical methods to various point patterns and levels of clustering. Three types of point processes; random (Poisson), inhibition (uniform) and clustered were considered. Summary statistics of the simulated events are presented in Table 6.2. The tabulated results are calculated from 200 simulations of each point process with 150, 300 and 450 events. Fig. 6.6 demonstrates some examples of the simulated point processes.

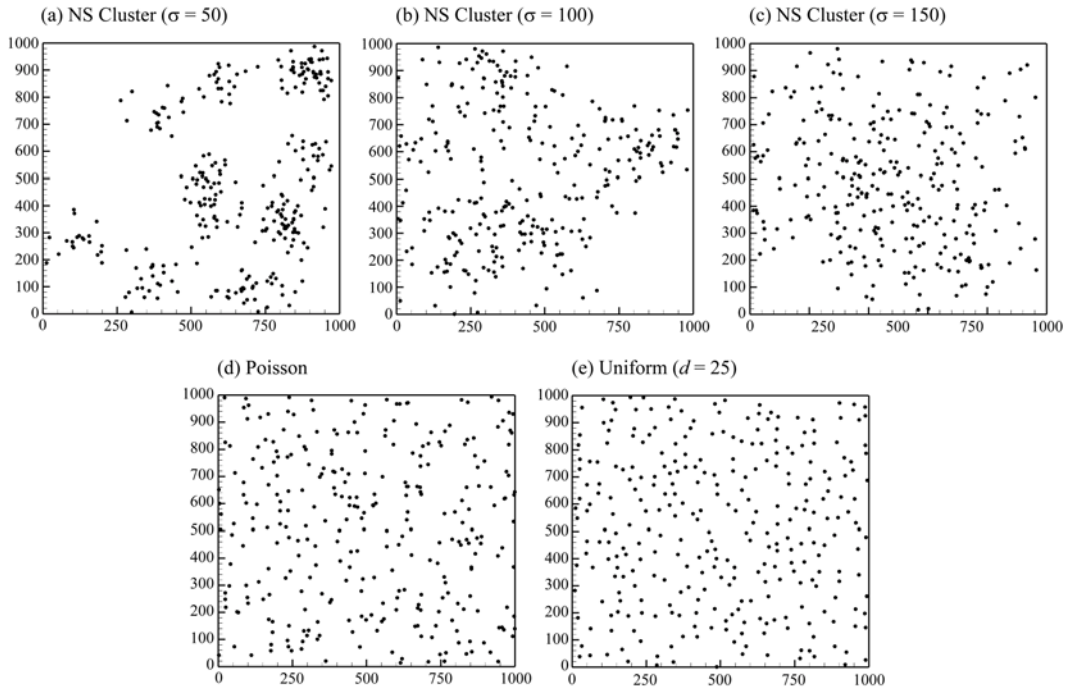

Figure 6.6 Examples of simulated point processes with 300 events: (a) Neyman-Scott (NS) cluster process with $\sigma = 50$; (b) NS with $\sigma = 100$; (c) NS with $\sigma = 150$; (d) Poisson (random); (e) Inhibition (uniform) $d = 25$. All point processes were simulated on a 1000 × 1000 square.

Table 6.2 Summary statistics of the simulated point processes

Events	Process	*Q*-ratio	% Threshold	CV_A
150	NS (μ = 10; σ = 50)	0.614 ± 0.025	34.911 ± 9.032	1.457 ± 0.288
	NS (μ = 10; σ = 100)	0.770 ± 0.060	29.001 ± 6.672	0.966 ± 0.194
	NS (μ = 10; σ = 150)	0.818 ± 0.047	21.200 ± 4.709	0.758 ± 0.082
	Poisson	0.988 ± 0.044	5.371 ± 1.194	0.548 ± 0.020
	Inhibition (*d* = 25)	1.127 ± 0.045	0.396 ± 0.137	0.533 ± 0.017
300	NS (μ = 20; σ = 50)	0.657 ± 0.026	38.010 ± 10.706	1.517 ± 0.218
	NS (μ = 20; σ = 100)	0.797 ± 0.022	29.199 ± 11.403	1.017 ± 0.208
	NS (μ = 20; σ = 150)	0.840 ± 0.020	22.479 ± 5.766	0.932 ± 0.081
	Poisson	1.025 ± 0.024	4.802 ± 1.129	0.611 ± 0.043
	Inhibition (*d* = 25)	1.285 ± 0.014	0.275 ± 0.088	0.410 ± 0.031
450	NS (μ = 30; σ = 50)	0.669 ± 0.020	40.567 ± 11.592	1.856 ± 0.248
	NS (μ = 30; σ = 100)	0.793 ± 0.034	28.926 ± 6.669	1.275 ± 0.245
	NS (μ = 30; σ = 150)	0.859 ± 0.018	18.378 ± 3.933	0.923 ± 0.124
	Poisson	0.992 ± 0.016	4.962 ± 1.103	0.597 ± 0.032
	Inhibition (*d* = 25)	1.334 ± 0.014	0.134 ± 0.098	0.338 ± 0.022

Values are presented as mean ± standard deviation. NS refers to Neyman – Scott clustering process..

The *Q*-ratios derived from the nearest neighbour statistics were observed to be robust discriminators of varying clustering levels and different point processes with various intensities. However, it should be noted that, the clustered patterns were generated by Poisson (Neyman - Scott) clustering process and different clustering levels correspond to alterations in the standard deviation of the Gaussian probability function that specifies the distance of clustered events from the parent event. Therefore, the mechanism of clustering in the synthetic data is closely related to the nearest neighbour distances, which may be reason for the success of nearest neighbour analysis in the present case. The graphical representations of the refined nearest neighbour analysis are demonstrated in Fig. 6.7.

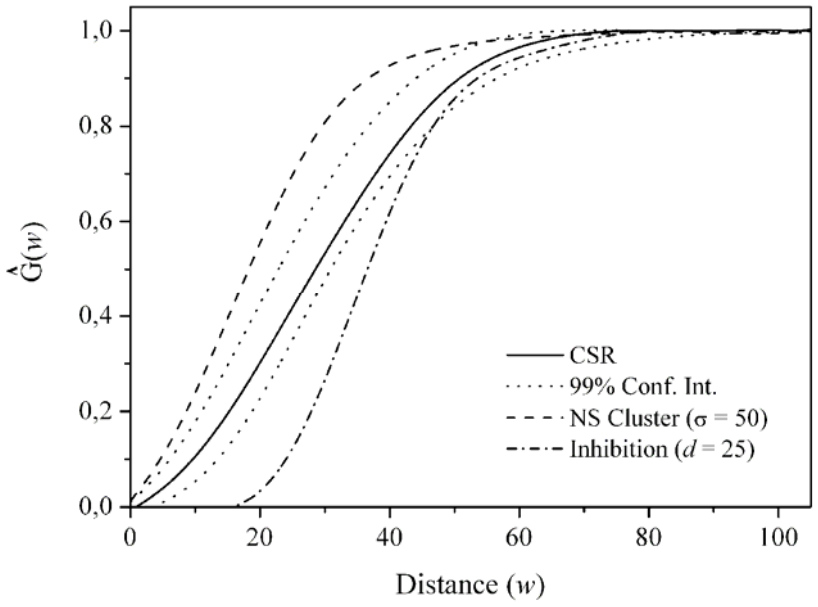

(a)

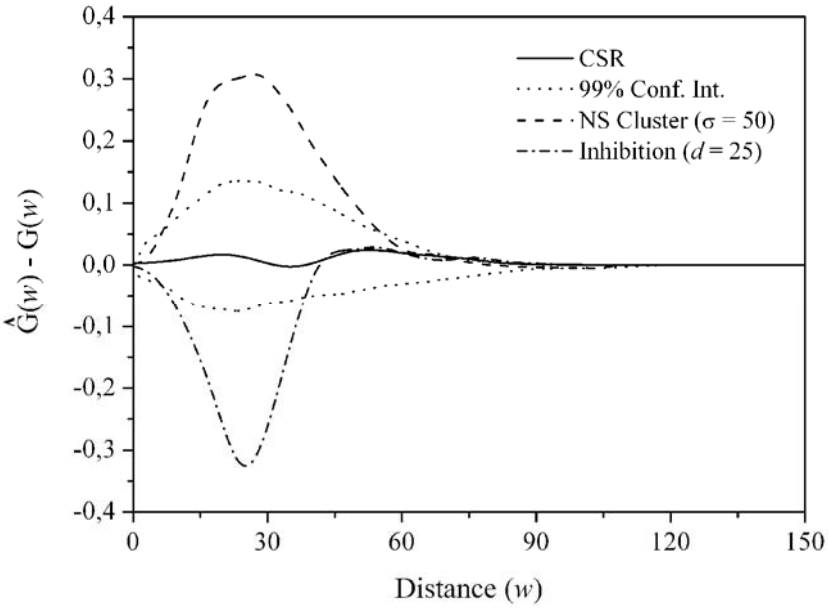

(b)

Figure 6.7 (a) The cumulative density function and (b) $\hat{G}(w) - G(w)$ plots of random (CSR), clustered (Neyman-Scott) and uniform (inhibition) point processes. Confidence intervals plotted at $\alpha = 0.01$ level, based on 200 replicates.

The generated point patterns were also analyzed by the local density statistics and the Voronoi tessellation method. % Threshold values in Table 6.2 were calculated from the ratio of average number of clustered events to the total number of events in each particular study region (Eqn. 2.7). The dispersions of the probability density functions for area (CV_A) distributions were also found to be sensitive to the different point patterns and to alternating cluster levels, which may again be due to same reason as discussed for the nearest neighbour method.

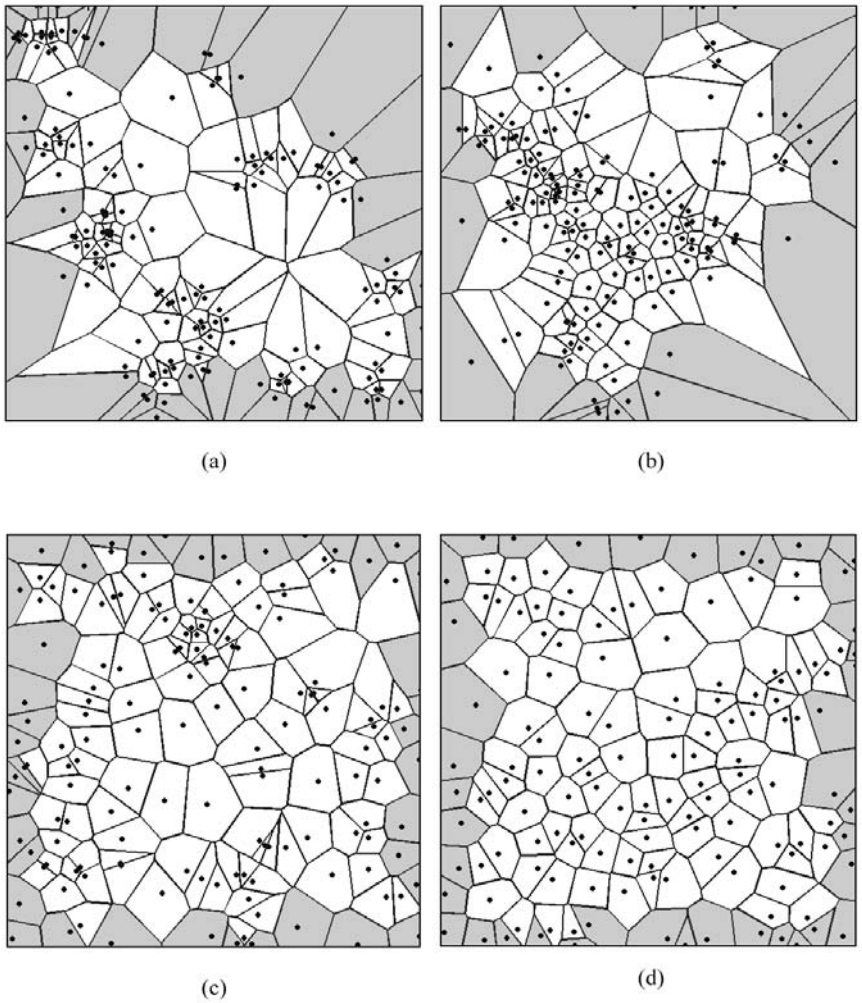

Figure 6.8 Sample Voronoi plots derived from generated point data: (a) Neyman Scott cluster process with $\sigma = 50$, (b) Neyman Scott cluster process with $\sigma = 100$, (c) Poisson (random) and (d) uniform distribution. Marginal polygons are shown in dark color and excluded from analysis since they are not statistically significant.

One drawback of the Voronoi tessellation method is the lack of information regarding the theoretical distribution functions for either Poisson or other known spatial processes. Consequently, the distinction between clustered and uniform distributions cannot be brought out by comparing the observed values with some theoretical statistics. Therefore, the results can only be evaluated in terms of the alterations in CV_A values. A lower CV_A value indicates uniform distribution, whereas higher values imply a tendency of cells to aggregate into clusters. Sample Voronoi plots derived from point data are presented in Fig. 6.8.

Fig. 6.9 presents the *K*-function plots of the generated data for clustered, random and uniform distributions. The advantage of *K*-function over the other methods discussed so far is that, it can characterize the pattern over many length scales. For example, the nearest neighbour statistics cannot identify the distinction between different patterns beyond a length scale of approximately 60 units (see Fig. 6.7). *K*-function, on the other hand, was observed to identify any deviation from randomness all throughout the analyzed length scales.

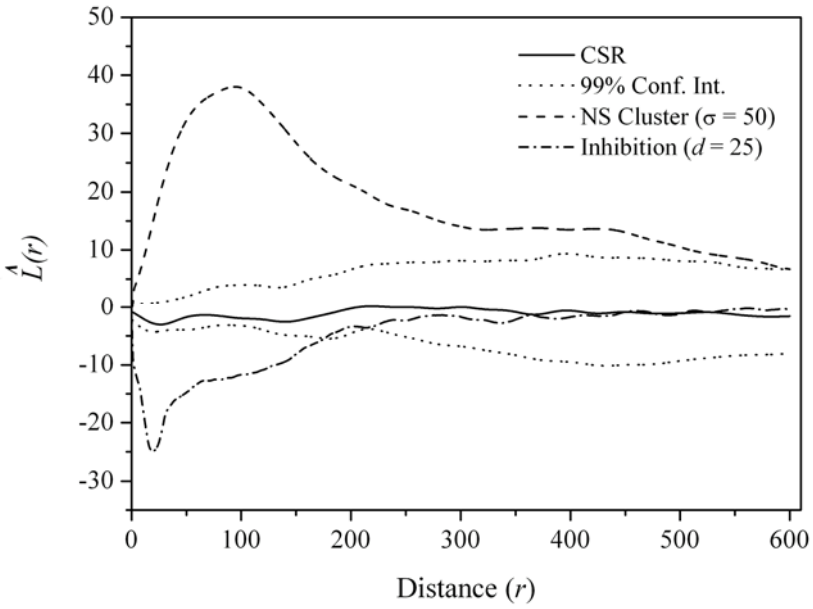

Figure 6.9 *K*-function plots presented with the $\hat{L}(r)$ correction for clustered, random and uniform distributions. Confidence intervals at $\alpha = 0.01$ level, based on 200 replicates.

The % Threshold values presented in Table 6.2 were obtained from the ratio of above-threshold events to all events within considered study regions averaged across all scales of observation. The decision whether an event belongs to a cluster or not depends on the number of events surrounding that particular event at some specific radius *r*. If the number of events surrounding an event exceeds the threshold $Th_{0.95}(r)$ at some distance *r*, that event was inferred to be a part of a cluster for that scale of observation. Therefore, the global clustering set *S(r)* was updated at each distance scale, meaning that the number of above-threshold events varies at each scale of observation. Fig. 6.10a presents this variation in percentages as a function of distance *r* for a generated clustered data set composed of 300 events with $\mu = 20$ and $\sigma = 100$ (see Fig 6.6b).

Three different distance scales were considered (80, 200 and 360) to monitor the effect of scale parameter *r* on localization of detected clusters. The kernels associated to the global cluster sets *S(r)* for each indicated distance scale are presented in Fig. 6.10b. Increasing the scale parameter from $r = 80$ to $r = 200$ expands the clusters, meaning that extra events were considered to be a part of a cluster. Further increasing the scale parameter from $r = 200$ to $r = 360$ results in rejection of some events from the global clustering set (the decrease in Fig. 6.10a). However, the kernels emerging from individual clusters merge into a single large cluster due to their interaction as a result of relatively large scale of observation as compared to the distance between the cluster centers. Note that while varying the scale parameter, the cluster centers remain approximately at the same positions.

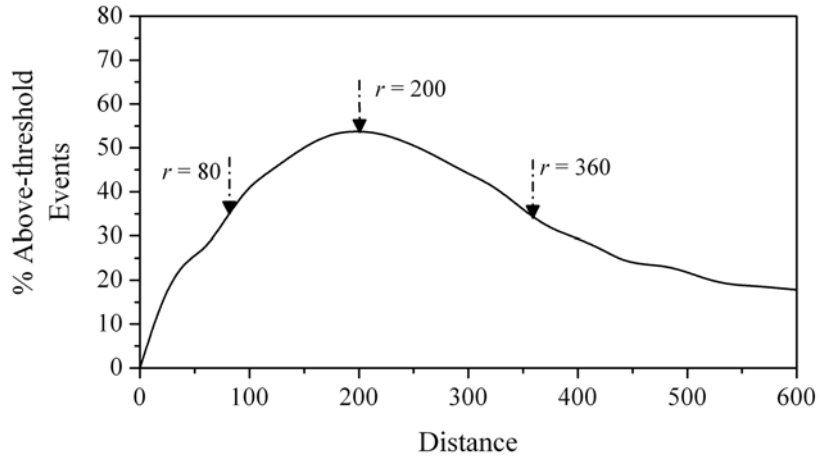

(a)

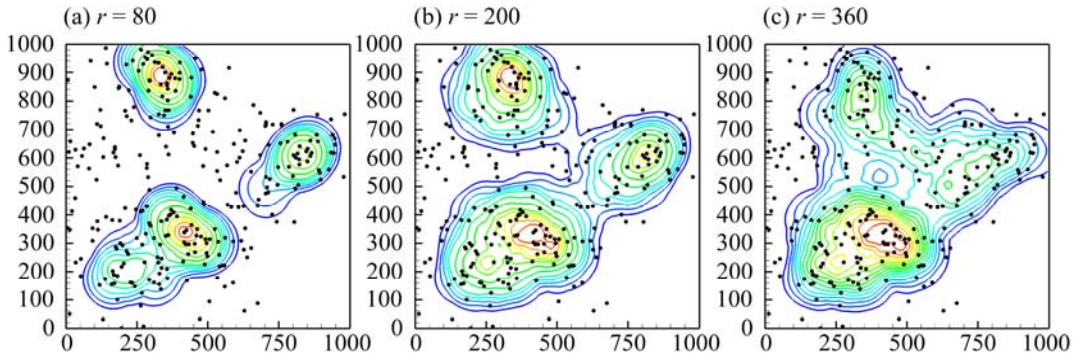

(b)

Figure 6.10 (a) Variation in amount of above-threshold events with scale of observation, (b) Kernel surfaces associated to above-threshold events.

According to Fig. 6.10a, clustering is most pronounced at a distance scale of r = 200 units. At this scale, the percentage of events that exceed the threshold reaches to a maximum. Therefore, this scale of observation can accepted to be the most informative scale regarding cluster geometries. Scales lower than r = 200 result in small individual clusters distributed as spikes over the matrix and higher scales result in formation of big merged clusters.

6.2.2 Quantitative Analysis of Composite Microstructures

6.2.2.1 Refined nearest neighbour analysis

The results of the nearest neighbour statistics indicate that, although the method is sensitive to various levels of clustering, it is not the best choice for quantitative analysis of particle distribution in metal matrix composites. The first reason is that, the method only considers the interaction of nearest particles and do not take the second, third or any other nearest particle into account. However, clusters in composites occur by involvement of many reinforcement particles and over many distance scales. The lack of information regarding the distribution of particles beyond the nearest neighbours makes this method a weak candidate in quantitative analysis of composite microstructures.

The refined nearest neighbour statistics can be presented by a variety of plots, which were demonstrated through Figs. 6.11 and 6.12. Fig. 6.11 shows the cumulative density function plots and the corresponding $\hat{G}(w) - G(w)$ variations. $\hat{G}(w) - G(w)$ plots simply express the difference between observed and theoretical (Poisson) distributions. Values below the confidence interval suggest uniform distribution, whereas values above the confidence interval indicate clustering of particles. Another way to present the nearest neighbour statistics is demonstrated through Figs. 6.12a, 6.12c and 6.12e. These plots present the nearest neighbour statistics of the observed pattern with reference to the Poisson distribution. Any deviation from linearity also indicates deviation from randomness. Similarly, values below the confidence interval suggest uniform distribution, whereas values above the confidence interval indicate clustering of particles.

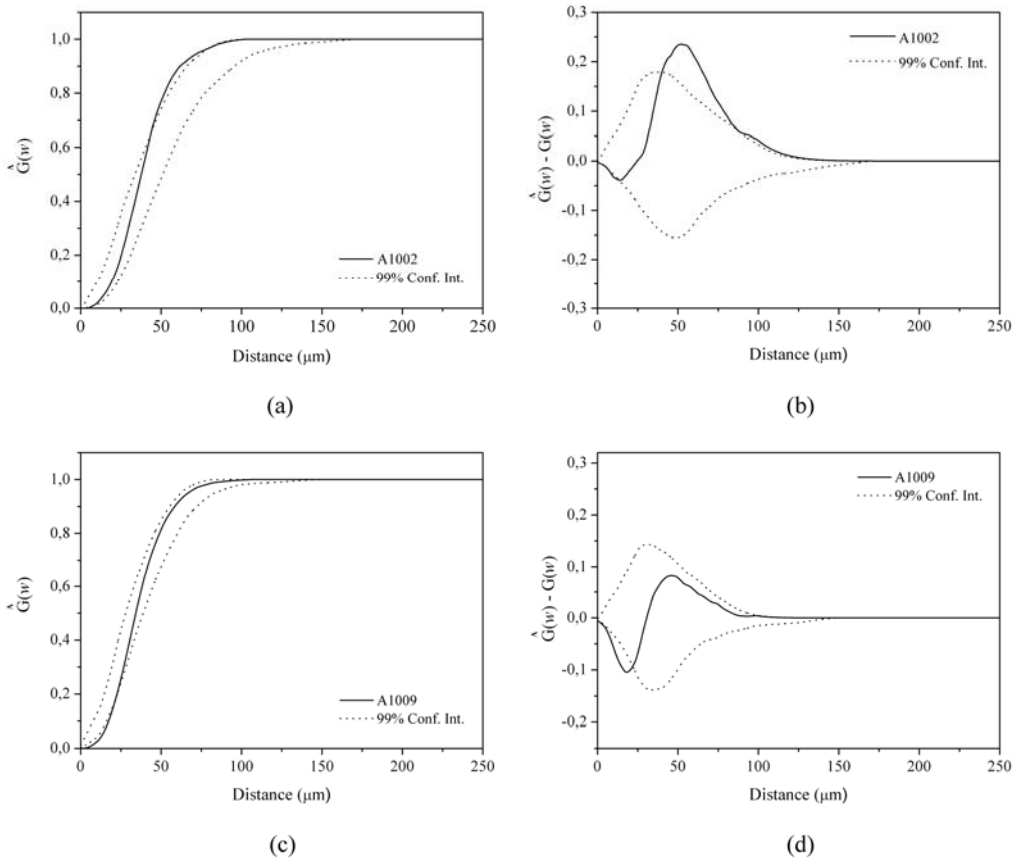

Figure 6.11 Sample cumulative density function plots (on the left hand side) and $\hat{G}(w) - G(w)$ plots (on the right hand side) for A356 alloy composites reinforced with 10% SiC_p for samples A1002 and A1009.

The refined nearest neighbour analysis was found to be effective in characterizing the global trends in distribution; however, cannot provide information about the local variations in the microstructure. The main issue in quantitative characterization of particle distribution is to relate the microstructure to the mechanical response of the composites. The nearest neighbour statistics fail to overcome this problem since the mechanical response is mainly determined by local variations in particle content and therefore cannot be described over a statistics that presents a summary that considers the interaction between closest particles.

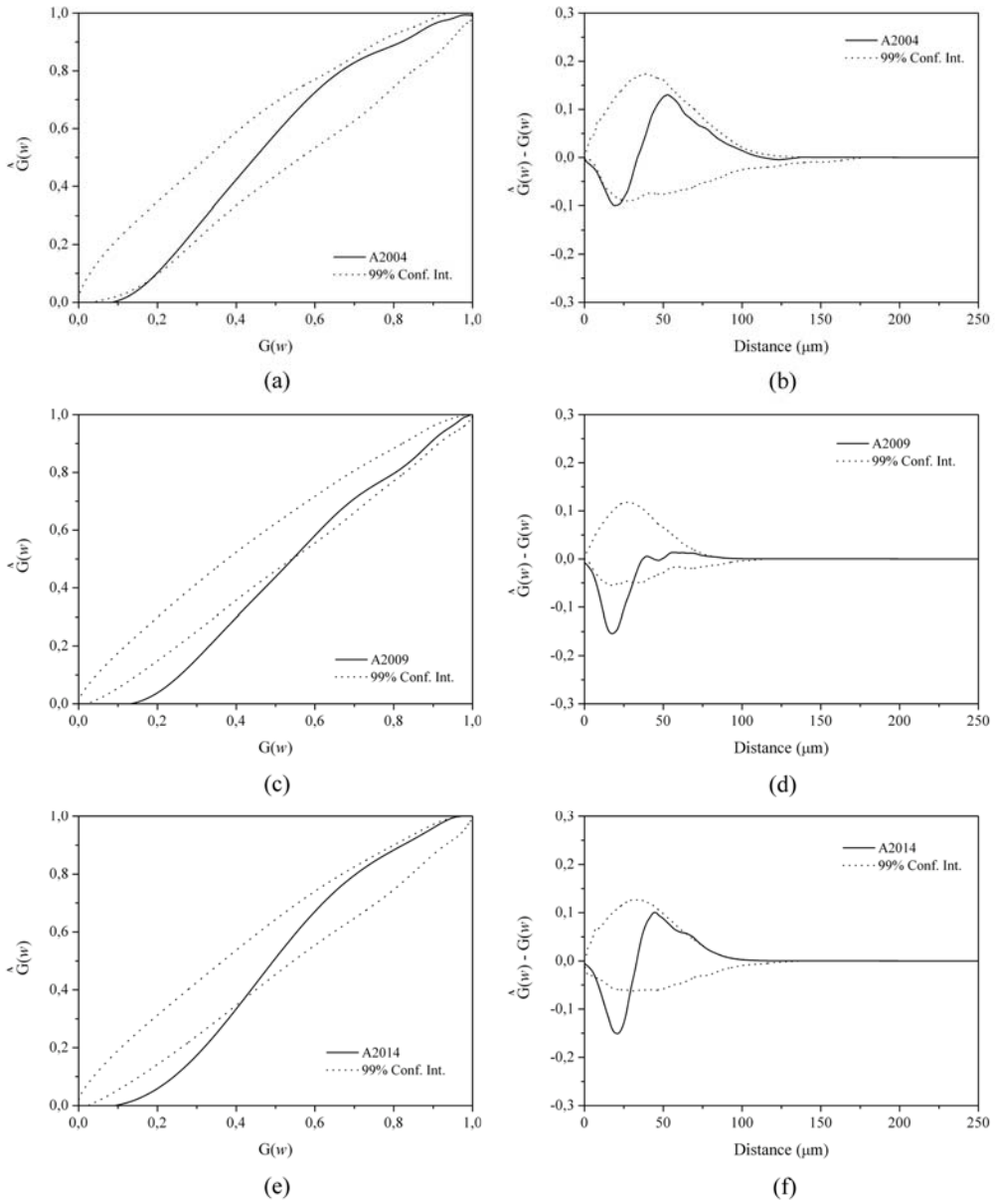

Figure 6.12 Sample refined nearest neighbour analysis results for A356 alloy composites reinforced with 20% SiC_p. for sample A2004, A2009 and A2014.

It is interesting to note that all plots indicate a solid tendency towards regularity at length scales up to approximately 30 μm. This value corresponds to the average SiC size used in the present study (29.2 ± 1.5 μm). Since the particles cannot approach each other closer than their diameter, the statistics suggest regularity within this length scale.

6.2.2.2 Voronoi tessellation

The Voronoi tessellation method considers the area distribution of the polygonal cells to assess the level of inhomogeneity. The results indicate that, although the method yields a good pictorial impression of the spatial pattern of the reinforcement particles, it cannot provide a comprehensive description of the microstructure. Sample tessellated composite microstructures are presented in Fig. 6.13.

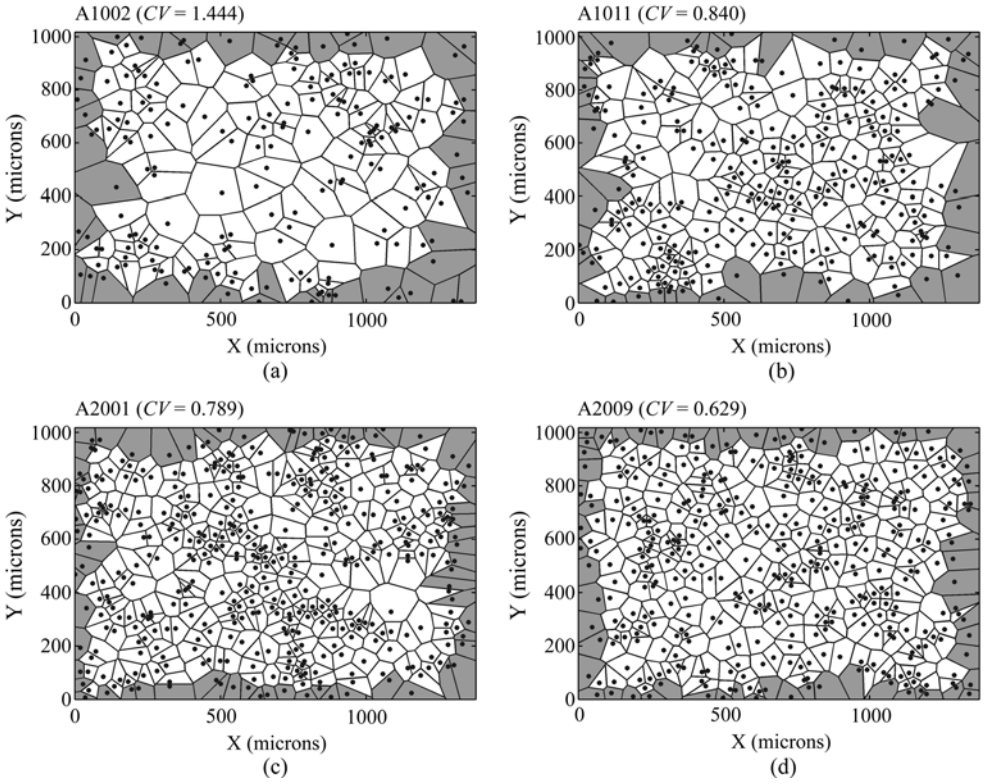

Figure 6.13 Sample Voronoi plots derived from composite microstructures together with the corresponding CV_A values for each particular micrograph. A higher CV_A value indicates tendency of cells to aggregate into clusters.

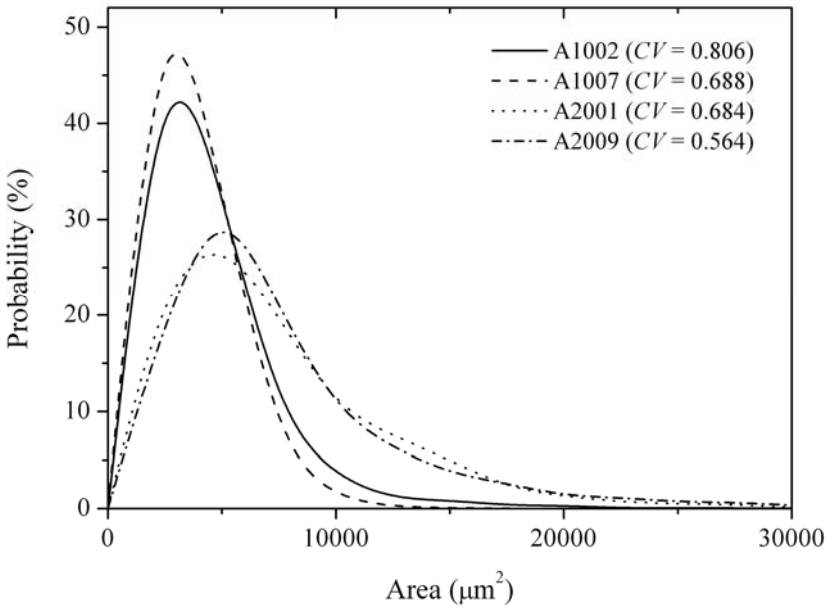

Figure 6.14 Sample probability density function plots for composites reinforced with 10% SiC and 20% SiC particles. A higher CV_A value indicates tendency of cells to aggregate into clusters.

The probability density functions of polygon area, *f(A)*, for some composite microstructures are plotted in Fig. 6.14. One problem associated with this approach is the sensitivity of the method to the volume fraction particles. At higher volume fraction (20% SiC), the distinction between levels of clustering is not as clear as in lower volume fraction of particles (10% SiC). Yet, this comparison is only valid for composites with similar volume fraction of particles. Normally, the intensity of the peaks ceases as the level of inhomogeneity increases. However, the reduction in the intensity of the peaks with increasing volume fraction occurs due to the decrease in area gradients as a result of high particle density and should not be interpreted as an increase in inhomogeneity.

The terms “inhomogeneity” and “clustering” are frequently used as synonyms with regard to distribution of second phase particles in metal matrix composites. However, the clusters in such materials cannot be directly detected by measuring the level of inhomogeneity by some statistical method. The Voronoi diagrams and their corresponding probability density function plots indicate that, the method is actually informative when one needs to assess the level of inhomogeneity of a given spatial pattern. However, in the

case of metal matrix composites, one also needs to gather information on the locations, relative intensities and spatial connectivities of the clusters. Description of whole microstructures in terms of some scalar numbers obviously cannot provide these information. Therefore, Voronoi tessellation was also not considered as a suitable method in quantitative characterization of metal matrix composites.

6.2.2.3 *K*-function

K-function (also known as Ripley's *K*-function) is a second order intensity function and is known as the most effective method for assessing departure from spatial randomness[75, 76]. Similar to radial distribution function, it is very sensitive to local variations and it has the ability to characterize a given morphological pattern over many length scales. The *K*-functions for some composite microstructures are plotted in Fig. 6.15.

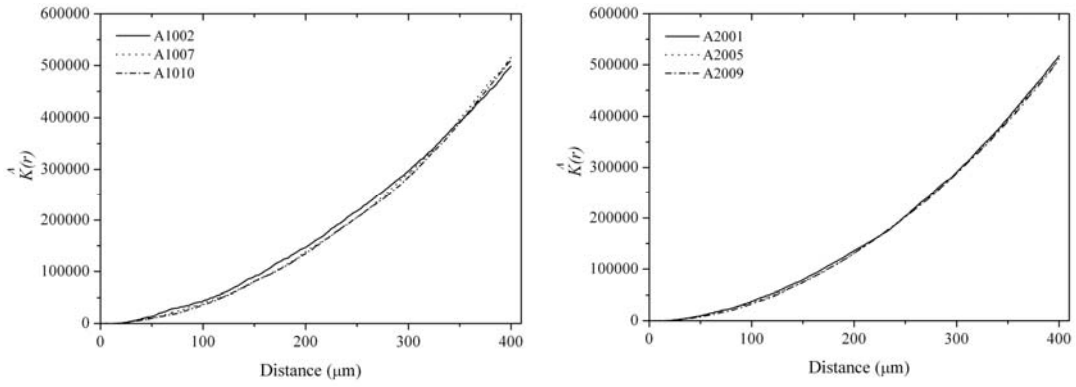

(a) (b)

Figure 6.15 Sample *K*-function plots for a number of composites reinforced with (a) 10% SiC and (b) 20% SiC particles.

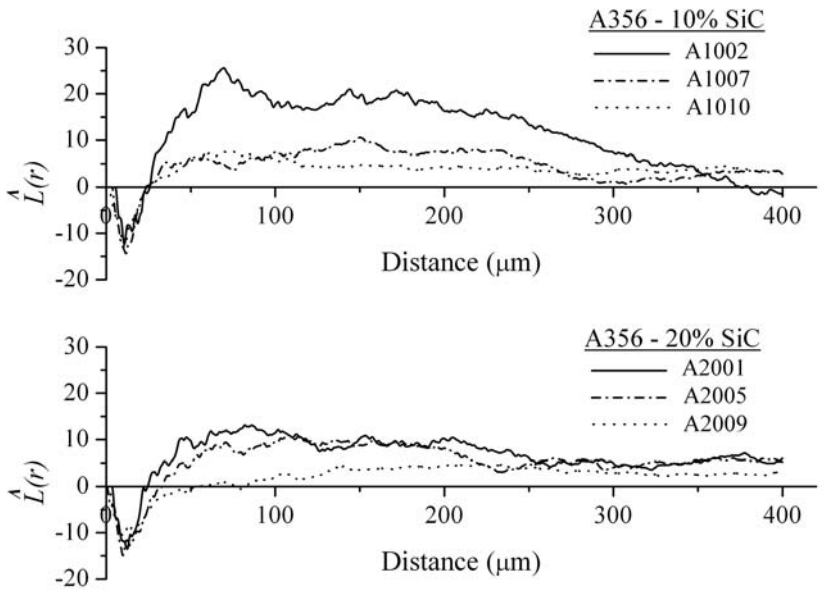

Figure 6.16 Sample $\hat{L}(r)$ function plots for composites reinforced with 10% and 20% SiC_p. The confidence intervals are not shown on the plots for simplicity, since each sample has different intensity resulting in different confidence limits.

Although *K*-function is quite sensitive to the trends in the pattern, it is commonly presented with a linearization transformation in order to bring out the differences between various patterns. Corresponding $\hat{L}(r)$ functions are plotted in Fig. 6.16. Instead of nearest neighbour statistics and the Voronoi tessellation, *K*-function is observed to detect any deviation from regularity over many length scales. The reinforcement particles aggregate into clusters at all distance scales greater than approximately 30 μm, which corresponds to the average SiC size used in the present study (29.2 ± 1.5 μm). The *K*-function results reveal that, clustering of reinforcement particles occur with arrangement of many particles over various distance scales. Therefore, the nature of these clusters can hardly be inferred by a statistics that only considers the interaction with the nearest neighbours. This is another limitation that indicates the deficiency of nearest neighbour statistics and Voronoi tessellation to be employed in quantitative characterization of composite microstructures.

6.2.2.4 Local density statistics

As mentioned previously, although the *K*-function successfully measures the local density around each particle, presence of clustering can be inferred only when the local density around a particle exceeds a certain threshold value. These threshold values were obtained from a threshold function, $T_{0.95}(r)$, which expresses the probability that the local density around a particle, as depicted by $\rho(P_i, r)$, exceeds a certain value in an associated Poisson point process. Figs. 6.17 through 6.24 show sample microstructural patterns, together with the variation of above-threshold particles as a function of observation scale.

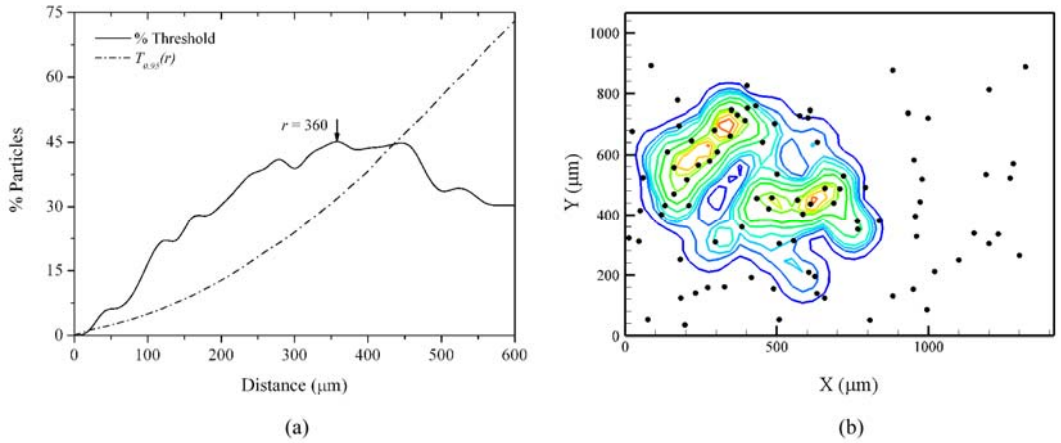

Figure 6.17 Evaluation of a micrograph from sample A1001: (a) Effect of observation scale on the amount of above-threshold particles and (b) clusters demonstrated by kernel surfaces at the observation scale where clustering is most pronounced (r = 360 μm).

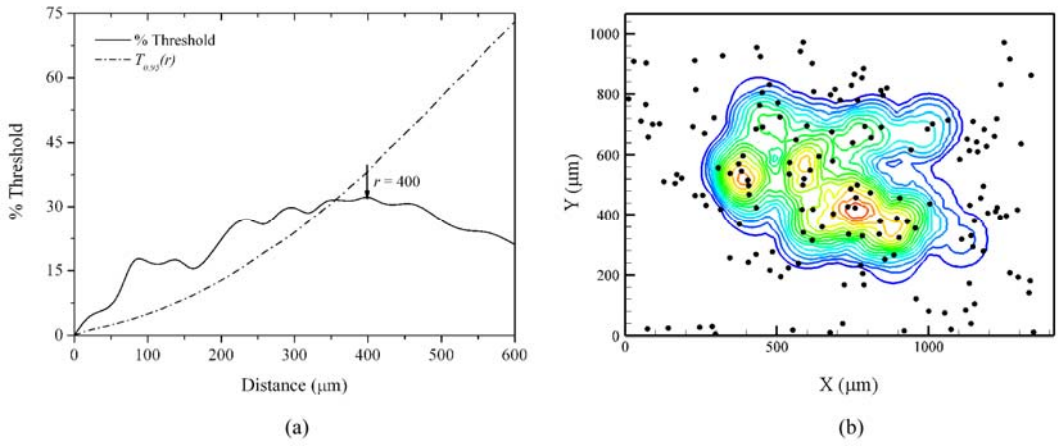

Figure 6.18 Evaluation of a micrograph from sample A1002: (a) Effect of observation scale on the amount of above-threshold particles and (b) clusters demonstrated by kernel surfaces at the observation scale where clustering is most pronounced (r = 400 μm).

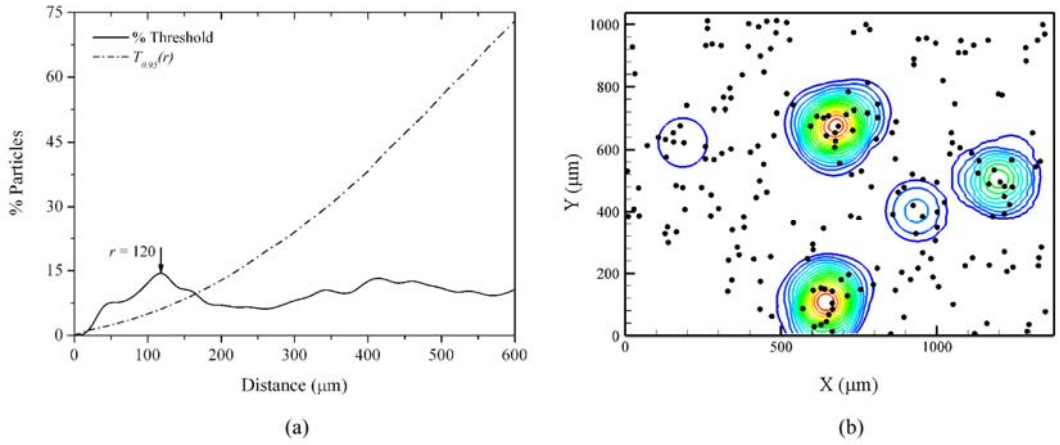

Figure 6.19 Evaluation of a micrograph from sample A1008: (a) Effect of observation scale on the amount of above-threshold particles and (b) clusters demonstrated by kernel surfaces at the observation scale where clustering is most pronounced (r = 120 μm).

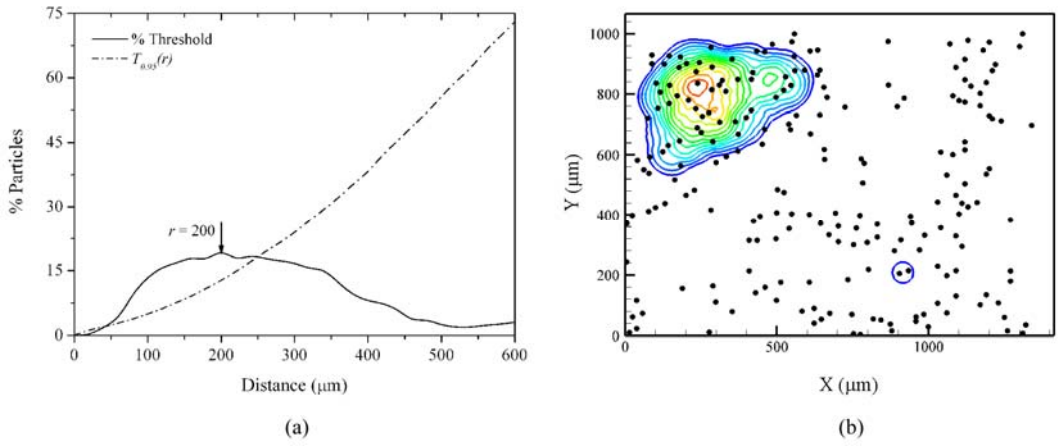

Figure 6.20 Evaluation of a micrograph from sample A1009: (a) Effect of observation scale on the amount of above-threshold particles and (b) clusters demonstrated by kernel surfaces at the observation scale where clustering is most pronounced (r = 200 μm).

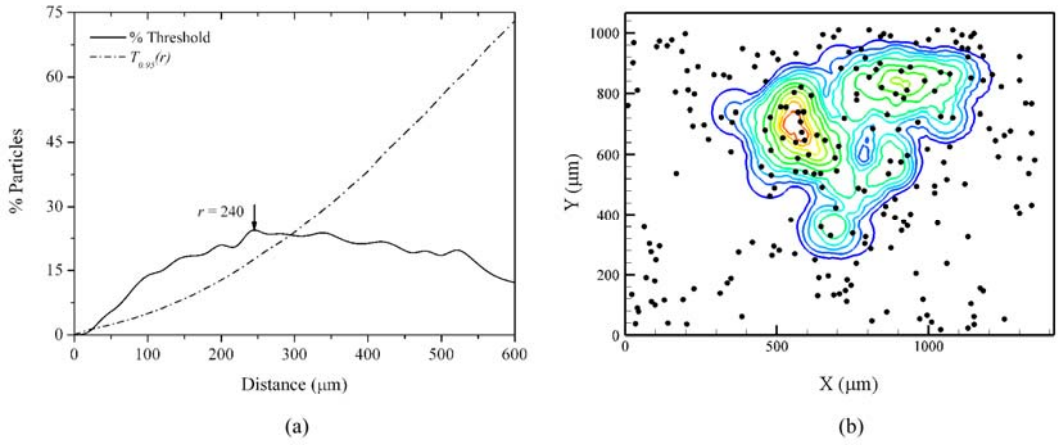

Figure 6.21 Evaluation of a micrograph from sample A2001: (a) Effect of observation scale on the amount of above-threshold particles and (b) clusters demonstrated by kernel surfaces at the observation scale where clustering is most pronounced (r = 240 μm).

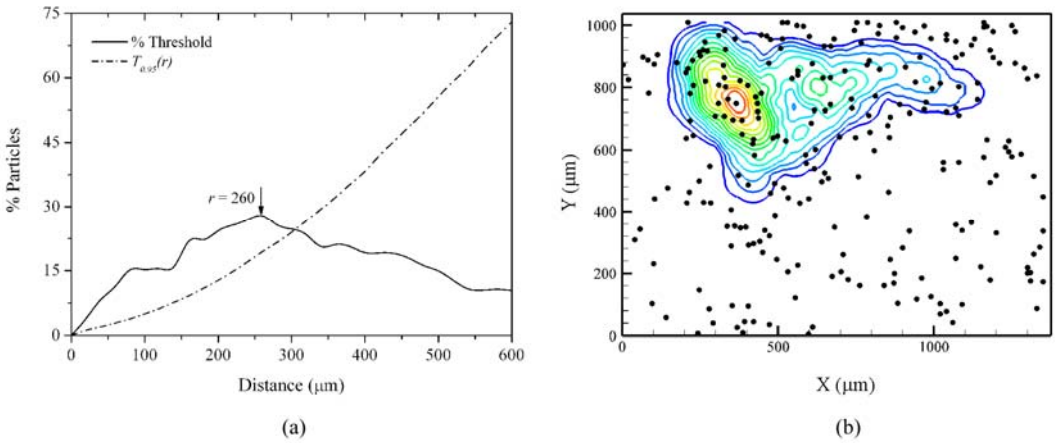

Figure 6.22 Evaluation of a micrograph from sample A2001: (a) Effect of observation scale on the amount of above-threshold particles and (b) clusters demonstrated by kernel surfaces at the observation scale where clustering is most pronounced (r = 260 μm).

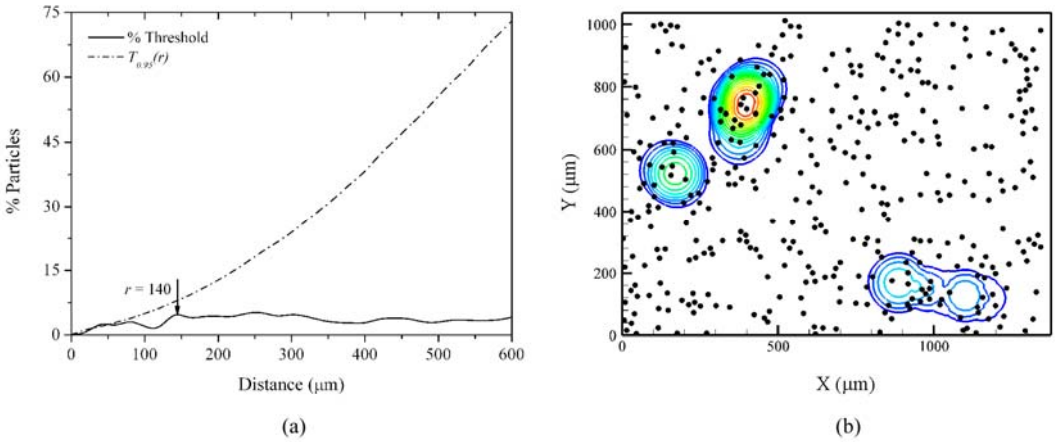

Figure 6.23 Evaluation of a micrograph from sample A2009: (a) Effect of observation scale on the amount of above-threshold particles and (b) clusters demonstrated by kernel surfaces at the observation scale where clustering is most pronounced (r = 140 μm).

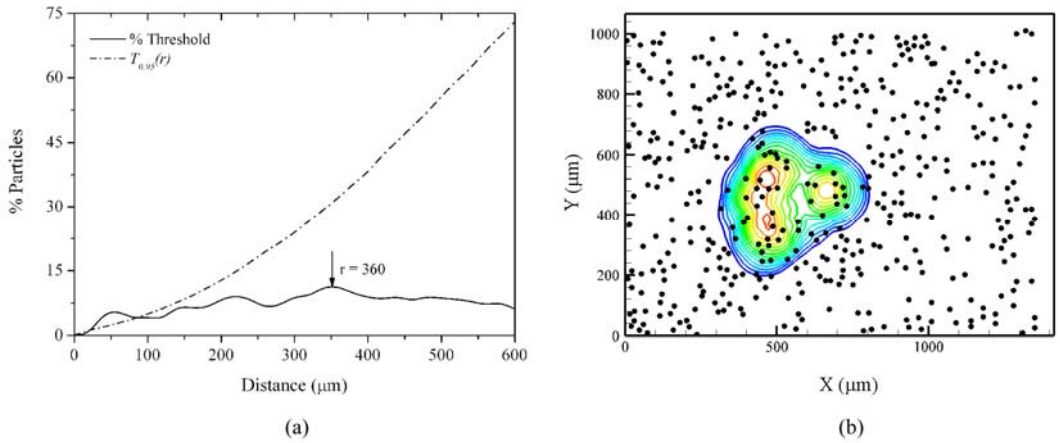

Figure 6.24 Evaluation of a micrograph from sample A2009: (a) Effect of observation scale on the amount of above-threshold particles and (b) clusters demonstrated by kernel surfaces at the observation scale where clustering is most pronounced (r = 360 μm).

As described previously, the local density around a particle may or may not exceed the corresponding clustering threshold depending on the scale of observation, r. The subfigures (a) in Figs. 6.17 through 6.24 show the influence of scale on the amount of above-threshold particles for actual composite microstructures. From these plots, the amount of deviation from randomness can be quantified over many length scales in terms of the amount of particles that have higher local density as compared to an associated Poisson process with the same intensity. The intensity of the peaks in these plots indicates the amount of particles that exceeds the clustering threshold.

The detected clusters are demonstrated by kernel surfaces in subfigures (b) in Figs. 6.17 through 6.24 at observation scales where clustering is most pronounced. It is interesting to note that, samples solidified with relatively slow and fast cooling rates display large clusters with arrangement of many above-threshold particles. The samples solidified with relatively moderate cooling rates, on the other hand, display small clusters, randomly distributed throughout the matrix. This result was verified to hold for all samples produced in this study and will be discussed in detail in section 6.3.2. No information regarding the cluster dimensions could be inferred from previously described statistical functions. Demonstration of the intensity variation of all particles also cannot help to obtain a clear picture about the cluster dimensions. One such example is illustrated

in Fig. 6.25, which compares the visual effectiveness of the local density statistics with the intensity variation of all particles, as demonstrated by kernel surfaces. The kernel surfaces, when associated with all particles, display similar trends with the intensity variation of the above-threshold particles in the clustered regions. However, these plots cannot provide information on the scales of clustered regions. The kernel surfaces associated with above-threshold particles, on the other hand, provide a much better description of the clustered regions by avoiding the particles, which do not agglomerate into clusters.

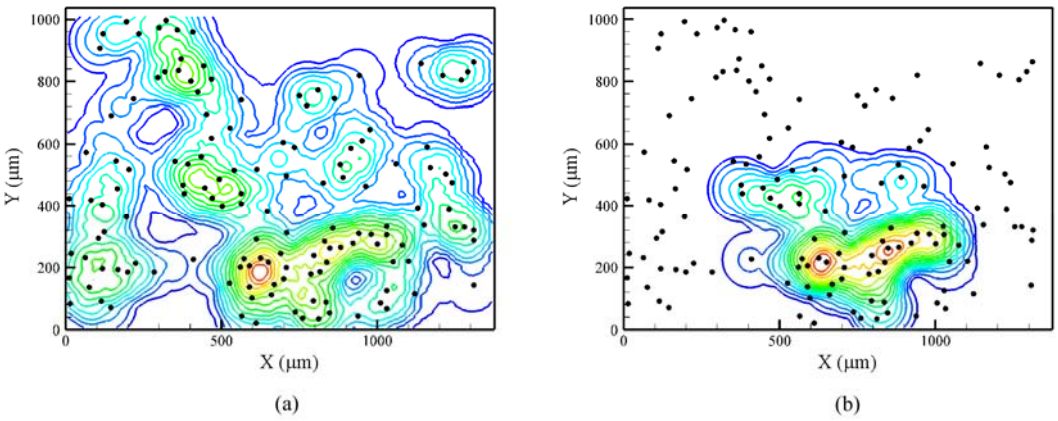

Figure 6.25 Kernel surfaces demonstrating the intensity variation of (a) all particles and (b) above-threshold particles.

The main aim of quantitative characterization of particle distribution is to relate the microstructure to the mechanical response of the composite materials. The results reveal that methods such as the nearest neighbour statistics or Voronoi tessellation have limited use in these systems since the mechanical response of the composites is determined by local variations in particle content and therefore cannot be described over a statistics that presents a summary of the interaction between nearest particles. The presented methodology, on the other hand, describes the pattern from the perspective of individual particles and even in a microstructure that globally conforms to random distribution, local clusters, which may actually control the mechanical response can be detected.

One problem, however, associated with this method is that not every particle that belongs to a cluster is included in the set of above-threshold particles, $S(r)$. As an example, let us consider an individual cluster composed of many SiC particles and surrounded by matrix only. Although the local density around the particles in the cluster core will exceed the clustering threshold, some particles close to cluster surface may not be accepted to $S(r)$ since the local density around these particles may be lower than the threshold. This limitation will especially be more pronounced as the particles form compact and well-separated clusters. In such cases, although the cluster locations can still be determined precisely, the amount of above-threshold particles may not reflect the actual amount of clustered particles. However, since the clusters in discontinuously reinforced composites are in the form of local variations in particle content rather than compact, well-separated agglomerates, the extent of this problem will not be realized significantly.

6.2.2.5 Effect of metallographic field size on cluster dimensions

The results of the local density statistics show that clusters in metal matrix composites can successfully be detected and visualized by the described approach. However, in all attempts the metallographic field size was constant (1376 × 1017 μm). We have also investigated the effect of metallographic field size on the size of the detected clusters. In order to capture the long range spatial patterns with high resolution we have performed the calculations on digital montages of contiguous microstructural fields (see Fig. 5.6).

Fig.6.26 shows the corresponding results of the local density statistics. A comparison from Fig. 6.26a between the samples reinforced with 10% and 20% SiC particles indicates that the sample reinforced with 10% SiC has higher level of clustering at all studied length scales, including the scale at which clustering is most pronounced.

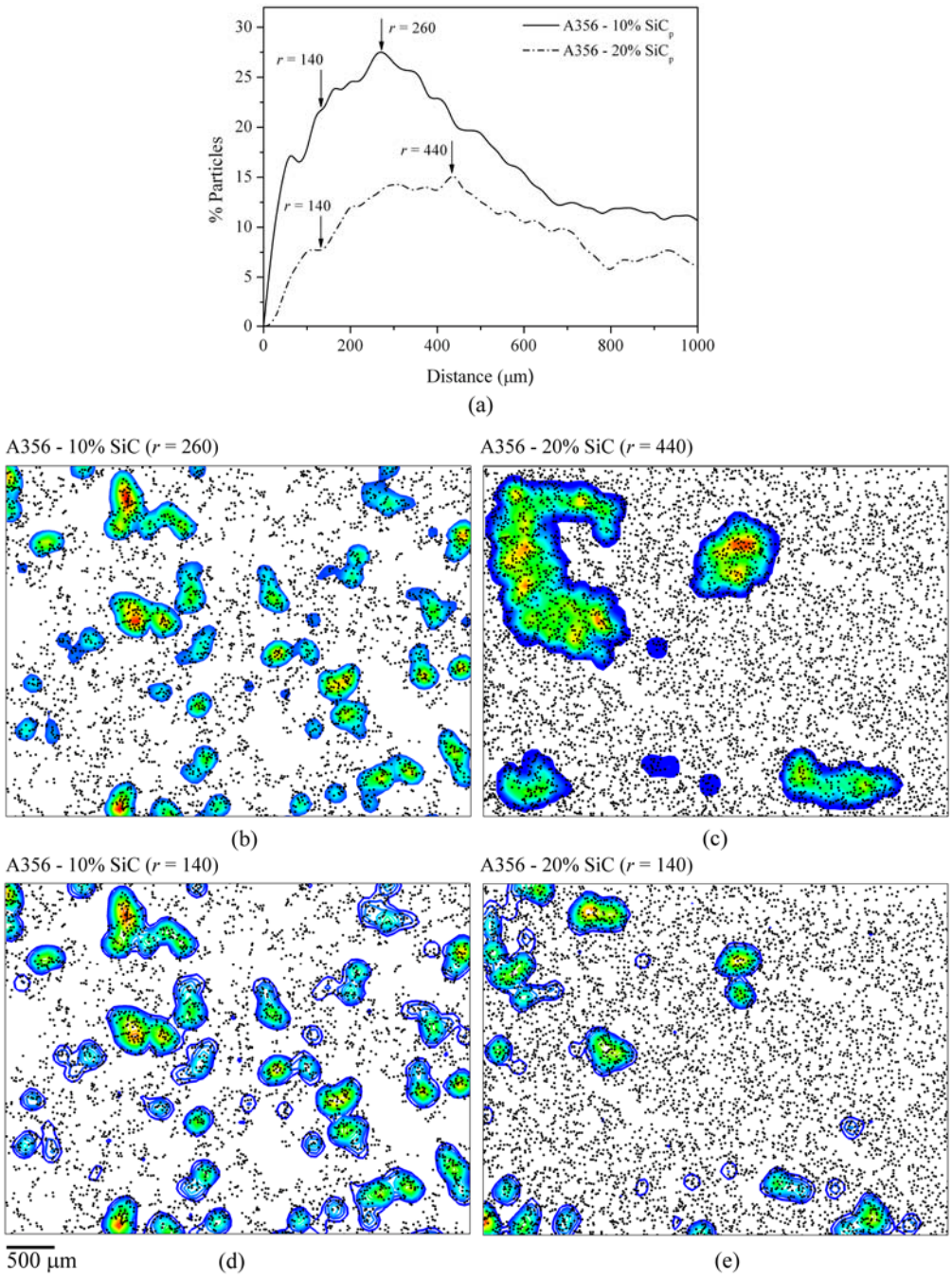

Figure 6.26 (a) Variation in the amount of above-threshold particles with scale of observation; (b-c) kernel surfaces associated to the set of above-threshold particles at scales where clustering is most pronounced and; (d-e) at an observation scale of 140 μm for composites reinforced with 10% and 20% SiC_p.

Figs. 6.26b-e shows the kernel surfaces associated to the set of above-threshold particles at scales where clustering is most pronounced to analyze the influence of scale on cluster locations. While varying the scale of observation from r = 260 μm to r = 140 μm, the cluster locations do not vary significantly in the sample with 10% SiC since the differences in length scales and amount of above-threshold particles at these scales are relatively small. In the sample with 20% SiC, on the other hand, although the locations where the clusters are detected remain almost the same, there is significant difference in the dimensions of the detected clusters. This is due to the fact that when the calculations are performed at a length scale of r = 140 μm, the nature of the pattern beyond 140 μm cannot be seen and therefore remains unevaluated. Consequently, the analysis results in small individual clusters distributed throughout the matrix, which do not seem to represent the actual cluster dimensions since no information is available beyond 140 μm. Upon increasing the length scale to r = 440 μm, some particles are rejected from $S(r)$ and some small clusters disappear since the local density around these particles does not exceed the clustering threshold anymore. However, a larger number of them are found to exceed the clustering threshold (the increasing trend in Fig. 6.26a). At this larger scale, the kernels merge to form bigger clusters, which can be accepted to represent a more accurate picture, since the number of particles that exceed the threshold reach to a maximum at this scale. Further increasing the length scales result in a decrease in the amount of above-threshold particles and the difference of the patterns from random distribution start to diminish.

It is interesting to note that, although there are considerable differences in cluster dimensions, the scales where clustering is most pronounced do not vary with metallographic field size. In all attempts, regardless of the metallographic field size, clustering was most pronounced at scales ranging between 150 – 500 μm. Therefore, in order to quantify the scale of clustering, one can make calculations on relatively small metallographic fields and end up with correct results. However, in order to reveal the actual dimensions of clusters, it is always better to work on micrographs that represent larger metallographic fields.

6.2.2.6 Comparison of methods

The refined nearest neighbour analysis and Voronoi tessellation were found to be effective in characterizing the global trends in distribution; however, cannot provide information about the local variations in the microstructure. The main issue in quantitative characterization of metal matrix composites is to relate the microstructure to the mechanical response of the composites. The nearest neighbour statistics and Voronoi tessellation fail to overcome this problem since the mechanical response is mainly determined by local variations in particle content and therefore cannot be described over a statistics that presents a summary that considers the interaction between closest particles. *K*-function was observed to be very sensitive to local variations in particle content and can effectively characterize the pattern over many distance scales. However, this method also fails to provide visual information on locations and dimensions of the clusters.

The local density statistics was observed to provide a much better description of the spatial pattern over many distance scales. Plots that show the variation of above-threshold particles with observation scale reveal that, the actual nature of clusters can hardly be inferred from the distances between nearest particles since clustering is evidenced over much larger scales of observation compared to nearest neighbour distances. The presented method considers the distribution from the perspective of individual particles, so that even in a pattern that globally conforms to random distribution, local clusters, which may actually control the mechanical response, can be detected. Results show that the presented methodology is an effective discriminator of clustered particles and can successfully be used for quantitative characterization of particle distribution.

6.3 Effect of Solidification Rate on Clustering of SiC Particles

6.3.1 Effect of Solidification Rate on Dendritic Structure

Distribution of SiC particles was evaluated in terms of two parameters related to primary solidification of composites; secondary dendrite arm spacing (SDAS) and volume fraction of solid phase at dendrite coherency point (f_S^{DCP}). We have examined the influence of solidification rate on these parameters for A356 alloy composites reinforced with 10% and 20% SiC_p. The influence of different SiC_p contents on SDAS was negligible, in agreement with the previous results reported in literature[1, 59]. Power law fits to the experimental data for composites with 10% and 20% SiC_p contents yield;

A356-10% SiC_p: $\lambda_2 = 37.2 \cdot \dot{T}^{-0.52}$ ($R^2 = 0.954$) (6.1)

A356-20% SiC_p: $\lambda_2 = 38.1 \cdot \dot{T}^{-0.56}$ ($R^2 = 0.949$) (6.2)

where, λ_2 is SDAS in μm and $\dot{T}$ is cooling rate in °C sec^{-1}. There exists a discrepancy regarding the cooling rate dependence of coherency point in the literature. Arnberg *et al*[42] reported a decrease in f_S^{DCP} with increasing cooling rate. Veldman *et al*[44] on the other hand, concluded from their research that an alteration to cooling rate alone has a negligible effect on f_S^{DCP}. In the present study, no relationships could be established between the solidification rate and the calculated coherencies. Although the coherency predictions obtained by NTA were observed to be in a slowly decreasing trend, FTA results were randomly scattered within the range of investigated solidification rates. As far as the effect of particle content is concerned, FTA results seem to yield a more accurate picture since, contrary to NTA, the f_S^{DCP} values obtained by FTA decrease as the particle content is increased from 10% to 20%.This is actually expected since the thermal conductivity of SiC[77] is much higher than that of A356 alloy[78] at the temperature range of coherency. Therefore, the SiC particles between growing dendrite arms contribute to the established fast channel of heat transfer and manipulate the coherency values, resulting in early predictions in general.

6.3.2 Effect of Solidification Rate on Particle Distribution

It was observed that the relationship of particle distribution to solidification rate can be characterized by three intervals for both reinforcement contents, which were denoted as intervals *1*, *2* and *3* in Tables 6.3 and 6.4 and Figs. 6.27 and 6.28. First interval was characterized by a continuous decrease in SDAS with increasing solidification rate. Both statistical functions suggested a decrease in amount of clustering with increasing solidification rate in this interval for both reinforcement contents. The f_S^{DCP} values were observed to be almost independent of solidification rate. In the second interval, further increasing the cooling rate did not create significant alterations in SDAS and the spacings remained almost constant around 40 μm. Interestingly, the corresponding statistics also did not suggest any significant tendency in this range. The f_S^{DCP} values were still fluctuating, however at relatively lower values as compared to the first interval. In the third interval SDAS values were smaller than the average particle size (29.2 ± 1.5 μm). In contrary to first two intervals, the statistical functions suggest tendency towards clustering. The f_S^{DCP} values exhibited sharp alterations, maintaining its scattered nature.

The tabulated results of statistical functions indicate that distribution of SiC particles is mainly determined by secondary dendrite arm spacings. This dependence is characterized by two steps in the first two intervals: (i) the growing secondary dendrite arms push the SiC particles into interdendritic regions, where the particles start to agglomerate; (ii) during growth of dendrite arms, there also occurs a fluid flow through these arms to feed the solidification shrinkage[79]. This flow carries some particles from interdendritic spaces towards the roots of secondary arms, therefore preventing formation of larger clusters.

Table 6.3 Effect of solidification rate (SR) on SDAS, f_S^{DCP} and corresponding summary statistics for A356 composites reinforced with 10% SiC_p

Interval	Sample	SR (°C sec^{-1})	SDAS (μm)	f_S^{DCP} (NTA)	f_S^{DCP} (FTA)	% Threshold	*Q*-ratio	CV_A
1 – 10% SiC_p	A1001	0.164	86.99 ± 12.51	0.271	0.203	17.781 ± 6.183	0.809 ± 0.067	0.827 ± 0.111
	A1002	0.242	72.70 ± 11.32	0.278	0.207	18.320 ± 7.949	0.815 ± 0.035	0.806 ± 0.103
	A1003	0.280	70.21 ± 11.45	0.273	0.174	18.539 ± 7.628	0.817 ± 0.063	0.839 ± 0.161
	A1004	0.345	72.23 ± 9.30	0.227	0.138	15.161 ± 6.427	0.853 ± 0.022	0.731 ± 0.242
	A1005	0.411	62.14 ± 8.69	0.270	0.212	16.021 ± 6.877	0.862 ± 0.028	0.749 ± 0.073
	A1006	0.429	60.58 ± 9.83	0.233	0.218	15.778 ± 7.496	0.858 ± 0.053	0.747 ± 0.097
2 – 10% SiC_p	A1007	0.596	42.44 ± 4.67	0.244	0.146	11.184 ± 6.764	0.892 ± 0.063	0.688 ± 0.078
	A1008	0.682	43.10 ± 7.42	0.238	0.141	11.925 ± 5.631	0.876 ± 0.067	0.808 ± 0.182
	A1009	0.725	48.20 ± 5.35	0.204	0.136	12.234 ± 3.447	0.881 ± 0.044	0.656 ± 0.101
	A1010	0.795	41.12 ± 6.12	0.209	0.195	12.285 ± 4.339	0.886 ± 0.035	0.682 ± 0.049
	A1011	0.981	37.40 ± 3.17	0.229	0.231	11.121 ± 3.842	0.878 ± 0.029	0.661 ± 0.071
	A1012	1.121	40.10 ± 2.95	0.196	0.147	12.282 ± 4.399	0.912 ± 0.016	0.692 ± 0.117
	A1013	1.329	35.12 ± 2.21	0.166	0.197	11.287 ± 3.371	0.891 ± 0.021	0.667 ± 0.058
3 – 10% SiC_p	A1014	1.928	24.89 ± 2.42	0.171	0.231	14.882 ± 4.011	0.852 ± 0.049	0.726 ± 0.088
	A1015	2.319	21.36 ± 2.78	0.129	0.204	15.687 ± 4.971	0.861 ± 0.031	0.731 ± 0.078

SDAS and statistical results are presented as mean ± standard deviation

Table 6.4 Effect of solidification rate (SR) on SDAS, f_S^{DCP} and corresponding summary statistics for A356 composites reinforced with 20% SiC_p

Interval	Sample	SR (°C sec^{-1})	SDAS (μm)	f_S^{DCP} (NTA)	f_S^{DCP} (FTA)	% Threshold	*Q*-ratio	CV_A
1 – 20% SiC_p	A2001	0.213	83.03 ± 6.32	0.268	0.117	13.952 ± 3.667	0.931 ± 0.019	0.684 ± 0.071
	A2002	0.309	76.68 ± 5.85	0.288	0.130	12.647 ± 7.241	0.952 ± 0.048	0.657 ± 0.048
	A2003	0.353	69.57 ± 5.92	0.291	0.107	10.130 ± 2.526	0.969 ± 0.051	0.688 ± 0.063
	A2004	0.429	65.23 ± 7.21	0.252	0.168	11.329 ± 5.365	0.963 ± 0.043	0.624 ± 0.064
	A2005	0.566	54.40 ± 7.03	0.252	0.154	10.801 ± 4.221	0.957 ± 0.073	0.672 ± 0.051
2 – 20% SiC_p	A2006	0.652	42.83 ± 7.12	0.256	0.122	8.932 ± 3.541	0.994 ± 0.011	0.617 ± 0.054
	A2007	0.698	40.60 ± 5.19	0.231	0.164	8.719 ± 4.050	0.986 ± 0.023	0.617 ± 0.054
	A2008	0.775	42.41 ± 3.57	0.198	0.136	7.868 ± 3.999	1.036 ± 0.029	0.619 ± 0.084
	A2009	0.806	47.09 ± 4.11	0.239	0.169	7.058 ± 3.785	1.035 ± 0.032	0.564 ± 0.034
	A2010	1.107	38.22 ± 3.12	0.207	0.162	7.125 ± 2.593	1.015 ± 0.020	0.605 ± 0.059
	A2011	1.211	40.07 ± 2.89	0.194	0.188	7.311 ± 3.253	1.024 ± 0.025	0.568 ± 0.047
	A2012	1.421	33.58 ± 2.66	0.156	0.221	5.205 ± 3.386	1.016 ± 0.017	0.597 ± 0.056
3 – 20% SiC_p	A2013	1.861	25.78 ± 2.91	0.186	0.176	8.883 ± 3.971	0.966 ± 0.028	0.627 ± 0.048
	A2014	2.417	20.52 ± 2.31	0.109	0.191	10.673 ± 2.584	0.973 ± 0.021	0.641 ± 0.052

SDAS and statistical results are presented as mean ± standard deviation

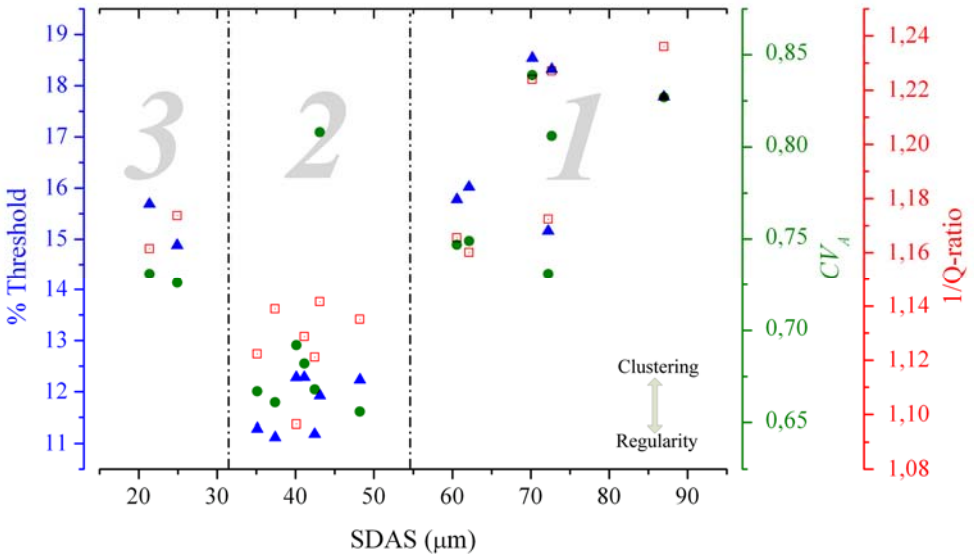

Figure 6.27 Effect of SDAS on clustering of reinforcement particles in A356 alloy composites reinforced with 10% SiC_p.

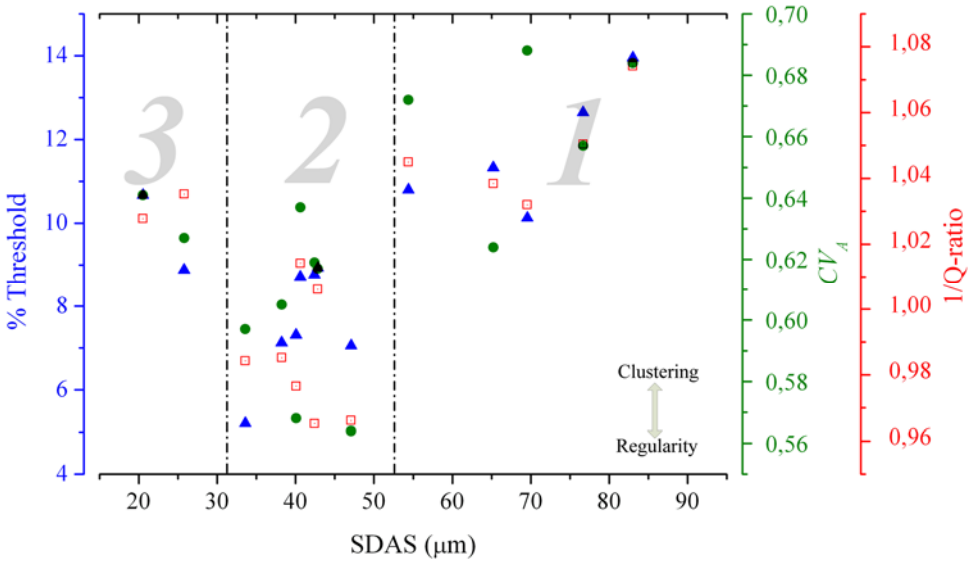

Figure 6.28 Effect of SDAS on clustering of reinforcement particles in A356 alloy composites reinforced with 20% SiC_p.

In the third interval, where the spacings were smaller than the average particle size, however, there was a net increase in amount of clustering. Karnezis *et al*[80] also observed a similar behavior in squeeze cast samples in which the arm spacings were lower than the average particle size. This reversed trend occurs when the fluid flow due to shrinkage cannot carry the particles through the finer secondary arms. The particles were therefore pushed by the finer mesh of secondary arms, resulting in formation of larger clusters[80].

The microstructural trends in these intervals are illustrated in Fig. 6.29 through sample micrographs. In the first interval (Fig. 6.29a), the particles accumulate at relatively large interdendritic regions. In the second interval (Fig. 6.29b), where the arm spacings are slightly larger than the average particle size, the number of particles that could be contained in these interdendritic spaces decreases significantly, leading to a considerable decrease in the amount of clustering. In the third interval (Fig. 6.29c), where the arm spacings are lower than the average SiC size, the particles cannot penetrate through the finer mesh of secondary arms and the amount of clustering again increases.

There is also a significant difference in amount of clustering between composites reinforced with 10% and 20% SiC_p. All statistical functions indicate a tendency towards regularity with an increase in SiC_p content from 10% to 20%. This tendency can be explained by two factors: (i) the statistical functions presented in this study are quite sensitive to local variations in distribution at low volume fractions, however, as the volume fraction of the particles increase the functions start to lose their effectiveness and the distinction between different clustering levels diminishes[25]; (ii) the presence of hard, insoluble particles increases the viscosity of the melt to a great extent[81]. Increased viscosity at higher volume fraction of particles suppresses the convection during solidification of the composite and hinders the settling of reinforcements[82, 83]. Therefore, the particles almost preserve their positions in the liquid state prior to solidification and show less tendency to agglomeration since faster settling rates at low fractions and convection effects contribute to clustering of reinforcement particles[2].

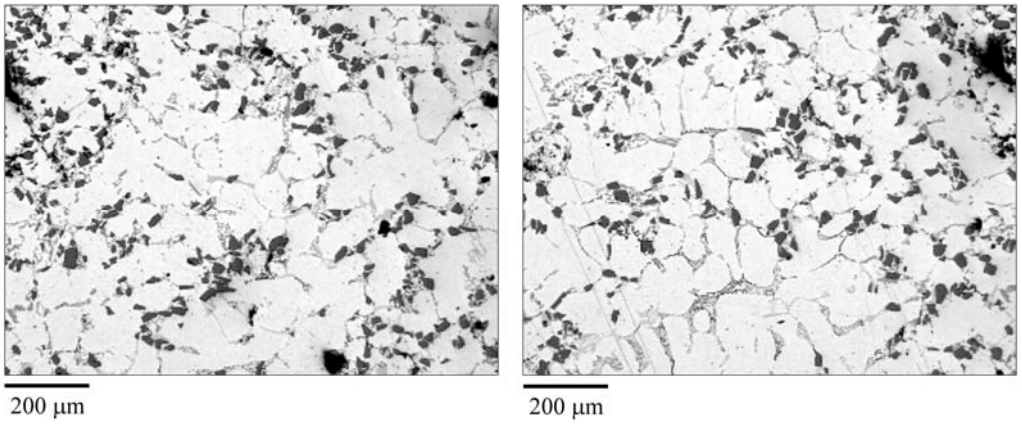

(a)

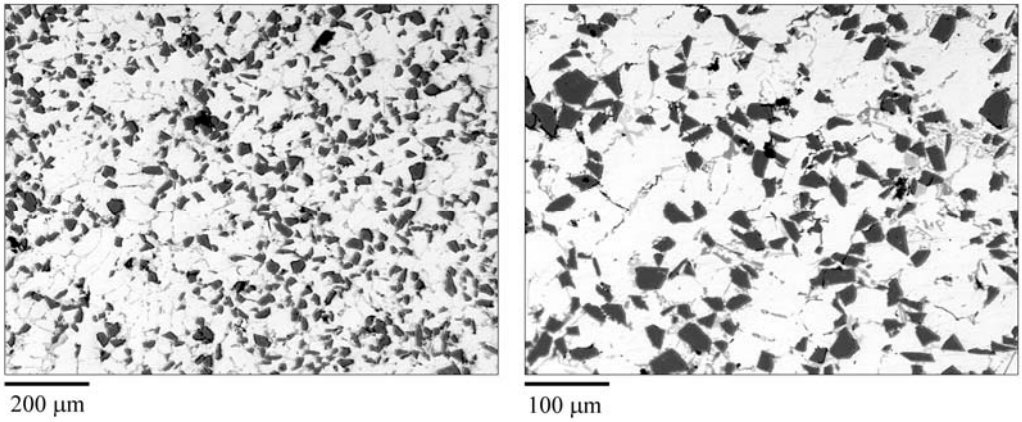

(b)

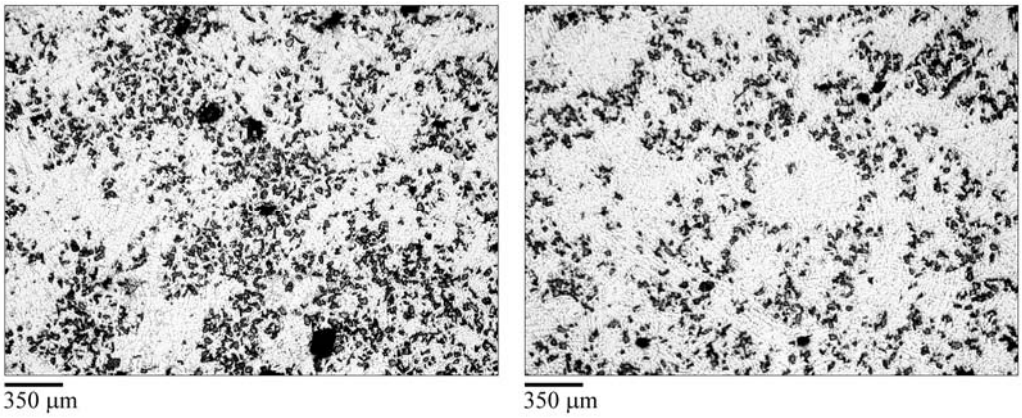

(c)

Figure 6.29 Micrographs from samples (a) A1002, (b) A2009 and (c) A1015, representing the microstructural trends in the first, second and third intervals, respectively.

6.4 Modelling of MMC Solidification

The results of the previous chapters indicate that, distribution of second phase particles is mainly determined by the secondary dendrite arm spacings. In general, finer arm spacings result in lower clustering levels. However, when the arm spacings are lower than the average particle size, this tendency is reversed, leading to an increase in the amount of clustering.

Therefore, in order to predict the cluster formation tendency in any cast part before production, one should be able to determine the dendritic arm spacing distribution throughout the casting. Such information would bring the advantage of assessing the critical regions in cast parts, where the particles are prone to agglomerate and help the engineers to come up with solutions by altering the solidification conditions or the design of the component. The final part of this study, therefore, focuses on numerical approaches to composite solidification to predict the local solidification rates and the resulting secondary dendrite arm spacings.

6.4.1 Prediction of Local Solidification Rate

A series of cooling curve simulations were performed to predict the local solidification rate distributions within the cylindrical castings. In each simulation, the experimental conditions were duplicated by entering the mold dimensions to the computer program. The simulated cooling curves were also plotted from the same radial locations with the experimental curves. The schematic illustrating the mold dimensions and the thermocouple locations is shown in Fig. 6.30.

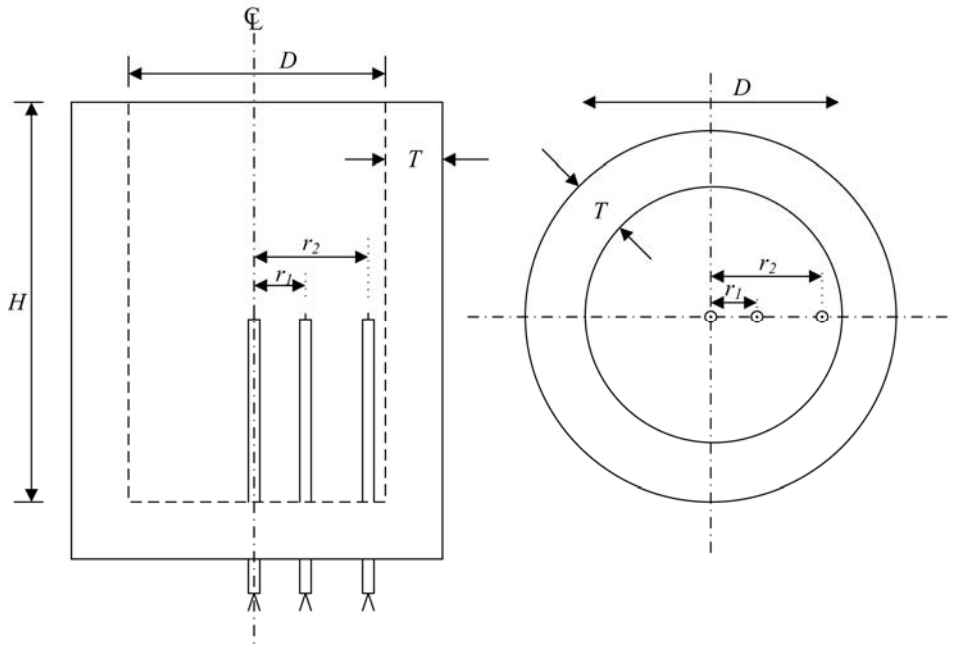

Figure 6.30 Schematic illustrating the mold dimensions and thermocouple locations.

Figs. 6.31 through 6.33 show the experimentally determined and simulated cooling curves for A356 alloy composites reinforced with SiC particles. Figs. 6.31a, 6.32a and 6.33a present the cooling curves obtained from the thermocouples located at the geometrical center (r = 0 mm) of the castings and Figs. 6.31b, 6.32b and 6.33b show the cooling curves obtained from various radial distances from the center, together with the simulated curves. The results reveal good agreement between the experimental and simulated cooling curves, especially in terms of local solidification time predictions.

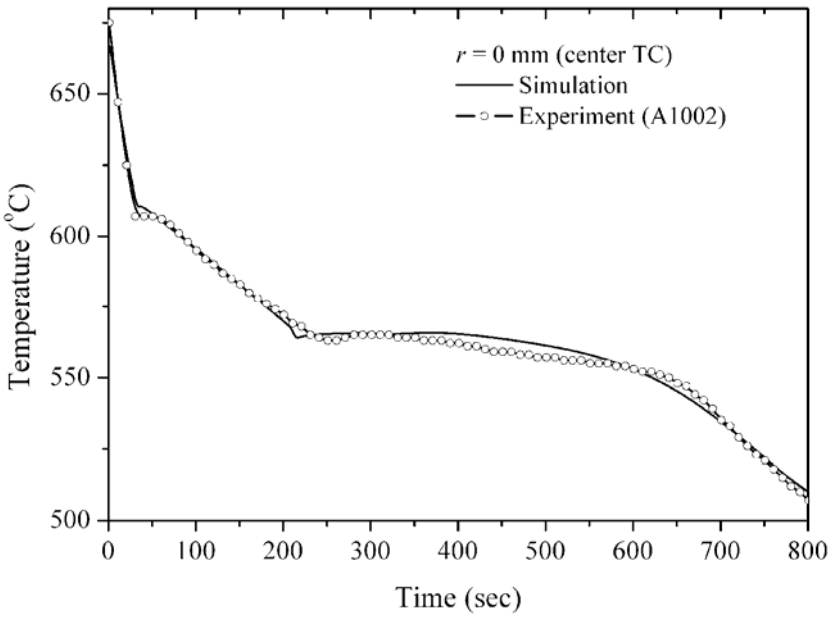

(a)

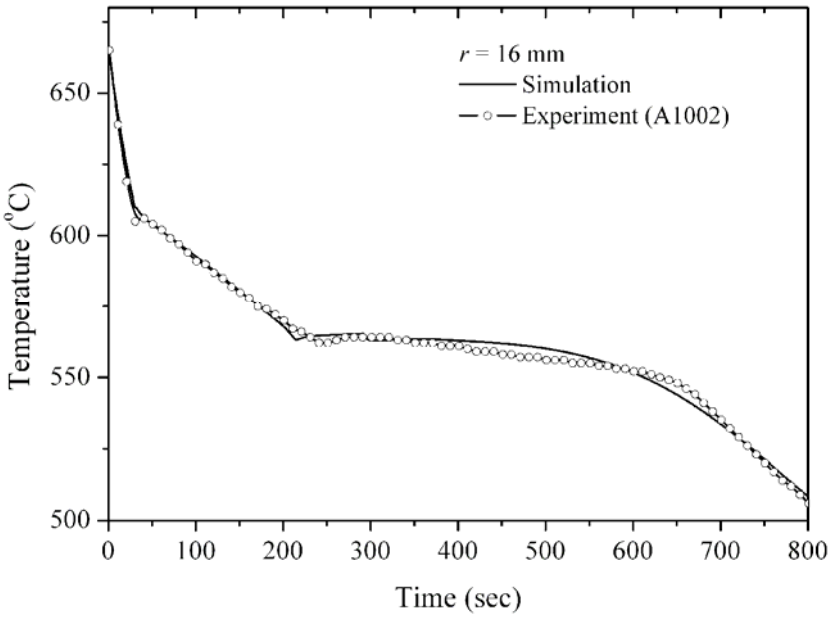

(b)

Figure 6.31 The simulated and experimental cooling curves of A356 alloy composite reinforced with 10% SiC_p (sample A1002). The mold dimensions are D = 50 mm, H = 60 mm, T = 12.5 mm, and the outer thermocouples are located at r_1 = 9 mm and r_2 = 16 mm.

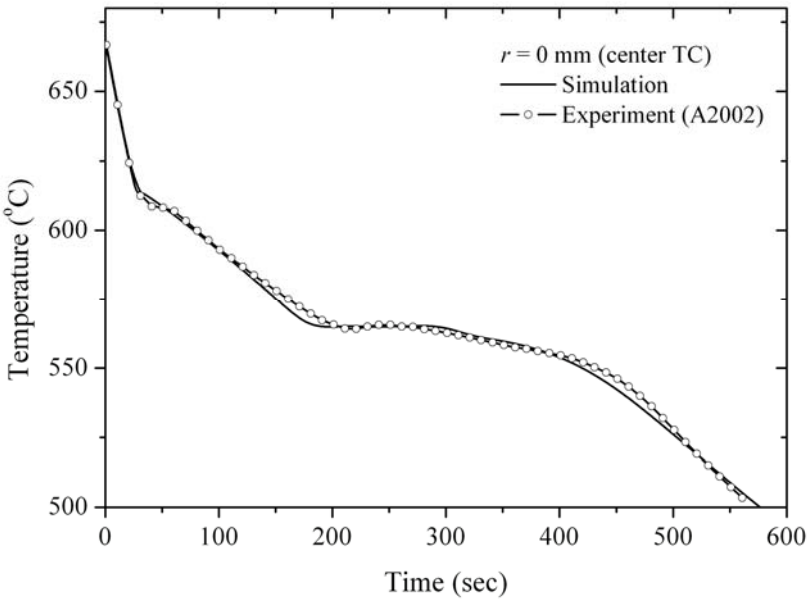

(a)

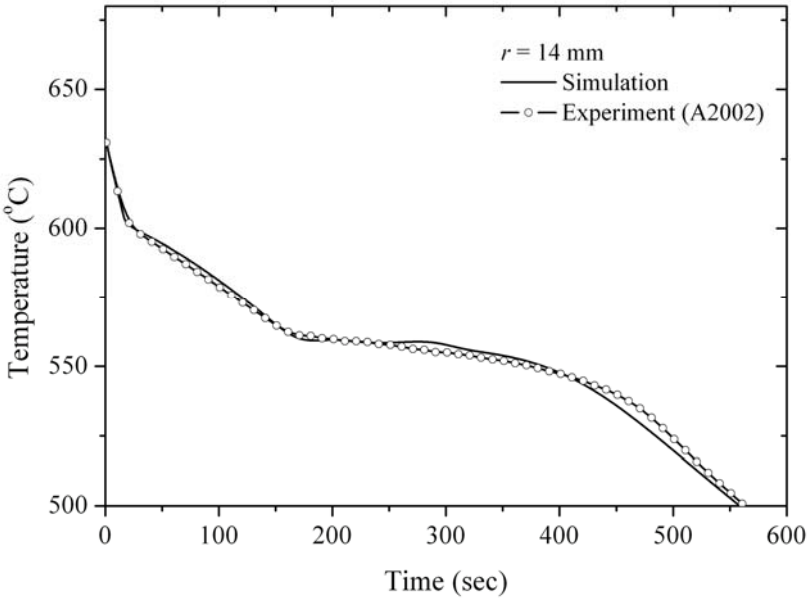

(b)

Figure 6.32 The simulated and experimental cooling curves of A356 alloy composite reinforced with 20% SiC_p (sample A2002). The mold dimensions are D = 55 mm, H = 60 mm, T = 12.5 mm, and the outer thermocouples are located at r_1 = 8 mm and r_2 = 14 mm.

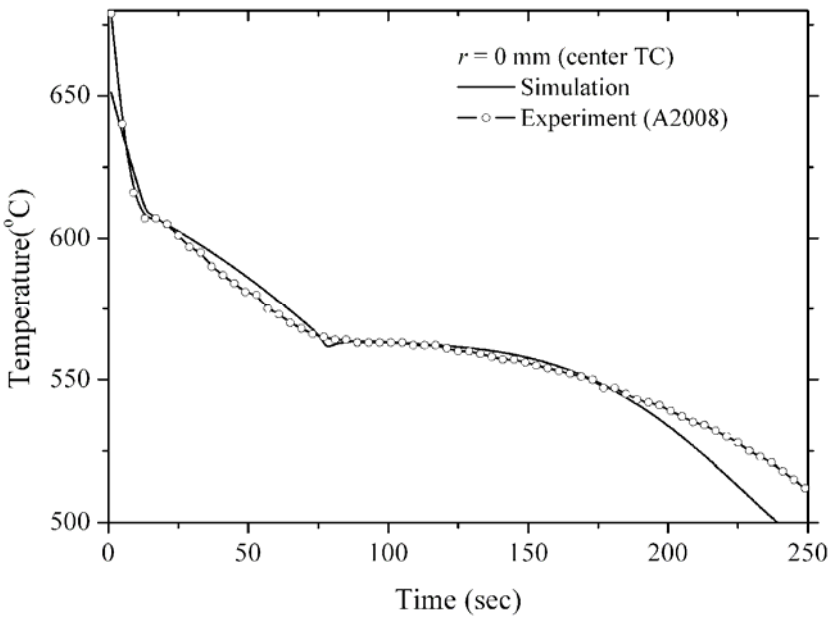

(a)

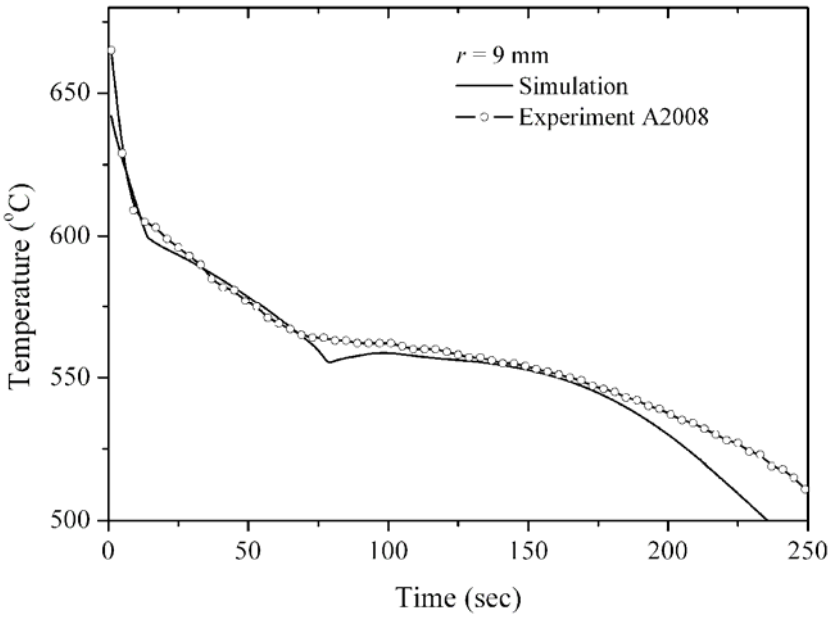

(b)

Figure 6.33 The simulated and experimental cooling curves of A356 alloy composite reinforced with 20% SiC_p (sample A2008). The mold dimensions are D = 30 mm, H = 50 mm, T = 15 mm, and the outer thermocouples are located at r_1 = 5 mm and r_2 = 9 mm.

There still exist some differences between the experimental and simulated curves, which may better be understood by close examination of the solidification kinetics in terms of evolution of the solid. Fig. 6.34 presents the variation of solidification rates during the course of solidification obtained from experimental cooling curves and simulation for sample A2002. The experimental solid fraction results were obtained by Fourier and Newtonian thermal analysis methods. The solidification rate of the simulated sample exhibits a higher initial peak (which corresponds to the nucleation and growth of primary α-Al dendrites) compared to the initial peaks of the experimental curves obtained by NTA and FTA. The simulated curve also ceases more rapidly as compared to the solidification rate curves of the actual sample. This is most probably due to the instantaneous nucleation model used in the calculations, which assumes that all nuclei are generated at the nucleation temperature. Therefore, the model predicts a high value of latent heat release at the initial stage of primary solidification. However, because the actual transformation proceeds with continuous nucleation during the interval of primary solidification, the initial maxima of the experimental curves are lower and the subsequent decrease in the solidification rates are slower.

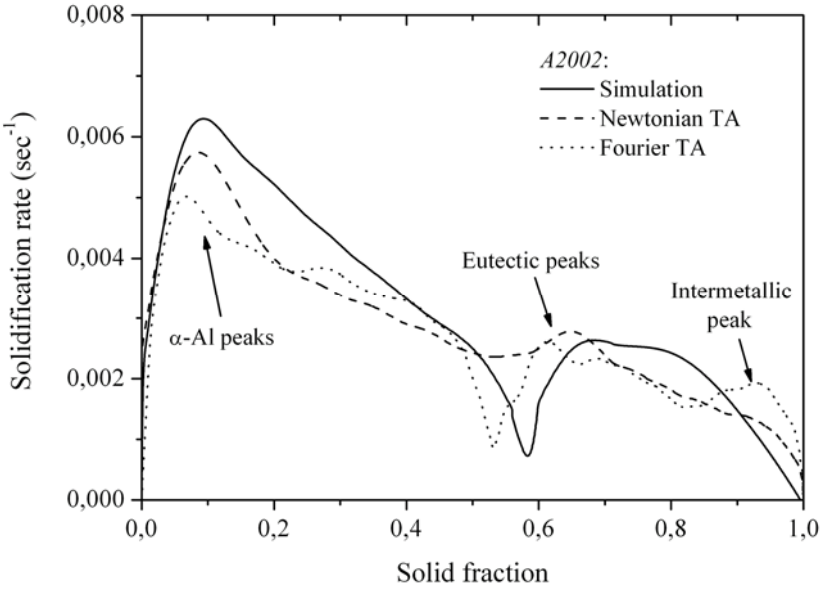

Figure 6.34 Variation of solidification rate as a function of solid fraction for sample A2002 obtained by NTA and FTA, together with simulation result.

The magnitudes of the second maxima are observed to be reasonably in agreement due to the continuous nucleation model used in eutectic solidification. However, the start of eutectic solidification in the simulated curve corresponds to a higher solid fraction as compared to the experimental observations as derived by FTA and NTA. The delay in eutectic nucleation cannot be detected when the transformation start times are considered on the cooling curves. This quantitative discrepancy indicates that further improvements are required to the model to simulate the nucleation kinetics of the eutectic grains.

There exists a third peak in the solidification rate curve of the FTA processed experimental cooling curve, which corresponds to formation of intermetallic phases such as Mg_2Si and β-Al_5FeSi, which was also illustrated in Fig. 6.2. This third peak is not visible on the simulated solidification rate curve. This is because of the pseudo-binary alloy assumption, which considers all alloying elements other than Si as solutes and calculates and equivalent solute for the eutectic reaction. Therefore, no extra transformation is visible after the eutectic reaction in the simulated curves.

6.4.2 Prediction of Secondary Dendrite Arm Spacings

As mentioned previously, we have assumed that the presence of SiC particles do not have any influence on the secondary dendrite arm spacings, which is in accordance with the previously reported results in the literature[1, 59] and with our experimental findings. Therefore, it was assumed that the dynamic coarsening model developed by Mortensen[65] can be applied both reinforcement contents (10% and 20%) without any modifications. Fig. 6.35 presents variation of SDAS as function of local solidification time for the composites, together with the predicted results from Eq. (4.30).

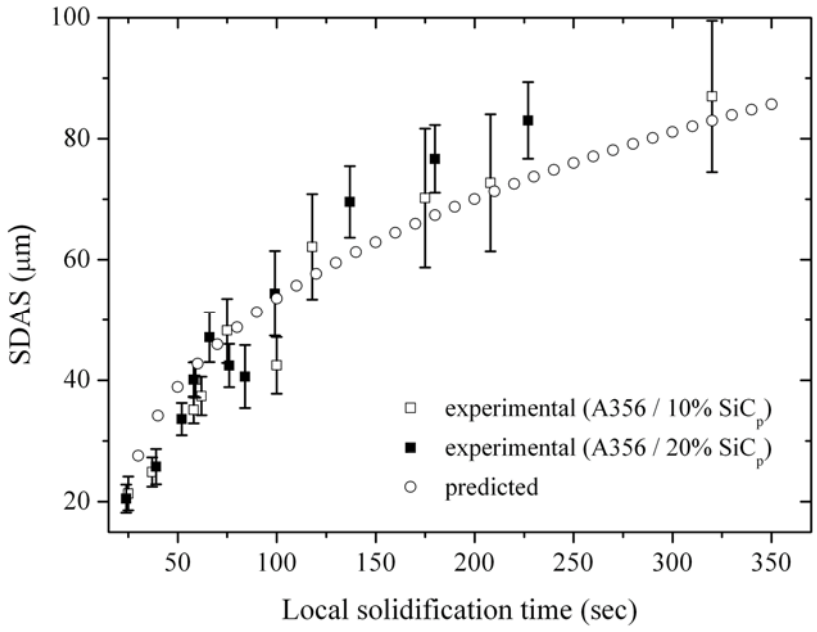

Figure 6.35 Predicted and experimental variations of secondary dendrite arm spacings as a function of local solidification time.

The experimental and predicted SDAS values are found to be in reasonably good agreement. Although the predicted and experimental variations have very similar trends, the predicted values are observed to be slightly higher than the actual spacings at local solidification times lower than approximately 50 seconds. This limitation may be a problem in correct prediction of SDAS values in rapidly cooled samples that belong to the third interval and therefore estimating the cluster formation tendencies. The origin of the quantitative discrepancies may be attributed to presence of factors not considered by the coarsening model.

Fig. 6.35 reveals that, the arm spacing distribution throughout any cast part can be predicted if the local solidification rate values at those locations are correctly calculated. Therefore, one can assess the local arm spacing at particular regions in a casting and evaluate the risk of cluster formation by looking at the particle size to SDAS ratio. One such example is shown in Fig. 6.36, which demonstrates the variation of SDAS values as a function of radial location within the casting for an A356 alloy composite reinforced with 20% SiC particles (sample A2009). It was observed that there exists a good agreement

between the experimental and predicted trends. However, the predicted values are slightly lower than the mean SDAS values all throughout the radial locations, which again may be attributed to the limitations discussed above and also to wrong estimation of local solidification times, which arises from incorrect description of the heat transfer system as a result of limitations in the thermophysical parameters.

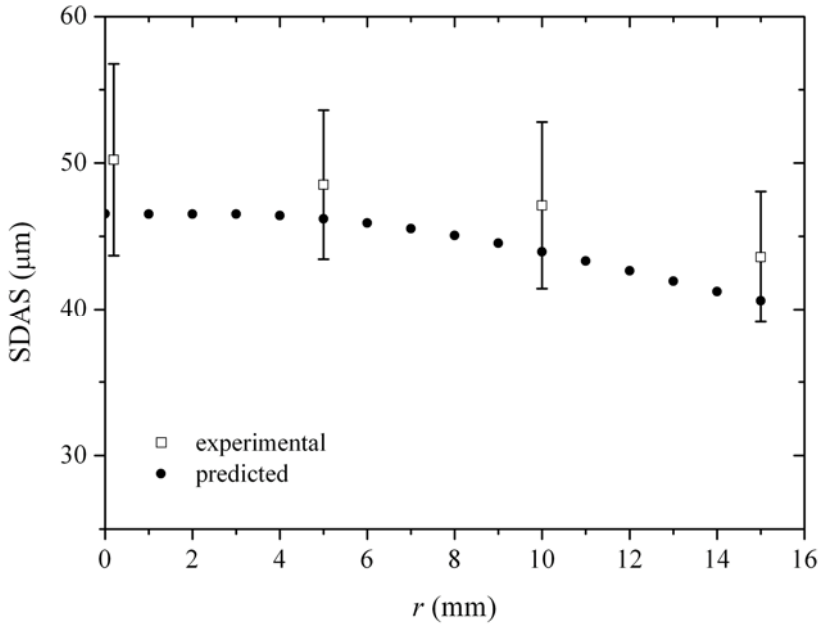

Figure 6.36 Predicted and experimental variations of secondary dendrite arm spacings as a function of radial location within the cylindrical casting for sample A2009.

CHAPTER 7

CONCLUSIONS

1. The distribution of SiC particles in aluminum alloy composites was found be highly dependent on secondary dendrite arm spacing (SDAS), which is a strong function of local solidification rate. In general, with decreasing arm spacings, particles exhibit less tendency towards clustering. At higher solidification rates, however, this tendency is reversed, resulting in formation of larger clusters. This reversed trend occurs when the average secondary dendrite arm spacing decreases below the average particle size. The particles cannot penetrate through the finer mesh of secondary arms and agglomerate in larger interdendritic channels. The results indicate that, in order to attain the lowest possible amount of particle clustering, the secondary dendrite arm spacings must lie with in the range of $d_{SiC} <$ SDAS $< 2d_{SiC}$, where d_{SiC} is the average particle diameter.

2. No relationships could be established between the as-cast particle distribution and the fraction of solid phase at the dendrite coherency (f_S^{DCP}). f_S^{DCP} indicates the fraction of solid phase when a solid network is established throughout the casting. This solid fraction value, however, does not give any information on the length scales that the particles were pushed by the growing dendrites during the course of solidification. Therefore, the fraction of solid phase at the dendrite coherency is not considered as a determining factor in clustering of reinforcement particles.

3. The applicability of various spatial characterization methods was investigated. Results indicate that, methods that describe the microstructural pattern over a statistics that presents a summary of the interaction between nearest particles have limited use in discontinuously reinforced composites since clustering in such materials is evidenced over many length scales. Methods such as the nearest neighbour statistics and Voronoi tessellation can describe the microstructural heterogeneity to a certain extent, however, cannot provide information on the characteristics of the pattern at length scales beyond nearest neighbour distances.

   K-function is observed to be an effective solution to overcome this problem, since it has the ability to analyze the microstructural pattern over many length scales. However, similar to the above aforementioned methods, *K*-function also cannot provide any sort of information regarding dimensions, locations and spatial connectivities of the detected clusters. However, as far as the fracture mechanics of the discontinuously reinforced composites is concerned, one also needs to gather such information in order to successfully relate the mechanical response of the composite to its microstructure.

   The local density statistics, on the other hand, was observed to provide a much better description of the composite microstructures. The method considers the microstructural pattern from the perspective of individual particles, therefore even in a pattern that globally conforms to random distribution, local clusters, that may actually control the mechanical properties, can be detected.

   The variation of above-threshold particles with observation scale show that clustering of SiC particles is most pronounced at length scales ranging between 150 - 500 μm. In general, slower solidification rates result in large clusters. The samples solidified with higher cooling rates, on the other hand, display small clusters, randomly distributed throughout the matrix. Further increasing the solidification rate, again produces large clusters due to agglomeration of particles within large interdendritic spaces.

The effect of metallographic field size on the corresponding statistics was also analyzed. It was observed that the length scales where clustering is most pronounced do not vary with metallographic field size. However, there are considerable differences in observed cluster dimensions. When the metallographic field area is increased, the kernel surfaces emerging from individual clusters merge together to reveal the actual cluster morphologies. Therefore, although clustering levels can successfully be quantified from relatively small micrographs, the actual dimensions of clusters can only be revealed from micrographs that represent much larger visual fields compared to reinforcement particle size.

4. Coupling of macroscopic heat transport with solidification kinetics through the latent heat method was observed to provide a neat description of MMC solidification process, especially in terms of local solidification time predictions. The experimental and predicted SDAS values are found to be in reasonably good agreement. Small quantitative discrepancies can be attributed to the presence of factors not considered in the model and incorrect description of the heat transfer system as a result of limitations in the thermophysical parameters.

   It was concluded that locations in a casting where there exists a tendency towards clustered particle arrangements can be successfully predicted prior to production with the described numerical approach. This advantage will obviously help engineers to come up with solutions to produce cast composites with more uniform microstructures and hence less prone to failure.

5. The present study differs from previous investigations in three ways. Firstly, the results hereby reported marks the first attempt in the literature to bring a quantitative approach to effect of dendritic solidification on spatial distribution of reinforcement particles.

   Another difference is that, this study approaches to the problem of clustering from a different perspective and quantifies the amount of clustering from the perspective of individual particles rather than global trends in the pattern. This is a much appropriate way to look at the problem under consideration since clusters in MMCs are in the form of local variations in particle content rather than compact,

well separated agglomerates and therefore are hard to detect by conventional methods of spatial statistics.

Finally, the described computational strategy marks the first attempt reported in the literature to predict the risk of cluster formation as a function of local solidification rate. With this approach, certain locations in a casting, where there exists a tendency towards clustered particle arrangements can be predicted before production. Such an ability will obviously help engineers to come up with solutions to produce these components with more uniform microstructures and hence, less prone to failure.

REFERENCES

1. D.J. Lloyd, *Composites Science and Technology* 35 (1989) 159-179

2. D.J. Lloyd, *International Materials Reviews* 39 (1994) 1-23

3. V.C. Nardone, K.M. Prewo, *Scripta Metallurgic*a 20 (1986) 43-48

4. V.C. Nardone, *Scripta Metallurgica* 21 (1987) 1313-1318

5. N. Ramakrishnan, *Acta Materialia* 44 (1996) 69-77

6. N. Chawla, C. Andres, J.W. Jones, J.E. Allison, *Metallurgical and Materials Transactions A* 29A (1998) 2843-2854

7. M. Vogelsang, R.J. Arsenault, R.M. Fisher, *Metallurgical Transactions A* 17A (1986) 379-389

8. R.J. Arsenault, L. Wang, C.R. Feng, *Acta Metallurgica et Materialia* 39 (1991) 47-57

9. N. Shi, B. Wilner and R.J. Arsenault, *Acta Metallurgica et Materialia* 40 (1992) 2841-2854

10. Li Chingshen, F. Ellyin, *International Journal of Solids and Structures* 37 (2000) 1389-1401

11. D.J. Lloyd, *Acta Metallurgica* 39 (1991) 59-71

12. Li Chingshen, F. Ellyin, *Metallurgical and Materials Transactions* A 26A (1995) 3177-3182

13. J. Hall, J.W. Jones, A. Sachdev, Materials Science and Engineering A 183 (1994) 69-80

14. A. Ayyar, N. Chawla, *Composites Science and Technology* 66 (2006) 1980-1994

15. N. Chawla, B.V. Patel, M. Koopman, K.K.Chawla, R. Saha, B.R. Patterson, E.R. Fuller, S.A. Langer, *Materials Characterization* 49 (2003) 395-407

16. J.E. Spowart, *Materials Science and Engineering A* 425 (2006) 225-237

17. J. Segurado, J.L. LLorca, *Mechanics of Materials* 38 (2006) 873-883

18. L. Mishnaevsky Jr, K. Derrien, D. Baptiste, *Composites Science and Technology* 64 (2004) 1805-1818

19. J.J. Lewandowski, C. Liu, *Materials Science and Engineering A* 107 (1989) 241-255

20. X.Q. Xu, D.F. Watt, *Acta Materialia* 44 (1996) 4501-4511

21. N. Ayyar, N. Chawla, *Acta Materialia* 55 (2007) 6064-6073

22. P.J. Wray, O. Richmond, H.L. Morrison, *Metallograph*y 16 (1983) 39-58

23. W.A. Spitzig, J.F. Kelly, O. Richmond, *Metallography* 18 (1985) 235-261

24. R.K. Everett, J.H. Chu, *Journal of Composite Materials* 27 (1992) 1128-1144

25. S. Ghosh, Z. Nowak, K. Lee, *Acta Materialia* 45 (1997) 2215-2234

26. M. Li, S. Ghosh, O. Richmond, H. Weiland, T.N. Rouns, *Materials Science and Engineering A* 265 (1999) 153-173

27. P. Ganguly, W.J. Poole, *Materials Science and Engineering A* 332 (2002) 301-310

28. J.D. Scalon, N.R.J. Fieller, E.C. Stillman, H.V. Atkinson, *Materials Science and Engineering A* 356 (2003) 245-257

29. G. Upton, B. Fingleton, *Spatial Data Analysis by Example* Vol. I, Wiley, New York, (1985)

30. M. Li, S. Ghosh, O. Richmond, H. Weiland, T.N. Rouns, *Materials Science and Engineering A* 265 (1999) 153-173

31. B.D. Ripley, *Journal of Applied Probability* 13 (1976) 255-266

32. D. Prodanov, N. Nagelkerke, E. Marani, *Journal of Neuroscience Methods* 160 (2007) 93-108

33. P.J. Diggle, *Applied Statistics* 34 (1985) 138-147

34. A.C. Gatrell, T.C. Bailey, P.J. Diggle, B.S. Rowlingson, *Transactions of the Institute of British Geographers* 21 (1996) 256-274

35. G. Voronoi, *Journal für die Reine und Angewandte Mathemetik* 133 (1907) 97-178

36. I.G. Chen, D.M. Stefanescu, *AFS Transactions* 92 (1984) 947-964

37. E. Fras, K. Kapturckiewicz, A Burbielko, H.F. Lopez, *AFS Transactions* 101 (1993) 505-511

38. M. Kılıç, A. Yiğit, *Isı Transferi* (*in Turkish*) Alfa, İstanbul (2004) 131-132

39. M.J. Oliveira, L.F. Malheiros, C.A.S. Ribeiro, *Journal of Materials Processing Technology* 92-93 (1999) 25-30

40. J.O. Barlow, D.M. Stefanescu, *AFS Transactions* 105 (1997) 349-354

41. L. Backerud, B. Chalmers, *Transactions of the Metallurgical Society of AIME* 245 (1969) 309-318

42. L. Arnberg, G. Chai, L. Backerud, *Materials Science and Engineering A* 173 (1993) 101-103

43. G. Chai, L. Backerud, T. Rolland, L. Arnberg, *Metallurgical and Materials Transactions A* 26A (1995) 965-970

44. N.L.M. Veldman, A.K. Dahle, D.H. StJohn, L. Arnberg, *Metallurgical and Materials Transactions A* 32A (2001) 147-155

45. S.L. Backerud, G.K. Sigworth, *AFS Transactions* 97 (1989) 459-463

46. H. Jiang, W.T. Kierkus, J.H. Sokolowski, *AFS Transactions* 68 (1999) 169-172

47. M.C. Flemings, *Solidification Processing* McGraw-Hill, New York (1974)

48. D.M. Stefanescu, *Science and engineering of casting solidification* Kluwer Academic/Plenum Publishers, New York (2002)

49. M. Rappaz, *International Materials Reviews* 34 (1989) 93-123

50. P. Thevoz, J.L. Desbiolles, M. Rappaz, *Metallurgical Transactions A* 20A (1989) 311-322

51. D.M. Stefanescu, G. Upadhya, D. Bandyopadhyay, *Metallurgical Transactions A* 21A (1990) 997-1005

52. L Nastac, *Modelling and simulation of microstructure evolution in solidifying alloys* 1st ed, Springer, US (2004)

53. M.B. Djurdevic, R. Francis, J.H. Sokolwski, D. Emadi, M. Sahoo, *Materials Science and Engineering A* 386 (2004) 277-283

54. C. Gonzalez-Rivera, B. Campillo, M. Castro, M. Herrera, J. Juarez-Islas, *Materials Science and Engineering A* 279 (2000) 149-159

55. H. Emmerich, *The Diffuse Interface Approach in Materials Science* Springer, Berlin (2003)

56. L. Nastac, D.M. Stefanescu, *Metallurgical and Materials Transactions A* 27A (1996) 4061-4074

57. A.K. Dahle, K. Nogita, J.W. Zindel, S.D. McDonald, L.M. Hogan, *Metallurgical and Materials Transactions A* 32A (2001) 949-960

58. P.K. Rohatgi, S. Ray, R. Asthana, C.S. Narendranath, *Materials Science and Engineering* 162 (1993) 163-174

59. S. Nagarajan, B. Dutta, M.K. Surappa, *Composites Science and Technology* 59 (1999) 897-902

60. W. Oldfield, *ASM Transactions* 59 (1966) 945-961

61. W.A. Johnson, R.F. Mehl, *Transactions of AIME* 135 (1939) 416-458

62. M. Avrami, *Journal of Chemical Physics* 8 (1940) 212-24

63. W. Kurz, D.J. Fisher, *Fundamentals of Solidification* Trans Tech Publications, Switzerland (1989)

64. T.Z. Kattamis, M.C. Flemings, *Transactions of AIME* 233 (1965) 992-999

65. A. Mortensen, *Metallurgical Transactions* 22A (1991) 569-574

66. D.A. Porter, K.E. Easterling, *Phase Transformations in Metals and Alloys* Second ed, Chapman & Hall, London (1992)

67. B.C. Pai, G. Ramani, R.M. Pillai, K.G. Satyanarayana, *Journal of Materials Science* 30 (1995) 1903-1911

68. S. Nagata, *Mixing Principles and Applications* Wiley, New York (1975)

69. A.K. Dahle, L. Arnberg, *Acta Materialia* 45 (1997) 547-559

70. S. Nafisi, R. Ghomashchi, *Journal of Materials Processing Technology* 174 (2006) 371-383

71. A.K. Dahle, D.H. StJohn, *Acta Materialia* 47 (1999) 31-41

72. A.K. Dahle, L. Arnberg, *Materials Science and Engineering A* 225 (1997) 38-46

73. C.M. Dinnis, J.A. Taylor, A.K. Dahle, *Scripta Materialia* 53 (2005) 955-958

74. Y.L. Liu, S.B. Kang, H.W. Kim, *Materials Letters* 41 (1999) 267-272

75. R. Pyrz, *Composites Science and Technology* 50 (1994) 197-208

76. R. Pyrz, *Materials Science and Engineering A* 177 (1994) 253-259

77. O. Nilsson, H. Mehling, R. Horn, J. Fricke, R. Hofmann, S.G. Muller, R. Eckstein, D. Hofmann, *High Temperatures-High Pressures* 29 (1997) 73-79

78. S.I. Bakhtiyarov, R.A. Overfelt, S.G. Teodorescu, *Journal of Materials Science* 36 (2001) 4643-4648

79. J. Campbell, *Castings* Butterworth-Heinemann, Oxford (1991)

80. P.A. Karnezis, G. Durrant, B. Cantor, *Materials Characterization* 40 (1998) 97-109

81. B. Dutta, M.K. Surappa, *Composites* 29A (1998) 565-573

82. J. Hashim, L. Looney, M.S.J. Hashmi, *Journal of Materials Processing Technology* 123 (2002) 251-257

83. P.N. Bindumadhavan, T.K. Chia, M. Chandrasekaran, H.K. Wah, L.N. Lam, O. Prabhakar, *Materials Science and Engineering A* 315 (2001) 217-226

APPENDIX A

PHASE DIAGRAM AND SOLIDIFICATION PATH OF A356 ALLOY

A356 is basically an Al - 7% Si - 0.35% Mg alloy. In order to present an accurate picture of the solidification path of the alloy and also the phases present at room temperature, various isothermal sections obtained from the ternary Al-Si-Mg phase diagram and solidification sequence of various phases were calculated by Pandat Multi-Component Phase Diagram Calculation Software (CompuTherm LLC, v5).

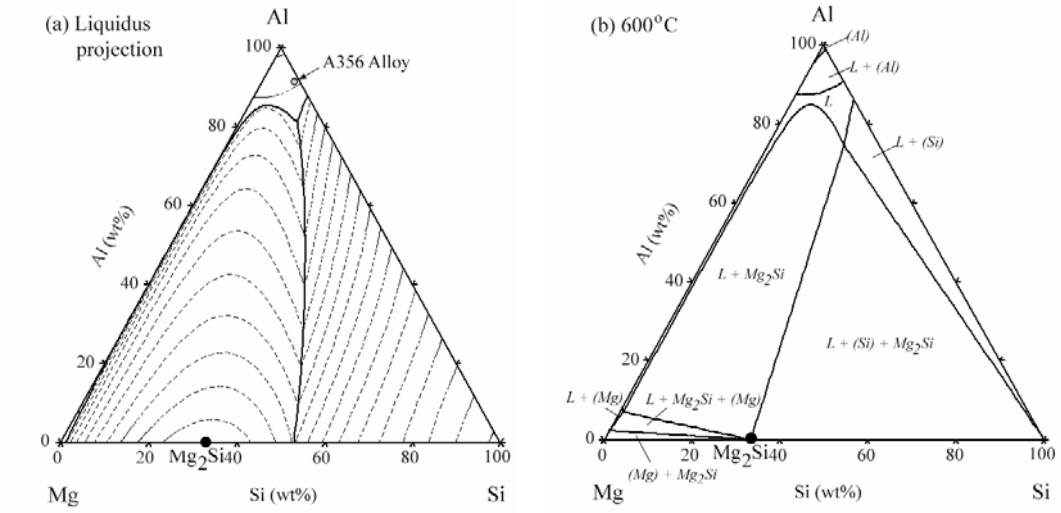

Figure A1 Isothermal sections from the Al-Si-Mg ternary phase diagram.

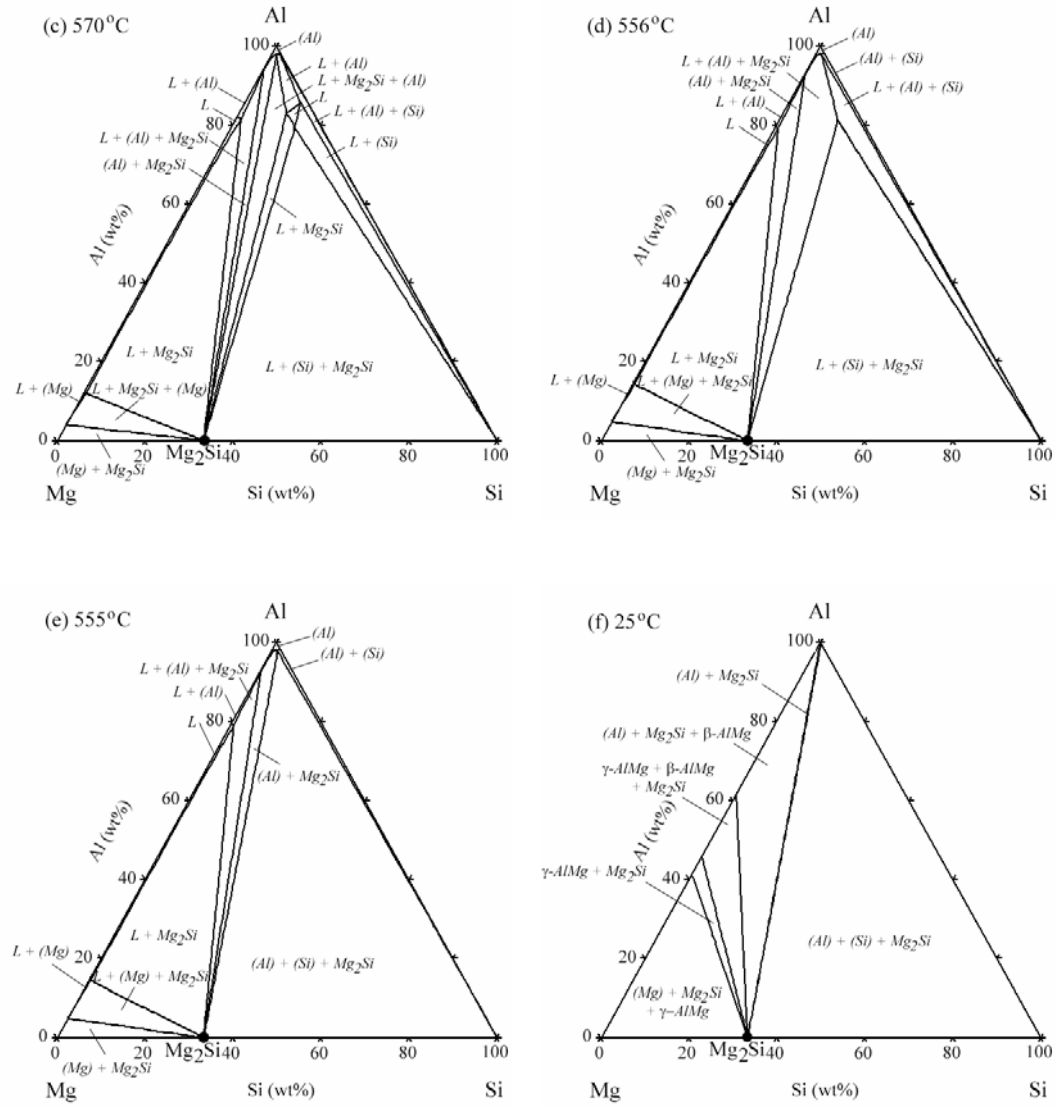

Figure A1 Isothermal sections from the Al-Si-Mg ternary phase diagram (*continued*).

Table A1 Theoretical non-equilibrium (Scheil) solidification sequence of A356 alloy calculated by Pandat Multi-Component Phase Diagram Calculation Software.

T (°C)	X (AL)	X (MG)	X (SI)	ΔG (J)	PhaseName
613,57	0,9265	0,0035	0,07	-31000,3	LIQ + (Al)
613,47	0,926352	0,003506	0,070142	-31001,8	LIQ + (Al)
613,27	0,926057	0,003518	0,070425	-31003	LIQ + (Al)
612,87	0,925467	0,003542	0,070991	-31005,4	LIQ + (Al)
612,07	0,924288	0,003591	0,072122	-31009,7	LIQ + (Al)
610,47	0,921936	0,003687	0,074377	-31017,5	LIQ + (Al)
607,27	0,91726	0,003879	0,078861	-31029,1	LIQ + (Al)
604,07	0,912617	0,004069	0,083313	-31009,8	LIQ + (Al)
600,87	0,908008	0,004259	0,087733	-30988,8	LIQ + (Al)
597,67	0,903432	0,004447	0,092121	-30966,1	LIQ + (Al)
594,47	0,898887	0,004635	0,096477	-30941,9	LIQ + (Al)
591,27	0,894374	0,004822	0,100803	-30916,2	LIQ + (Al)
588,07	0,889892	0,005009	0,1051	-30889	LIQ + (Al)
584,87	0,885439	0,005195	0,109366	-30860,5	LIQ + (Al)
581,67	0,881016	0,00538	0,113604	-30830,7	LIQ + (Al)
578,47	0,876621	0,005565	0,117813	-30799,6	LIQ + (Al)
575,27	0,872255	0,00575	0,121995	-30767,3	LIQ + (Al)
574,87	0,871711	0,005773	0,122515	-30726,9	LIQ + (Al)
574,67	0,87144	0,005785	0,122776	-30722,2	LIQ + (Al)
574,66	0,871432	0,005785	0,122783	-30719,7	LIQ + (Al) + (Si)
574,56	0,871128	0,00605	0,122823	-30734,9	LIQ + (Al) + (Si)
574,36	0,87052	0,006579	0,122901	-30759,1	LIQ + (Al) + (Si)
573,96	0,869303	0,007637	0,123059	-30801,3	LIQ + (Al) + (Si)
573,16	0,866866	0,009756	0,123378	-30870,7	LIQ + (Al) + (Si)
571,56	0,861971	0,013998	0,124032	-30979,5	LIQ + (Al) + (Si)
568,36	0,852102	0,022502	0,125396	-31151,4	LIQ + (Al) + (Si)
565,16	0,842124	0,031034	0,126842	-31411,6	LIQ + (Al) + (Si)
561,96	0,83203	0,0396	0,128371	-31668,3	LIQ + (Al) + (Si)
558,76	0,821813	0,048201	0,129986	-31917,7	LIQ + (Al) + (Si)
557,16	0,816655	0,052517	0,130828	-32158,6	LIQ + (Al) + (Si)
556,36	0,814064	0,054679	0,131257	-32278,6	LIQ + (Al) + (Si)
555,96	0,812766	0,05576	0,131474	-32338,4	LIQ + (Al) + (Si)
555,91	0,81258	0,055915	0,131505	-32368,2	LIQ + (Al) + (Si) + Mg_2Si
555,91	0,81258	0,055915	0,131505	-32372,5	(Al) + (Si) + Mg_2Si

Table A2 Theoretical non-equilibrium (Scheil) solid phase evolution of A356 alloy calculated by Pandat Multi-Component Phase Diagram Calculation Software.

T (°C)	f_L	f_S	f_{Tot}(Al)	f_{Tot}(Si)	f_{Tot}(Mg_2Si)
613,57	1	0	0	0	0
613,47	0,997718	0,002282	0,002282	0	0
613,27	0,993185	0,006815	0,006815	0	0
612,87	0,984236	0,015764	0,015764	0	0
612,07	0,9668	0,0332	0,0332	0	0
610,47	0,933668	0,066332	0,066332	0	0
607,27	0,873612	0,126388	0,126388	0	0
604,07	0,820779	0,179221	0,179221	0	0
600,87	0,773955	0,226045	0,226045	0	0
597,67	0,732181	0,267819	0,267819	0	0
594,47	0,69469	0,30531	0,30531	0	0
591,27	0,660864	0,339136	0,339136	0	0
588,07	0,630195	0,369805	0,369805	0	0
584,87	0,602266	0,397734	0,397734	0	0
581,67	0,576729	0,423271	0,423271	0	0
578,47	0,553292	0,446708	0,446708	0	0
575,27	0,531709	0,468291	0,468291	0	0
574,87	0,529136	0,470864	0,470864	0	0
574,67	0,52786	0,47214	0,47214	0	0
574,66	0,527822	0,472178	0,472178	0	0
574,56	0,500454	0,499546	0,496568	0,002977	0
574,36	0,452731	0,547269	0,539098	0,008171	0
573,96	0,378352	0,621648	0,605378	0,016269	0
573,16	0,281021	0,718979	0,6921	0,026879	0
571,56	0,180225	0,819775	0,781885	0,037891	0
568,36	0,099748	0,900252	0,853532	0,04672	0
565,16	0,067398	0,932602	0,882321	0,050281	0
561,96	0,050232	0,949768	0,897593	0,052175	0
558,76	0,039695	0,960305	0,906965	0,053341	0
557,16	0,035863	0,964137	0,910372	0,053765	0
556,36	0,034199	0,965801	0,911853	0,053949	0
555,96	0,03342	0,96658	0,912545	0,054035	0
555,91	0,033311	0,966689	0,912642	0,054047	0
555,91	0	1	0,940323	0,05727	0,002408

APPENDIX B

MOLD DIMENSIONS AND THERMOCOUPLE LOCATIONS

Table B1 Mold dimensions and thermocouple locations (r_2, r_3)

Sample	H (mm)	D (mm)	T (mm)	r_2 (mm)	r_3 (mm)
A1001	60	55	10	7	20
A1002	60	50	12.5	9	16
A1003	60	45	15	4	14
A1004	60	40	17.5	6	14
A1005	55	50	17.5	4	10
A1006	55	37	11.5	7	11
A1007	55	34	13	4	10
A1008	50	32	14	4	7
A1009	50	30	15	9	14
A1010	45	30	15	6	10
A1011	45	28	16	5	10
A1012	45	25	17.5	4	8
A1013	40	25	12.5	4	9
A1014	40	20	15	4	8
A1015	35	18	11	4	7
A2001	60	55	10	8	12
A2002	60	55	12.5	8	14
A2003	60	45	15	6	16
A2004	60	40	17.5	8	15
A2005	55	35	20	5	8
A2006	55	32	14	6	9
A2007	55	30	15	4	8
A2008	50	30	15	5	9
A2009	50	28	16	5	9
A2010	45	28	16	5	10
A2011	45	25	17.5	4	10
A2012	40	25	17.5	5	9
A2013	40	20	15	4	8
A2014	35	18	11	3	7

There is also a third thermocouple (r_1) placed at the center of each cylindrical mold (r = 0 mm).

Figure B1 A sample cylindrical thermal analysis cup with three thermocouples placed at three different radial locations.

VITA

PERSONAL INORMATION

Last Name, Name	: Çetin, Arda
Nationality	: Turkish (TC)
Date and Place of Birth	: January 05, 1977, Ankara
Marital Status	: Single
Voice	: +90-532-408-0902
E-mail	: ardacetin@gmail.com

EDUCATION

Degree	**Institution**	**Year of Graduation**
MS	METU, Metallurgical and Materials Eng.	2002
BS	METU, Metallurgical and Materials Eng.	1999
High School	Gazi Anatolian High School	1994

WORK EXPERIENCE

Year	**Place**	**Enrollment**
2007-present	TAREL Technological Research	Research Engineer
2002-2007	METU, Metallurgical and Materials Eng.	Research Assistant
1998 August	Arçelik	Intern Engineering Student
1997 July	Ergenekon Steel Casting	Intern Engineering Student

PUBLICATIONS

1. A. Çetin, A. Kalkanlı, Effect of solidification rate on spatial distribution of SiC particles in A356 alloy composites, Journal of Materials Processing Technology, In Press (doi:10.1016/j.jmatprotec.2007.11.065)

2. A. Çetin, A. Kalkanlı, Investigation of microporosity formation mechanisms in A356 aluminum alloy, Proceedings of The 13th International Metallurgy and Materials Congress and Fair, Istanbul, 9-11 November 2006, 1766-1773

3. O. Elmabrouk, A. Çetin, A. Kalkanlı, E. Selçuk, Application of cooling curves as a process control tool in production of compacted graphite cast iron, Proceedings of The 13th International Metallurgy and Materials Congress and Fair, Istanbul, 9-11 November 2006, 1721-1728

4. A. Çetin, A. Kalkanlı, Evaluation of latent heat of solidification of gray cast iron from cooling curves, Canadian Metallurgical Quarterly 44 (2005) 1-6

5. A. Çetin, A. Kalkanlı, Particle distribution in SiC reinforced aluminum matrix composites, Proceedings of The 12th International Metallurgy and Materials Congress and Fair, Istanbul, 28 September – 2 October 2005, 799-807

6. A. Çetin, A. Kalkanlı, Computer aided thermal analysis of gray cast iron by using cooling curves, Proceedings of The 66th World Foundry Congress, Istanbul, 6-9 September 2004, 837-848